

***Institute of***

***Geophysics and***

***Planetary***

***Physics***

# ***1994 Annual Report***

***Frederick J. Ryerson, editor***  
*Manuscript date: September 29, 1995*

*UCRL-53809-94*  

---

*Lawrence Livermore  
National Laboratory  
University of California*

---

#### Disclaimer

This document was prepared as an account of work sponsored by an agency of the United States Government. Neither the United States Government nor the University of California nor any of their employees makes any warranty, express or implied, or assumes any legal liability or responsibility for the accuracy, completeness, or usefulness of any information, apparatus, product, or process disclosed, or represents that its use would not infringe privately owned rights. Reference herein to any specific commercial products, process, or service by trade name, trademark, manufacturer, or otherwise, does not necessarily constitute or imply its endorsement, recommendation, or favoring by the United States Government or the University of California. The views and opinions of authors expressed herein do not necessarily state or reflect those of the United States Government or the University of California and shall not be used for advertising or product endorsement purposes.

UCRL-53809-94

Work performed under the auspices of the U.S. Department of Energy by Lawrence Livermore National Laboratory under Contract W-7405-Eng-48.

This report has been reproduced directly from the best available copy. Available to DOE and DOE contractors from the Office of Scientific and Technical Information, P.O. Box 62, Oak Ridge, TN 37831; prices available from (615) 576-8401 FTS 626-8401. Available to the public from the National Technical Information Service, U.S. Department of Commerce, 5285 Port Royal Rd., Springfield, VA 22161.

*Institute of  
Geophysics and  
Planetary  
Physics*

*Lawrence Livermore  
National Laboratory*

# ***1994 Annual Report***

*October 1, 1993 through  
September 30, 1994*

*Edited by  
Frederick J. Ryerson  
Institute of Geophysics and Planetary Physics  
University of California*

---

## **Acknowledgments**

Arlene L. Manning prepared the manuscript for this report. Carolin Middleton was the publication editor, John Danielson and Al Garruto were the graphic designers, and Irene Chan was the technical illustrator. Charles Alcock, George Zandt, and William Nellis assisted in the technical reviews.

---

## Section I. Overview \_\_\_\_\_ 1

---

## Section II. Highlights of Fiscal Year 1994 \_\_\_\_\_ 5

Center for Geosciences \_\_\_\_\_ 5

Center for High-Pressure Sciences \_\_\_\_\_ 24

Astrophysics Research Center \_\_\_\_\_ 29

---

## Section III. Research Summaries of Collaborative Projects \_\_\_\_\_ 35

### *Geosciences* \_\_\_\_\_ 35

A Global Survey for the 80-km Discontinuity Using Three-Component Broadband Data  
*Peter Shearer, George Zandt, William R. Walter, and Paul Earle* \_\_\_\_\_ 35

Shear-Wave Velocity Structure beneath Central California from Surface-Wave Dispersion  
*Jiajun Zhang and William R. Walter* \_\_\_\_\_ 37

Investigation of the April 25, 1992, Cape Mendocino Aftershock Sequence  
*Susan Y. Schwartz, George Zandt, and Stanley Ruppert* \_\_\_\_\_ 40

Continuous Global Positioning System Monitoring in Northern California  
*Barbara A. Romanowicz, Shawn Larsen, and Richard Clymer* \_\_\_\_\_ 42

Modeling Small-Scale Asthenosphere Convection under California  
*Jason Phipps Morgan, George Zandt, Charles Carrigan, and Mara Yale* \_\_\_\_\_ 45

Upper-Mantle P-Velocity Structure beneath Central and Northern California  
*Charles J. Ammon, George Zandt, and Stanley Ruppert* \_\_\_\_\_ 47

Monazite as a Prograde Geochronometer: Determination of Pb Diffusion Rates in Monazite  
*Daniel L. Farber, Kevin D. McKeegan, T. Mark Harrison, and Frederick J. Ryerson* \_\_\_\_\_ 49

Actinide Element Partitioning at High Pressures between Coexisting  
Silicate Melts and Crystals: Constraints on Magmatic Segregation Processes  
*Quentin Williams, Frederick J. Ryerson, Henry Shaw,  
Charles C. Lundstrom, and Daniel L. Farber* \_\_\_\_\_ 52

Point-Defect Diffusion in Olivine Rock  
*Steven Constable and Alfred G. Duba* \_\_\_\_\_ 54

Measurements of Muon-Induced  $^{10}\text{Be}$  and  $^{26}\text{Al}$  in Terrestrial Quartz  
*Kunihiro Nishiizumi, Robert C. Finkel, and Marc W. Caffee* \_\_\_\_\_ 56

Studies of Soil Dynamics and Loess Paleoclimate Records Using Cosmogenic Nuclide  $^{10}\text{Be}$   
*Devendra Lal, Marc W. Caffee, Robert C. Finkel, John R. Southon, and Zhaoyan Gu* \_\_\_\_\_ 58

Crustal Thickening in Southern Tibet over the Last 27 Ma?: The Gangdese Thrust Revisited  
*T. Mark Harrison, An Yin, and Frederick J. Ryerson* \_\_\_\_\_ 62

Late Cenozoic Uplift History of the Tian Shan Region, Central Asia <i>An Yin, T. Mark Harrison, Frederick J. Ryerson, Marc W. Caffee, Robert C. Finkel, and Peter Craig</i>	64
--	----

An Asteroid-Meteorite Link: High-Resolution Exposure Age Chronology <i>Kurt Marti, Marc W. Caffee, Robert C. Finkel, Thomas Graf, Kunihiko Nishiizumi, and Yoosook Kim</i>	67
---	----

## *High-Pressure Sciences* 69

Pressure-Induced Morphology and Spatial Correlations of $\text{Ni}_3\text{X}$ Precipitates in Binary Ni-Based Alloys <i>Alan J. Ardell, Frederick J. Ryerson, and Abhay Maheshwari</i>	69
--	----

Dynamic Compaction of Alumina–Zirconia Ceramics <i>Joanna McKittrick, William J. Nellis, and John Freim</i>	72
--	----

Shock Compaction of Ferromagnetic Particles <i>M. Brian Maple, William J. Nellis, and Ricky Chau</i>	74
---	----

Semiconductors under High Pressure <i>Robert N. Shelton, Harry B. Radousky, and Stephen H. Irons</i>	76
---	----

Experimental Investigation of Shock Effects in Porous Meteoritic and Terrestrial Materials <i>John T. Wasson and William J. Nellis</i>	77
---	----

The Development of Preferred Orientation in Ice Investigated by Neutron Diffraction <i>Hans-Rudolph Wenk, William B. Durham, and Kristin Bennett</i>	80
---	----

Melting of Ni and Pt at Ultrahigh Pressure: A Unique Interlaboratory Comparison <i>Raymond Jeanloz, William J. Nellis, and Abby Kavner</i>	82
---	----

## *Astrophysics* 84

Atmospheric Characterization for Adaptive Optics <i>Stanley M. Flatté, Claire E. Max, and L. William Bradford</i>	84
--	----

The r-Process in Supernovae and Parameterized Nucleosynthesis <i>Stanford E. Woosley, Grant J. Mathews, James R. Wilson, and Robert D. Hoffman</i>	88
---	----

Dark Matter Neutrinos, Weak Interaction Physics, and Supernova Dynamics and Nucleosynthesis <i>George M. Fuller, Grant J. Mathews, James R. Wilson, Ron Mayle, and Gail C. McLaughlin</i>	91
--	----

Numerical Studies of Fragmentation in Star-Forming Regions <i>Christopher F. McKee, Richard I. Klein, John Bell, Louis H. Howell, Jeffrey Greenough, and John H. Holliman II</i>	93
---	----

Dust-Driven Winds from Pulsating, Late-Type Stars <i>Mark Morris, John I. Castor, and Nickolaos Mastrodemos</i>	95
--	----

---

**Section IV. IGPP–LLNL Seminars and Workshops**\_\_\_\_\_ 99

Center for Geosciences \_\_\_\_\_ 99

Center for High-Pressure Sciences \_\_\_\_\_ 101

Astrophysics Research Center \_\_\_\_\_ 103

---

**Section V. Bibliography**\_\_\_\_\_ 109

---

**Section VI. Fiscal Year 1995 IGPP–LLNL University  
Collaborative Research Program**\_\_\_\_\_ 117





## Section I. Overview

The Institute of Geophysics and Planetary Physics (IGPP) is a Multicampus Research Unit of the University of California (UC). IGPP was founded in 1946 at UC Los Angeles with a charter to further research in the earth and planetary sciences and in related fields. The Institute now has branches at UC campuses in Los Angeles, San Diego, Riverside, and Irvine and at Los Alamos and Lawrence Livermore national laboratories.

The University-wide IGPP has played an important role in establishing interdisciplinary research in the earth and planetary sciences. For example, IGPP was instrumental in founding the fields of physical oceanography and space physics, which at the time fell between the cracks of established university departments. Because of its multicampus orientation, IGPP has sponsored important interinstitutional consortia in the earth and planetary sciences. Each of the six branches has a somewhat different intellectual emphasis as a result of the interplay between strengths of campus departments and Laboratory programs.

The IGPP branch at Lawrence Livermore National Laboratory (LLNL) was approved by the Regents of the University of California in 1982. IGPP-LLNL emphasizes research in seismology, geochemistry, cosmochemistry, high-pressure sciences, and astrophysics. It provides a venue for studying the fundamental aspects of these fields, thereby complementing LLNL programs that pursue applications of these disciplines in national security and energy research. IGPP-LLNL is directed by Charles Alcock and is structured around three research centers. The Center for Geosciences, headed by George Zandt and Frederick Ryerson, focuses on research in geophysics and geochemistry. The Center for High-Pressure Sciences, headed by William Nellis, sponsors research on the properties of planetary materials and on the synthesis and preparation of new materials using high-pressure processing. The Astrophysics Research Center, headed by Charles Alcock, provides a home for theoretical and observational astrophysics and serves as an interface with the Physics Department's Laboratory for Experimental Astrophysics and with other astrophysics efforts at LLNL.

The IGPP branch at LLNL (as well as the branch at Los Alamos) also facilitates scientific collaborations between researchers at the UC campuses and those at the national laboratories in areas related to earth science, planetary science, and astrophysics. It does this by sponsoring the University Collaborative Research Program (UCRP), which provides funds to UC campus scientists for joint research projects with LLNL. The goals of UCRP are to enrich research opportunities for UC campus scientists by making available to them some of LLNL's unique facilities and expertise, and to broaden the scientific program at LLNL through collaborative or interdisciplinary work with UC campus researchers. UCRP funds (provided jointly by the Regents of the University of California and by the Director of LLNL) are awarded annually\* on the basis of brief proposals, which are reviewed by a committee of scientists from UC campuses, LLNL programs, and external universities and research organizations. Typical funding for a collaborative research project ranges from \$5,000 to \$25,000 per year. Funds are used for a variety of purposes, including support for visiting graduate students, postdoctoral fellows, and faculty; released-time salaries for LLNL scientists; and costs for experimental facilities and supercomputing time.

---

\* Further information about the University Collaborative Research Program, including guidelines for submitting proposals, may be obtained from Christina Budwine, Operations Manager, IGPP-LLNL, L-413, Lawrence Livermore National Laboratory, P.O. Box 808, Livermore, CA 94551 (telephone: 510-423-4476; e-mail address: budwine2@llnl.gov).

Although the permanent LLNL staff assigned to IGPP is relatively small (presently about seven full-time equivalents), IGPP's research centers have grown into vital research organizations. This growth has been possible because of IGPP support for a substantial group of resident postdoctoral fellows; because of the thirty or more UCRP projects funded each year; and because IGPP hosts a variety of visitors, guests, and faculty members (both from UC and other institutions) on sabbatical leave. To focus attention on areas of topical interest in the geosciences and astrophysics, IGPP–LLNL hosts conferences and workshops. IGPP–LLNL also organizes three seminar series: one in astrophysics, one in high-pressure sciences, and one in the earth sciences. Section IV lists the seminars given in FY 1994.

Figures 1 and 2 give a statistical overview of IGPP–LLNL's UCRP (colloquially known as the mini-grants). Figure 1 shows the distribution of UCRP awards among the UC campuses, by total amount awarded and by number of proposals funded. Figure 2 gives the distribution of awards by center, showing that the awards

*Figure 1.*  
*Distribution of FY*  
*1994 UCRP awards*  
*to UC campuses*  
*from IGPP–LLNL:*  
*(a) funds awarded in*  
*thousands of dollars*  
*and (b) number of*  
*projects funded.*

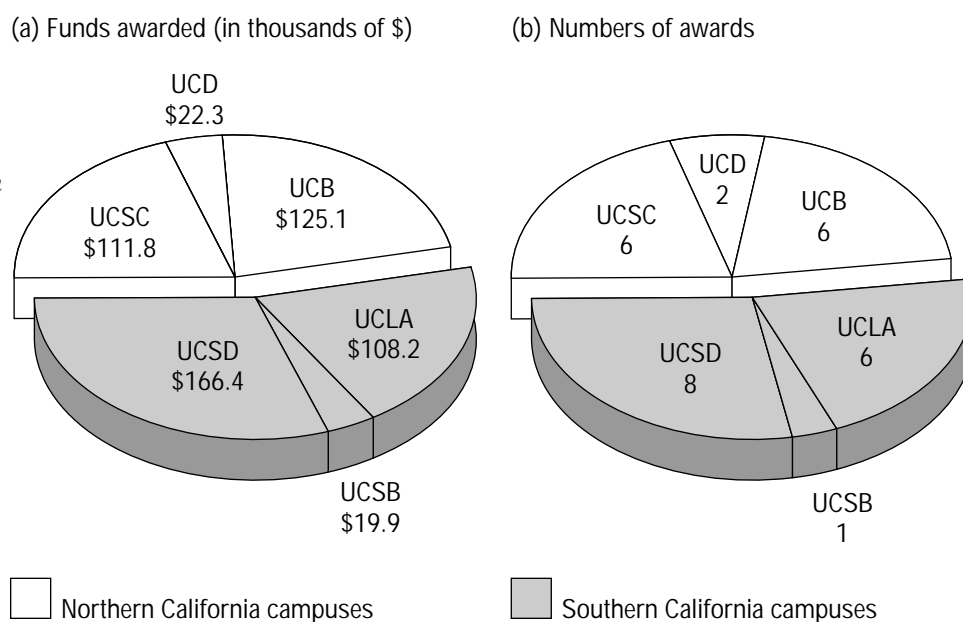
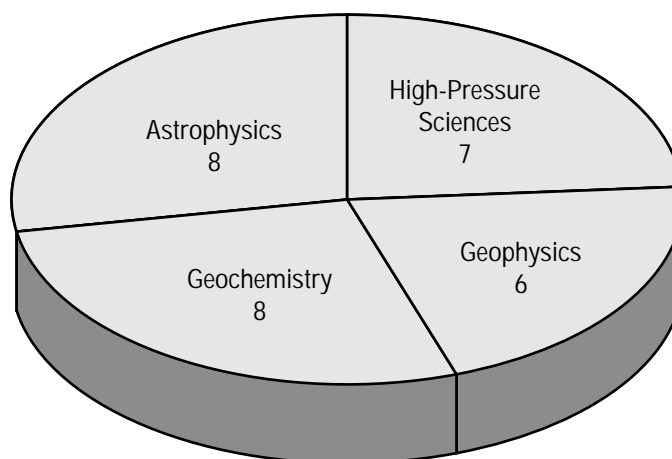


*Figure 2. Distribution*  
*of awards by*  
*IGPP–LLNL center.*



are broadly spread over the areas we support. In addition, IGPP–LLNL hosts an increasing number of scientific visitors. During FY 1994, 31 scientists spent a week or more in residence.

Since FY 1987, IGPP–LLNL has maintained a bibliography of published research papers resulting from UCRP projects and from research by the IGPP’s staff, postdoctoral fellows, and consultants. These lists are published each year in the annual report. Section V gives the bibliography for FY 1994. As a measure of research productivity, the results are gratifying. The abundance of publications from IGPP collaborative projects is a measure of the significance of the results obtained in these projects. This refereed-journal publication rate for IGPP-related projects corresponds to more than 1 paper/year for each faculty member, 2 papers/year for each IGPP postdoctoral fellow, and 2 papers/year for each IGPP staff member. Figure 3 compares the total papers published in refereed journals or conferences for the last four years. (Note that, because of the extensive peer-review process for most scientific journals, several papers submitted by the principal investigators are still in progress. Therefore, we cannot give an accurate total of 1994 papers published until we receive formal notification from the journals and authors.)

To prepare for the future, IGPP–LLNL is exploring new directions in its research. These ventures, some of which are described in this report, include new applications of technologies developed for astrophysics experiments, new directions in geodesy, and the mapping of tectonic movements over long periods by isotope analysis of rock samples.

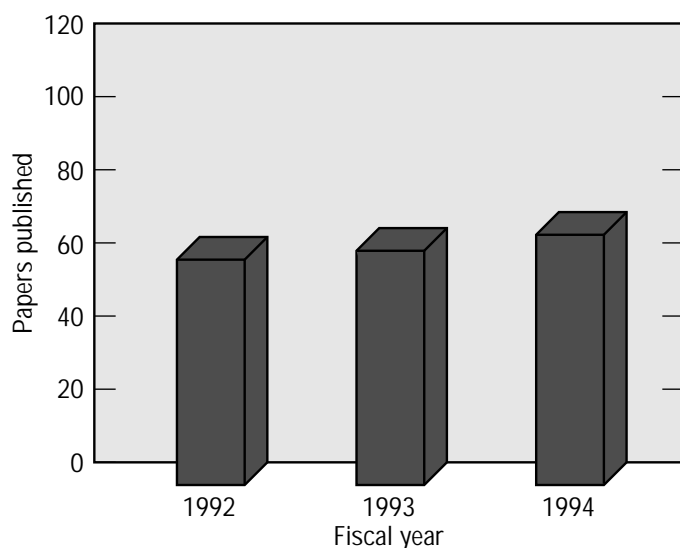


*Figure 3. Total number of papers published in refereed journals and conference proceedings from 1992 through 1994.*



## Section II. Highlights of Fiscal Year 1994

### *Center for Geosciences*

The primary purpose of the IGPP–LLNL Center for Geosciences is to promote collaborative research in the earth sciences between LLNL and UC researchers. Many subdisciplines within the geosciences are employed by LLNL’s mission-oriented programs in national security and energy research. IGPP is able to draw upon these capabilities and expertise and to act as a focal point for research in the more fundamental aspects of these areas. In doing so, we hope to consolidate many unique talents and capabilities at LLNL and provide an easily identifiable avenue for LLNL–UC collaborations. The Center for Geosciences is the physical and scientific focus for interactions with visitors for academic (UC and other universities), industrial, and government geoscience research institutions. The center’s past research emphasis on the physics and chemistry of the solid Earth, including seismology, geochemistry, experimental petrology, mineral physics, and hydrology, continues along with a recently initiated effort in interdisciplinary studies of active tectonics.

The center is located in and partially supported by the LLNL Earth Sciences Department. It has strong ties with several programs within the Earth Sciences Department as well as the Isotope Sciences Division of Chemistry and Materials Science, which is a major contributor of scientific expertise and facilities supporting collaborative efforts in geochemistry. The center provides access to computational, experimental, and analytical research facilities and supports fieldwork for geophysical and geochemical studies.

Operational responsibilities for the center are shared by George Zandt and Rick Ryerson. Zandt is a seismologist with interests in upper mantle and crustal structure and tectonics and in developing seismic underground imaging techniques. He provides oversight for research projects in seismology and observational geophysics. Ryerson is a petrologist with interests in diffusion in rock-forming minerals, rheology of partially molten crustal rocks, and high-pressure and high-temperature mineral-melt phase equilibria. He provides oversight for projects in geochemistry, mineral physics, and experimental geophysics and is also actively involved in field studies in Tibet and southeast Asia.

The Center for Geosciences is located in an area with minimal access controls, thus allowing university collaborators ready access to LLNL computational facilities. This area houses the center’s library and several computer workstations for use by visitors and staff, and it is the focus of our activities in seismology and geophysics. State-of-the-art seismological field equipment is available for collaborative studies. Portable broadband seismic stations can be deployed worldwide to provide data for crustal and mantle structure investigations in difficult access terrains.

Research in geochemistry and experimental geophysics takes place in the Earth Science and Isotope Sciences facilities. The Isotope Sciences facility houses an ion microprobe, an electron microprobe, an inductively coupled plasma (ICP) mass spectrometer, and clean laboratory facilities for preparing accelerator mass spectrometry (AMS) samples. The Earth Science experimental facilities include apparatus for high-pressure gas media deformation experiments; piston cylinder and multi-anvil laboratories; and laboratories for electrical conductivity measurements, crystal growth, diamond cell experiments, and cryogenic deformation experiments. In addition, we have laboratories for x-ray diffraction analysis and infrared spectroscopy.

## Research Highlights

The Center for Geosciences has developed a research program to study the physics and chemistry of the solid Earth, including seismology, geochemistry, experimental petrology, mineral physics, hydrology, and active tectonics. The following pages give a summary of some of this research.

### Seismic Exploration of the Deep Altiplano

We are participating in an ongoing deployment of a passive source, broadband, seismic experiment in the central Andean Cordillera of Bolivia and northern Chile. This is an international, multi-institutional experiment with participants from LLNL, the University of Arizona, the Carnegie Institution of Washington, and San Calixto Observatory of La Paz, Bolivia. The main LLNL participants are George Zandt (the principal investigator), IGPP postdoctoral fellows Stanley Ruppert and Annie Kersting, and chief project engineer Don Rock. The main scientific objective is to extend our understanding of the deep structure and tectonics of the central Andean Cordillera and in particular the Altiplano plateau, the world's highest plateau associated with ocean-continent subduction. The passive source experiment consists of a 16-station, east–west transect called the Broadband Andean Joint (BANJO) Experiment and a 7-station, north–south transect called the Seismic Exploration of the Deep Altiplano (SEDA) Experiment. The equipment for BANJO is provided by the Incorporated Research Institutions for Seismology (IRIS) and the Carnegie Institution of Washington, and the experiment is funded by the National Science Foundation. The equipment for SEDA is provided by LLNL, and the project is funded by the Department of Energy.

We deployed 7 broadband seismic stations in Bolivia extending from La Paz to Uyuni ( $\sim 17^\circ$  to  $20.5^\circ\text{S}$ ). The roughly north–south transect lies along the eastern edge of the Altiplano between  $67^\circ$  and  $68^\circ\text{W}$  and intersects the east–west BANJO broadband deployment near  $19^\circ\text{S}$ . The 7 SEDA stations, the 4 BANJO stations on the Altiplano, and the IRIS station LPAZ combine to form a 12-station broadband network to investigate the deep structure of the Altiplano (Figure 1). However, before we could start our structural studies, something remarkable happened. On June 9, 1994, less than two months after we had installed the network, a magnitude 8.3 earthquake occurred 636 km beneath northern Bolivia. This was the largest deep earthquake to occur since modern seismic stations have been installed, and we recorded it with our portable broadband array.

Using all available data for the mainshock and our data for the aftershocks, we determined that the earthquake occurred on a nearly horizontal fault within the subducting Nazca Plate, and the rupture propagated bilaterally across the width of the slab. The fault area we inferred from analyzing the waveforms is about 40 km by 50 km, and the rupture propagated at a velocity of 1 to 2 km/s, which is remarkably slow. We identified only 36 aftershocks ( $M > 2$ ) in the 10 days following the mainshock. The aftershocks occurred mostly beneath the main fault plane in an area measuring 60 km by 60 km by 35 km, with predominantly normal faulting mechanisms. The volume of the seismogenic zone is much larger than previously predicted by the transformational faulting mechanism and thus throws open the question about the faulting mechanism for deep earthquakes.

We are analyzing teleseismic events and local slab earthquakes, so we can explore the lithospheric structure of the Altiplano and investigate the anisotropy of the Altiplano mantle. Local, deep-focus events were used to compute receiver functions so we could isolate P-to-S converted phases from major lithospheric discontinuities beneath each station. Large Moho Ps conversions arrived about 8 to 10 s after the P waves at all stations, thus indicating that the crustal thickness varies from

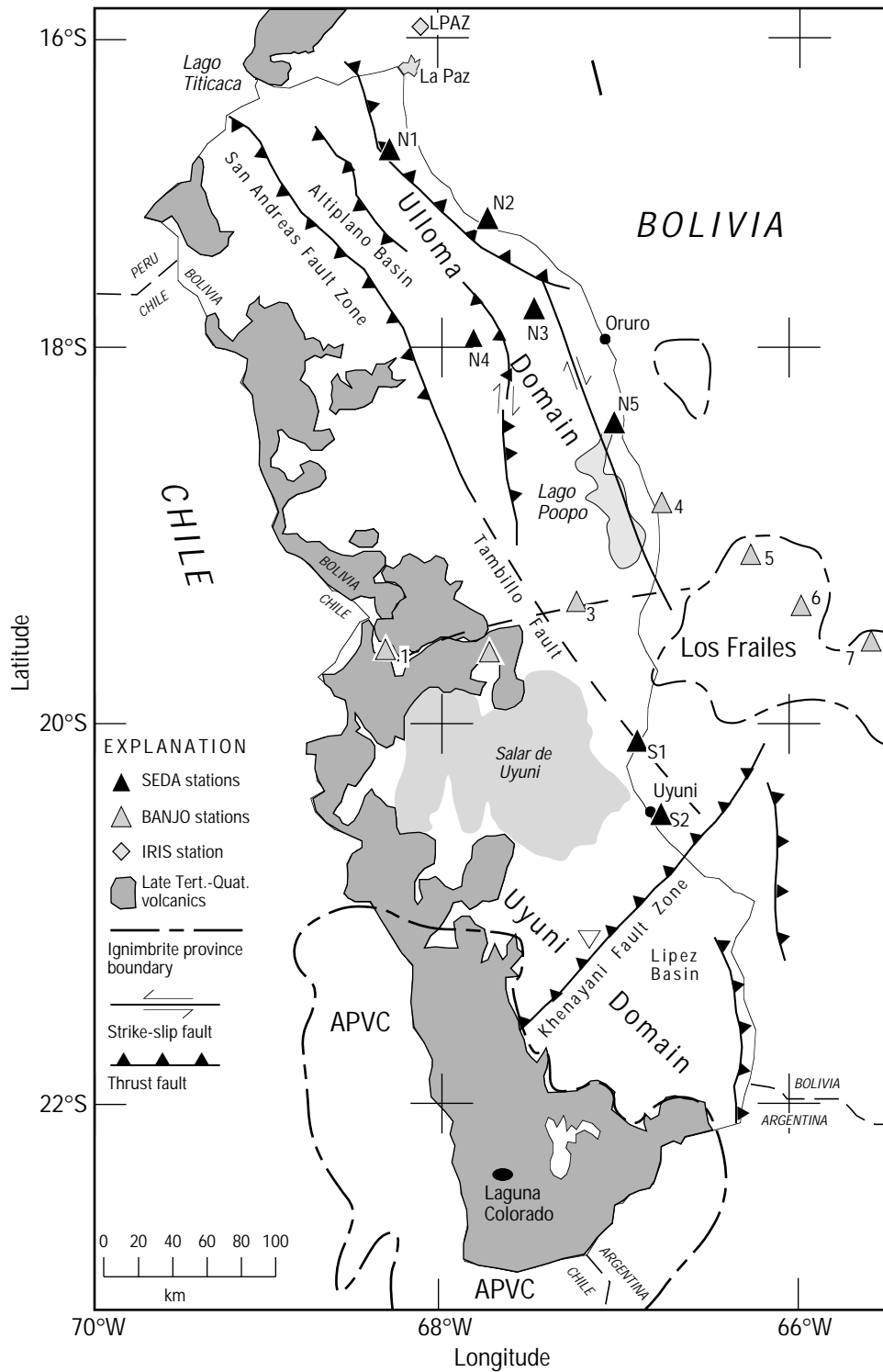


Figure 1. Map of SEDA stations and western BANJO stations in Bolivian Altiplano. Late Cenozoic volcanics and ignimbrite fields are outlined. Base map from Richter et al., 1992.

65 to 80 km. Local, intermediate-depth events generated large S-coupled P waves that propagated in the crustal waveguide. Reflectivity modeling of a pure Altiplano-path profile of waveforms with periods  $> 10$  s is consistent with a crust about 70 km thick, with a 10-km-thick, 5-km/s layer over a 6.2-km/s layer. Higher-frequency waveforms reveal consistent arrivals, which we are attempting to model for more details of the lithospheric structure.

Preliminary results using teleseismic SKS, SKKS, and deep-focus ScS events revealed significant upper-mantle anisotropy. The fast polarization direction is approximately west-northwest–east-southeast for the northern stations and changes to north-northwest–south-southeast under the southern stations, following the curvature of the trench and the Andean Cordillera. All of the SEDA stations exhibit delay times between 0.75 to 0.95 s. Further analyses of slab events and converted crustal phases are required to separate the effects of anisotropy within the thick crust, the mantle wedge above the slab, and the mantle beneath the slab.

## Southern Sierra Nevada Continental Dynamics Project

Mount Whitney, located within the Sierra Nevada in central California and the highest peak in the conterminous United States, lies less than 150 km from the lowest point—Death Valley. Until now, crustal thickness and upper-mantle velocities beneath the region were poorly understood, complicating the study of tectonic processes responsible for the recent uplift of the Sierra Nevada. Two end-member models have been proposed: a thick, Airy-isostatic mountain root or a thin crust overlying an anomalous mantle that provides isostatic compensation. Previous seismic investigations of the Sierran crust and mantle were unable to resolve these two tectonic processes. However, in analyzing the seismic-refraction travel-time and amplitude data collected during the 1993 Southern Sierra Nevada Continental Dynamics (SSCD) project, we found a region of local crustal thickening, with a crustal welt about 40 km thick, centered 80 km west of the Sierran topographic crest (Figure 2) and thin crust beneath the highest Sierran topography. Because the P velocities are low and there is no thick isostatic crustal root centered beneath the Sierran crest, we concluded that the recent uplift of the Sierra Nevada is most likely

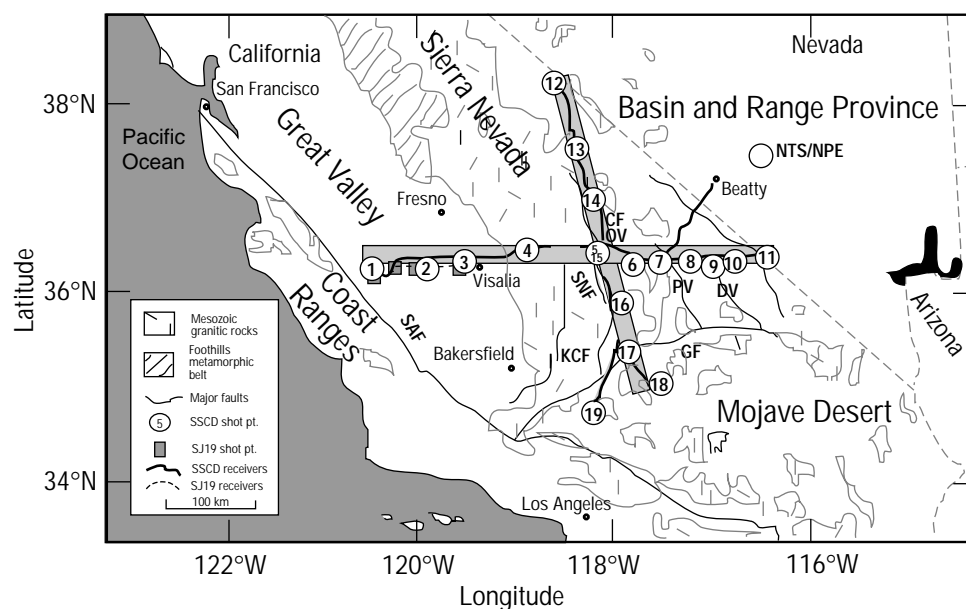


Figure 2. Location of the SSCD seismic refraction profiles. The Non-Proliferation Experiment (NPE) was fired at the Nevada Test Site and recorded on instruments in the west–east line. Tectonic features shown are the Sierra Nevada batholith and metamorphic belt. The major fault lines shown are San Andreas Fault (SAF), Garlock Fault (GF), Kern Canyon Fault (KCF), Sierra Nevada Fault (SNF), Furnace Creek Fault (Death Valley, DV), and Panamint Valley Fault (PV).



due to asthenospheric upwelling, lithospheric thinning, or a combination of both processes beneath the southeastern Sierra Nevada and Basin and Range.

The Sierra Nevada, composed mainly of Mesozoic intrusive rocks of the Sierran Batholith and remnant metamorphic rocks (Figure 3), has most likely been uplifted and tilted at least 2 km during the last 10 million years. Since most of the high topography of the Sierra Nevada (3 to 4 km) exists in isostatic equilibrium, some form of mass deficit must exist within either the crust or upper mantle beneath the region that is large enough to compensate the range isostatically. Because there is a delay between the presumed Mesozoic development of the batholith as well as any isostatic crustal root and the late Cenozoic uplift, we have proposed that a strong lithosphere prevented significant uplift until the lithospheric plate was broken by encroaching Basin and Range extension.

Another proposal to explain the Sierran uplift is during the Cenozoic, the lithosphere thinned as the Mendocino Triple Junction migrated northward. Then the oceanic lithosphere was replaced by hot buoyant asthenosphere beneath the Sierra Nevada. In this project, we used previous refraction profiles to interpret both thick (>50 km) crust and normal (about 8.0 km s<sup>-1</sup>) upper-mantle velocities. Similar refraction data were also used to interpret thin (about 30 to 35 km) crust overlying a low-velocity (7.6 to 7.9 km s<sup>-1</sup>) and presumably warm buoyant upper mantle. However, since the Sierra Nevada has a low apparent heat flow (<1.5 HFU), we cannot distinguish between the crustal-root hypothesis and the active upper-mantle hypothesis because the thermal time constant for the crust exceeds the age of uplift.

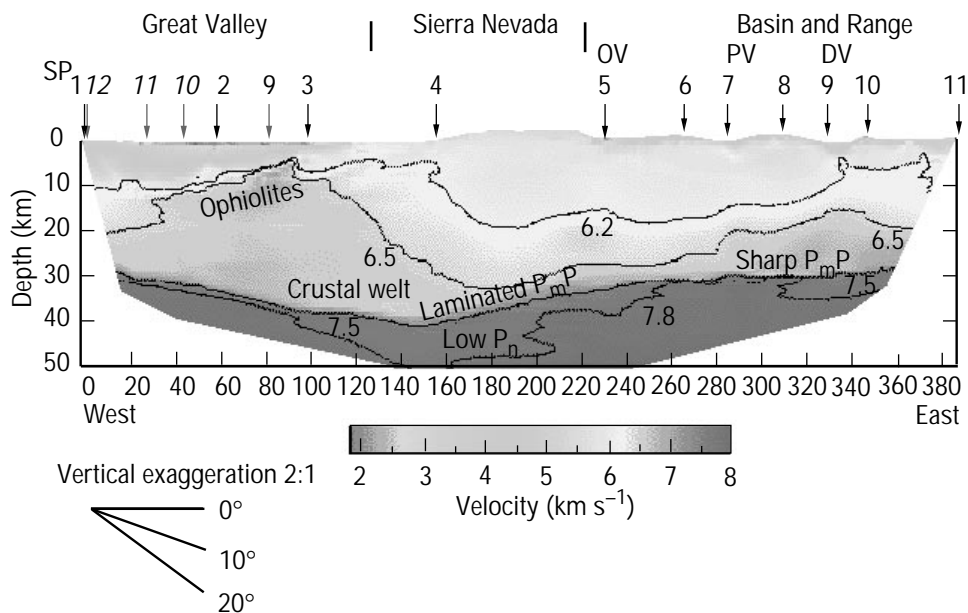


Figure 3. Final crustal model for the west-east refraction profile. Only those portions of the velocity model that have ray coverage are shown. A local crustal thickening (crustal welt) is centered beneath the western Sierra Nevada near seismic profile (SP) 4 on the east-west profile. Thinner crust is present beneath the highest topography of the Sierran crest near model coordinate 215. Between SP 4 and 5, the Moho is interpreted to be laminated (alternating high- and low-velocity layers), giving rise to a reverberatory P<sub>m</sub>P. Between SP 2 and 3, a west-dipping wedge of high velocity (6.8 to 7.1 km s<sup>-1</sup>) material beneath the Great Valley sedimentary rocks is interpreted to be ophiolites. The Sierran batholith lower crust has an average velocity of 6.3 to 6.5 km s<sup>-1</sup>, whereas the Basin and Range lower crust east of Panamint Valley has a higher average velocity of 6.7 to 7.0 km s<sup>-1</sup>.

One of our main objectives of the SSCD project is to resolve the controversy around the crustal structure of the Sierra Nevada and associated tectonic processes driving the uplift. To achieve this goal, we collected a broad range of geologic and geophysical data, including passive and active seismic, gravity, and magnetotelluric data. The main seismic survey consisted of two crossing lines, with 19 inline chemical explosions (shots) separated by about 50 km and ranging from 500 to 4000 kg. Maximum shot-receiver offset is 330 km in the north-south line and 390 km in the west-east line (Figure 3). Additionally, a 480-km-long west-east profile for the 1-million-kg chemical explosion for the Department of Energy's Non-Proliferation Experiment (NPE) was recorded from Beatty, Nevada, west across the Sierra Nevada along the previously deployed west-east profile, continuing nearly to the Pacific Ocean.

Up to 675 seismic recorders were installed along the ground surface for each seismic profile. Nominal receiver spacing was about 500 m for the crossed profiles and 1500 m for the NPE profile. We compared the detailed two-dimensional (2D) interpretation of the observed  $P_g$ ,  $P_n$ , and  $P_mP$  seismic phases for all inline shots with an upper-mantle P-wave delay model. We also completed a three-dimensional (3D) crustal interpretation and a Moho depth map and gravity interpretation, using the 2D profiles plus additional fan shots and the NPE data.

Using a 2D, finite-difference travel-time inversion of  $P_g$  and  $P_n$  arrivals, we resolved upper-crustal velocities of 6.0 to 6.4 km s<sup>-1</sup> within the Sierran batholith and Basin and Range; an upper-crustal, west-dipping wedge with velocities of 6.8 to 7.2 km s<sup>-1</sup>, which is consistent with ophiolitic material, underlying the Great Valley sedimentary sequence; and different crustal velocities beneath the Basin and Range (6.8 to 7.0 km s<sup>-1</sup>) than those beneath the Sierran batholith (6.6 km s<sup>-1</sup>). Low average  $P_n$  velocities (7.6 to 7.9 km s<sup>-1</sup>) and a laminated transitional Moho imaged beneath the Sierran batholith also differ from the higher  $P_n$  velocities (7.9 to 8.0 km s<sup>-1</sup>) and the sharp first-order Moho observed beneath the Basin and Range.

Crustal-thickness variations beneath the Sierran batholith are derived from travel-time modeling of well-recorded  $P_mP$  reflected arrivals and imply a crustal welt with a maximum thickness of 42 to 44 km centered beneath the western Sierra Nevada. The crust thins westward beneath the Great Valley to 28–34 km thick; it thins eastward beneath the highest Sierran topography to 35 km thick into the Basin and Range, where it is 27 to 30 km thick. Crustal thickness increases southeast to northwest from 27–29 km beneath the Garlock Fault to 38–44 km beneath the north end of Owens Valley.

A density model derived from the crustal velocity model but with constant mantle density satisfies the pronounced negative Bouguer anomaly associated with the western Sierra Nevada. However, it shows a large discrepancy in the eastern Sierra Nevada, increasing to 100 mgal in the Basin and Range Province. Unfortunately, we cannot match the observed gravity with anomalies in the crust alone with realistic densities. A contribution from the upper mantle, either by lateral density variations or by a thinning of the lithosphere under the Sierra Nevada and the Basin and Range, is required for a physically plausible model. The region of low  $P_n$  velocities and the absence of a thick isostatic crustal root centered beneath the Sierran crest suggest that the recent uplift of the Sierra Nevada is caused by asthenospheric upwelling, lithospheric thinning, or a combination of both processes beneath the southeastern Sierra Nevada and Basin and Range.

The SSCD Working Group includes P. E. Malin (Duke University); S. K. Park (UC Riverside); S. Ruppert (LLNL); G. Jiracek (San Diego State University); R. A. Phinney (Princeton University); J. B. Saleeby, B. Wernicke, R. Clayton, and L. Squires (California Institute of Technology); R. Keller and K. Miller (University of Texas at El Paso); C. Jones (University of Nevada at Reno); W. D. Mooney, J. H. Luetgert, and H. Oliver (U.S. Geological Survey); S. L. Klemperer and G. A.

Thompson (Stanford University); and F. Monesterio (China Lake Geothermal Office, Department of the Navy). Funding sources include the National Science Foundation, the U.S. Department of Energy (BES and IGPP), the U.S. Department of Defense, and the U.S. Geological Survey.

## Red River Shear Zone

Identifying and determining the relative importance and temporal variability of the mechanisms responsible for accommodating convergence during the Indo-Asian collision is fundamental to understanding the geologic evolution of Tibet and the Himalaya. For example, researchers have established that part of the Tertiary convergence was absorbed by intracontinental thrusts in the Lesser Himalaya, Tethyan Himalaya, and Indus-Tsangpo suture zone. Although some have speculated that similar amounts of thrust-related thickening occurred throughout Tibet during the Tertiary, relatively little has been securely documented. Complicating simple thickening models is the proposal that continental extrusion accommodated some fraction of the convergence of India with Eurasia after 50 Ma.<sup>1-3</sup> Although the two deformational styles are not exclusive of one another, they reflect disparate views of the response of continental lithosphere to tectonic forces. Therefore, many researchers who are attracted to pure thickening models have questioned whether predictions of the extrusion hypothesis have been borne out.

Because the Tertiary tectonic evolution of the Red River Shear Zone (RRSZ) is a key prediction of the hypothesis that extrusion of Indochina accommodated a significant portion of Indo-Asian convergence, this feature has been the focus of considerable attention in recent years. Traceable from Tibet through Yunnan to the South China Sea (Figure 4), this belt had previously been interpreted as either a purely right-lateral fault or a suture of Proterozoic age, Paleozoic age, or Triassic age. However, in our studies (Rick Ryerson, IGPP-LLNL, and Mark Harrison, IGPP-UCLA) and those by our colleagues Paul Tapponnier, Herve Leloup, and Urs Sharer (Institut de Physique du Globe de Paris) and Chen Wenji and Li Qi (Chinese State Seismological Bureau), we found that the RRSZ is a Tertiary, ductile, strike-slip shear zone with a left-lateral offset greater than 80 km.

The elongated massifs in Vietnam and Yunnan that define the RRSZ contain metamorphic rocks that have been ductilely deformed in a left-slip sense. In the continental extrusion hypothesis, the South China Sea is interpreted to be a pull-apart basin at the southeastern termination of the RRSZ that opened as a result of strike-slip motion. Magnetic stripes in the South China Sea<sup>4</sup> are consistent with a left-lateral offset along the RRSZ of about 550 km occurring during seafloor spreading between 32 and ~16 Ma. This is compatible with a minimum displacement of  $330 \pm 60$  km estimated from boudinage restoration within the gneiss massifs.<sup>5</sup> The sense of motion on the RRSZ reversed at 5 Ma, becoming right-slip with normal throw in places.

In FY 1994, we collected new  $^{40}\text{Ar}/^{39}\text{Ar}$  and stable isotopic results from the RRSZ in Yunnan and Vietnam, to augment the data

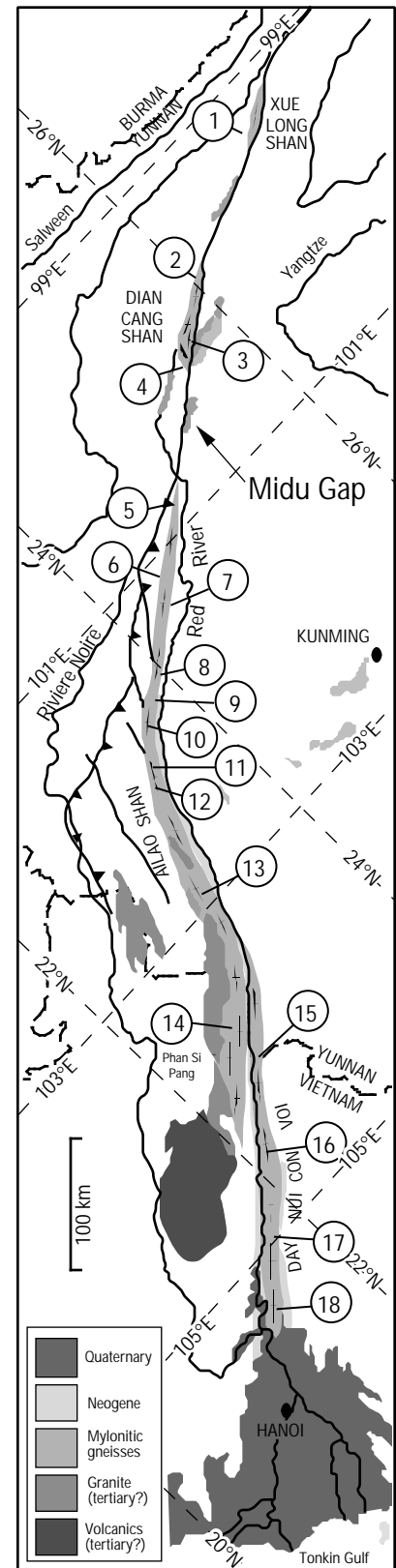


Figure 4. Simplified geologic map of the Red River Shear Zone. The sample locations are indicated by the circled numbers.

previously collected in this project. These results are used to constrain models of the thermal and mechanical evolution of the RRSZ. We also analyzed  $^{40}\text{Ar}/^{39}\text{Ar}$  data for K-feldspars from 10 transects perpendicular to the northwest–southeast strike of the Ailao Shan (Figure 4), the longest massif in the chain. These data help us determine the thermal histories for each location and yield a pattern of ages consistent with diachronous initiation of transtensional faulting (extension) along the RRSZ. The normal component of this faulting occurs along the eastern boundary of the shear zone, the locus of the active Range Front fault.

Numerical modeling of isotopically derived cooling histories yields a dip-slip rate of  $\sim 6$  mm/year. A 400-km-long segment of the Ailao Shan reveals a pattern of ages that increase smoothly from 17 Ma in the northwest Ailao Shan to 25 Ma in Vietnam. Figure 5 shows time versus distance (from the Gulf of Tonkin) for the 200, 300, and 400°C isotherms from samples along the eastern edge of the shear zone. These isotherms clearly demonstrate that the extension is younger at its northwest end than at its southeast, which thus allows us to determine the rate of onset of extension. This relationship indicates that the onset of extension was diachronous, beginning in the southeast and propagating northwest at a rate of  $\sim 4.5$  cm/year.

This rate and the spatial and temporal variability of extension are consistent with predictions, based on Oligocene–Early Miocene magnetic anomalies from the South China Sea, that the RRSZ experienced strike-slip rates of  $\sim 4$  cm/year. Thus, its present position does not represent a small circle about the Indochina–South China poles of rotation. As a consequence, a strike-perpendicular component of compression would have existed in the northern portion of the belt, with an increasing component of strike-perpendicular extension to the southeast across the Ailao Shan. The general shallowing of foliation from northwest to southeast across the Ailao Shan is consistent with this prediction.

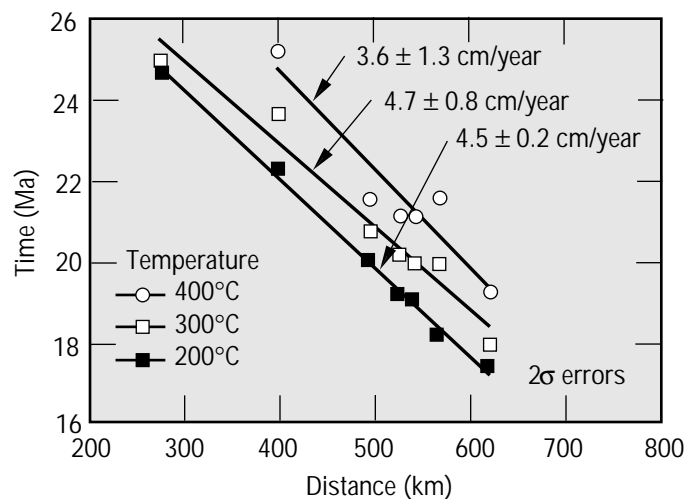


Figure 5. Plot of the age of rapid cooling as evidenced from K-feldspar-derived thermal histories reaching temperatures of 400, 300, and 200°C, against distance along strike of the Ailao Shan–Red River Shear Zone. The correlation indicates an age vs distance relationship of  $\sim 4.5$  cm/year. It is argued that this is due to the propagation of the brittle-ductile transition from southeast to northwest at a rate corresponding to the strike-slip motion on the RRSZ.

## Island-Arc Petrogenesis and Implications for Chemical Recycling

Island-arc volcanoes are the dramatic result of continuous and dynamic interaction between the downgoing oceanic slab, the overlying mantle wedge, and the lithospheric mantle and crust of the Earth. This tectonic environment marks the principal area for the return of the Earth's crust to the mantle from which it was once derived. Thus, island arcs are key areas of focus for studies aimed at understanding the evolution of the Earth's crust and upper mantle. In terms of chemical mass balance, the interactions between the subducting component (the oceanic crust, sediment, and fluid), the overlying mantle, and the lithosphere are far from understood. For example, there is controversy about determining (1) whether sediments deposited on the seafloor are carried down with the subducted oceanic crust and if so, are they melted and recycled into the arc crust via magmatism or transported into the deep mantle; (2) the chemical nature of the fluids and/or melts resulting from dehydration of the subducting slab and understanding their importance in the chemical mass transfer process; and (3) the role of the lithosphere in altering the chemistry of island-arc magmas.

The isotopic composition of the mantle, subducting oceanic crust, oceanic sediments, overlying mantle wedge, and arc lithosphere can be distinct and thus offers the potential of being used as geochemical tracers to more precisely quantify the recycling process between the Earth's mantle and crust. To gain a better understanding of the net chemical fluxes involved in recycling in island-arc settings, Annie Kersting (IGPP-LLNL) has been working on two related aspects of island-arc genesis. The first project is to evaluate the contribution of the subducting slab and oceanic sediments to the generation of island-arc volcanoes in Kamchatka. The second project is designed to understand the chemical influence of the lithosphere to the diversity of island-arc magmas from a transect of volcanoes in Honshu, Japan (Figure 6).

Trace-element, radiogenic, and stable isotope (Pb, Nd, Sr, O) data were collected on a suite of basalts from the world's most active island-arc volcano, Klyuchevskoy, Kamchatka, Russia. Pb isotopic ratios ( $^{206}\text{Pb}/^{204}\text{Pb}$ ,  $^{207}\text{Pb}/^{204}\text{Pb}$ , and  $^{208}\text{Pb}/^{204}\text{Pb}$ ) and Sr isotopic ratios ( $^{87}\text{Sr}/^{86}\text{Sr}$ ) were also measured, using LLNL's

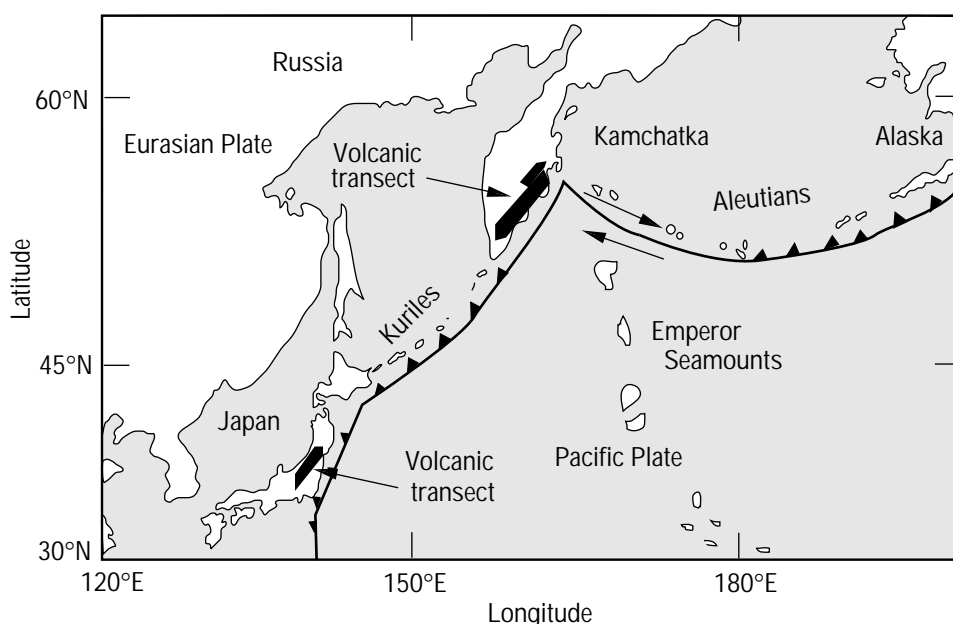
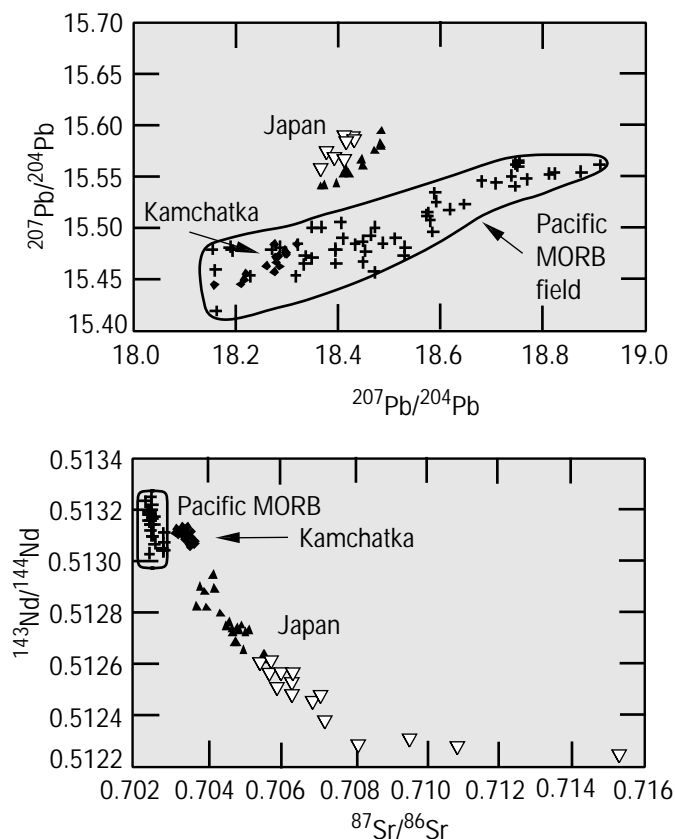


Figure 6. The location of the transect of volcanoes in Honshu, Japan, and Kamchatka, which are designated by a black bar. Triangles indicate the direction of the subducting Pacific Plate.

thermal ionization mass spectrometry facilities. The Pb, Sr, and Nd isotope data show that the Klyuchevskoy lava source is similar to Pacific mid-ocean ridge basalt (MORB) mantle and that sediments are not involved in the generation of these lavas. In terms of Pb isotopes, the Klyuchevskoy lavas are among the most unradiogenic island-arc lavas measured to date. To determine if the results from the Klyuchevskoy study are representative of the Kamchatkan arc, Kersting expanded her study to include four additional Quaternary volcanoes. The Pb, Sr, and Nd isotope data of the five Quaternary volcanoes are similar (Figure 7). In comparison to other island arcs, Kamchatka represents an end member wherein little or no sediment is involved in terms of elemental recycling and arc magma genesis. This work clearly demonstrates that no single generalized model can explain the diversity of processes in island arcs. It also points out the need for detailed study of individual island arcs rather than relying solely on similarities to guide our understanding of island arcs.

To address the influence of the lithospheric component on the diversity of island-arc magmas, Annie Kersting, Richard Arculus (Australian National University), and Ikuo Kushiro (University of Tokyo) collected rock samples from 13 primarily basaltic volcanoes in Honshu, Japan. The northeast-southwest transect of arc volcanoes crosscut a major tectonic boundary where two different crustal terrains are juxtaposed. In northern Honshu, Japan, the Tanakura tectonic line (TTL) crosscuts the recent transect of volcanoes. The proximity of the Quaternary volcanoes minimizes any variation in depth to the subducting slab, in distance to the trench axis, or in composition of the subducting sediments, oceanic crust, and overlying mantle. Therefore, isotopic and elemental distinctions that are coincident with the TTL must reflect differences in the contribution from the lithosphere. The volcanoes show

Figure 7. The Pb, Sr, and Nd isotopic data for the five Quaternary volcanoes: solid diamond = Kamchatkan volcano; solid triangles = volcanoes north of the TTL, Japan; open triangles = volcanoes south of the TTL; and crosses = Pacific MORB values.



along-strike geochemical differences coincident with the TTL (Figure 7). The volcanoes south of the TTL (shown in open triangles) have elevated Pb and Sr isotopic ratios and lower Nd isotopic ratios compared with the volcanoes to the north (solid triangles). Distinct differences in trace-element ratios such as Ce/Yb have also been observed between the two volcanic groups. The chemical and isotopic distinctions observed between the volcanoes north and south of the TTL must reflect crustal contributions. The different geochemical signatures between the volcanoes immediately north and south of the TTL result from contamination as the magmas traverse through chemically distinct crusts.

## Mineral–Melt Partitioning

Observed secular disequilibria among the uranium ( $^{238}\text{U}$  and  $^{235}\text{U}$ ) decay series nuclides have received a great deal of attention as tracers of mantle melting processes. Since the half-lives of the intermediate nuclides are short relative to the time scale of mantle evolution, we can assume that these nuclides are in secular equilibrium when melting begins. These nuclides are unlike many of the other isotopic and elemental tracers in basalts, which are products of processes that influence the source both before and after melting begins. Therefore, secular disequilibria among the uranium decay series nuclides are largely a function of melting and melt–migration processes.

Before we can fully use the temporal information contained in uranium decay series disequilibria and further constrain the processes responsible for the observed disequilibria, we must better understand the partitioning of parent and intermediate nuclides among the various mineral, fluid, and melt phases comprising the mantle, in terms of both composition and external variables. Therefore, in this project, we collected experimental data on the partitioning of U, Th, Pb, Sr, Zr, and Ba (an analog for Ra) between clinopyroxene and a haplobasaltic melt and between amphibole and an andesitic melt at near-natural abundance levels. Participants in this study include Craig Lundstrom, Quentin Williams, and James Gill (UC Santa Cruz) and Henry Shaw, James Brennan, Douglas Phinney, and Rick Ryerson (LLNL).

The partition coefficients for Th, U, and Zr between clinopyroxene and melt show a strong dependence on the Al and Na content of the clinopyroxene (Figure 8). A good correlation between  $^{\text{IV}}\text{Al}$  and  $D_{\text{Th}}$  exists for all recent Th partitioning studies, providing a simple explanation for the 2-order-of-magnitude variation in  $D_{\text{Th}}$  observed in this and previous studies.<sup>6–8</sup> The tetrahedral Al content of the pyroxene is

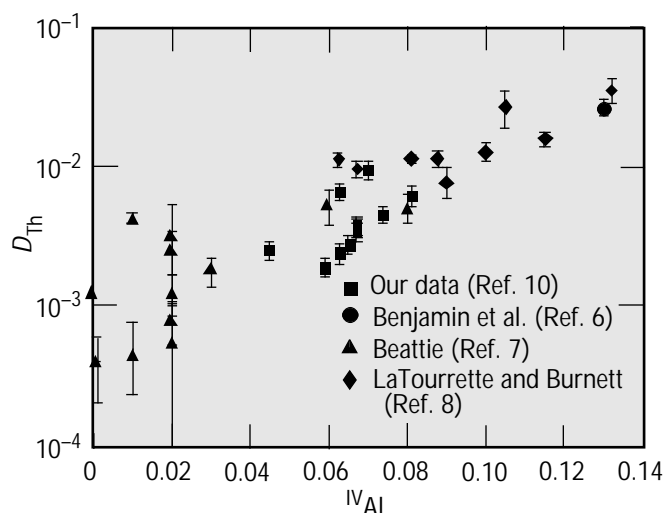


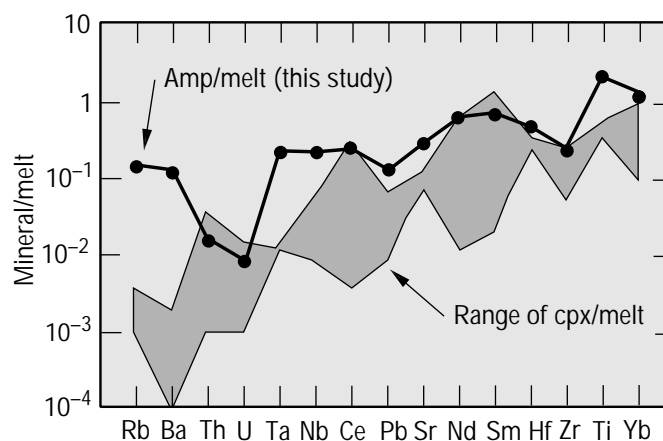
Figure 8.  $D_{\text{Th}}$  vs  $^{\text{IV}}\text{Al}$  for the experiments of Benjamin et al.,<sup>6</sup> Beattie,<sup>7</sup> LaTourrette and Burnett,<sup>8</sup> and our data,<sup>10</sup> where  $\log D_{\text{Th}} = -3.1 + 11.5 \times ^{\text{IV}}\text{Al}$  and  $R^2 = 0.74$ .

a strong indicator of the relevant partition coefficient for Th and U. Because mantle clinopyroxenes generally have greater than 5 wt%  $\text{Al}_2\text{O}_3$ , we suggest that relevant partition coefficients for U and Th are between 0.01 and 0.02. Although variations in Al and Na in clinopyroxene affect the absolute value of the Th and U partition coefficients, they have no effect on their ratio,  $D_{\text{Th}}/D_{\text{U}}$ . Our results reinforce the inference that equilibrium partitioning of U and Th between clinopyroxene and melt cannot explain the observed  $^{230}\text{Th}$  excesses in basalts. Indeed, under the oxygen fugacities relevant to mid-ocean ridge basalt (MORB) petrogenesis, clinopyroxene has little ability to fractionate U from Th ( $D_{\text{Th}}/D_{\text{U}} < 2$ ), implying that chemical disequilibrium between melt and wallrock during transport is not required to preserve  $^{230}\text{Th}$  excesses generated in the garnet stability field. If the Ba partition coefficient serves as an analog for Ra and the partition coefficient of  $\text{U}^{+5}$  serves as an analog for  $\text{Pa}^{+5}$ , then  $^{226}\text{Ra}$  and  $^{231}\text{Pa}$  excesses can be generated by clinopyroxene–melt partitioning.

Using compositionally dependent partition coefficients, we constructed a melting model demonstrating that equilibrium porous flow is a viable explanation for the magnitudes and differences of U-series disequilibria between N-MORBs and E-MORBs from the East Pacific Rise.<sup>9</sup> Indeed, unlike previous modeling, we can explain quantitatively the magnitudes of all the U-series excesses using geophysically reasonable parameters. Moreover, the  $^{231}\text{Pa}$ – $^{230}\text{Th}$  correlation may provide a first-order constraint on the depth at which melting commences beneath different ridges.

We also determined amphibole–melt partition coefficients for a wide range of elements and compared them to the range of clinopyroxene–melt data from the literature (Figure 9). Rb, Ba, Nb, and Ta are dramatically less compatible in pyroxene than in amphibole, while other elements such as Th, U, Hf, and Zr have similar compatibilities. Because of these differences, liquids produced by small degrees of partial melting of amphibole-bearing mantle sources or by high-level fractionation of amphibole will have distinctively lower Th-normalized Rb, Ba, Nb, and Ta concentrations than melts from amphibole-free systems. The compatibility of U, Th, and Pb in amphibole decreases in the order  $\text{Pb} > \text{Th} > \text{U}$ . Therefore, partial melting or fractional crystallization of amphibole-bearing assemblages will generate  $^{238}\text{U}$  excesses relative to  $^{230}\text{Th}$  similar in magnitude to those produced by clinopyroxene fractionation. The compatibility of Pb in amphibole relative to U and Th indicates that melt generation in the presence of residual amphibole will lead to long-term enrichment in Pb relative to U and Th in the mantle residue. Therefore, this process cannot produce the depletion of Pb relative to U and Th in the mantle inferred from Pb isotopic studies of MORB and ocean island basalts.

*Figure 9.*  
Comparison of our mineral–melt partitioning data for amphibole (amp) with the range of values determined for clinopyroxene (cpx). Note the affinity of the alkalis for amphibole relative to clinopyroxene.





## Mineral–Fluid Trace-Element Partitioning Relevant to Island-Arc Volcanism

Convergent boundaries are one of the principal sites of mass and chemical recycling on the planet. Driven by lithospheric subduction, the length scales and processes that characterize chemical recycling at convergent boundaries range from the generation and upward migration of volatiles derived from the dehydration of slab components, to mantle anatexis, melt migration, and associated volcanism-plutonism, and to tectonically driven fluid expulsion within accretionary prisms. These processes share an important characteristic—at some level, each can be described as an example of reactive transport, in which a fluid (melt or aqueous/carbonate fluid) reacts with the solid matrix through which it migrates, by porous media or fracture flow. Quantitative understanding of the processes occurring in these regions requires experimental constraints on mineral–fluid partitioning, kinetics of mineral–fluid–melt exchange, and textural equilibrium between minerals–melts and fluids.

The partitioning of trace elements between minerals and fluids at elevated temperatures and pressures is one of the most poorly constrained geochemical variables in subduction zone processes. Therefore, we are investigating the partitioning of the high-field-strength elements U, Th, Nb, Ta, and Zr and of other geochemically important trace elements between aqueous fluids and the minerals that are found in subducted lithosphere and the overlying mantle wedge. Participants in this project include James Brenan, Henry Shaw, Douglas Phinney, and Rick Ryerson (LLNL). The experiments were conducted in a standard piston cylinder apparatus, but using a large-volume (~100-mL), strong capsule that allows a few grains of a mineral to be retrieved from experiments characterized by a high fluid–mineral ratio. This setup allows a known fluid composition to be imposed on the mineral, which is subsequently analyzed using an ion microprobe at LLNL. The result is a mineral–fluid partition coefficient determined at natural, or near-natural, trace-element abundance levels.

Figure 10 summarizes our results for clinopyroxene (cpx), orthopyroxene (opx), garnet, olivine, and amphibole. Using these mineral–fluid partition coefficients, we can calculate the compositions of fluids that coexist with lherzolite- and eclogite-mineral assemblages (relevant to the mantle wedge and subducted oceanic crust, respectively). Our results indicate that the subarc fluid composition is consistent with a mixture having the chemical and isotopic composition of fluids derived from both altered mid-ocean ridge basalt (~96 wt%) and sediment (~4 wt%). Calculations also

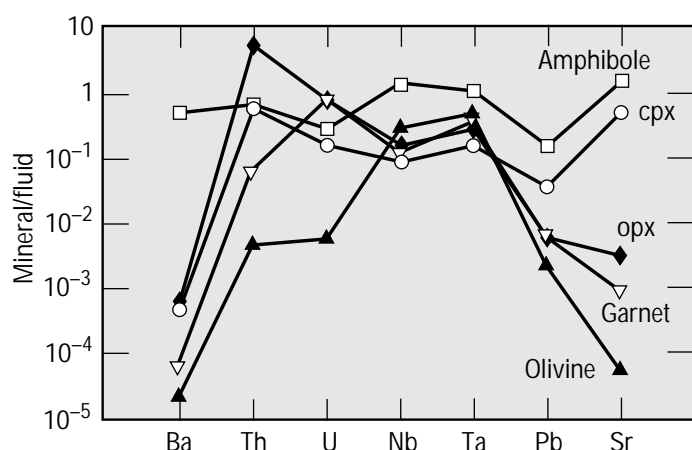
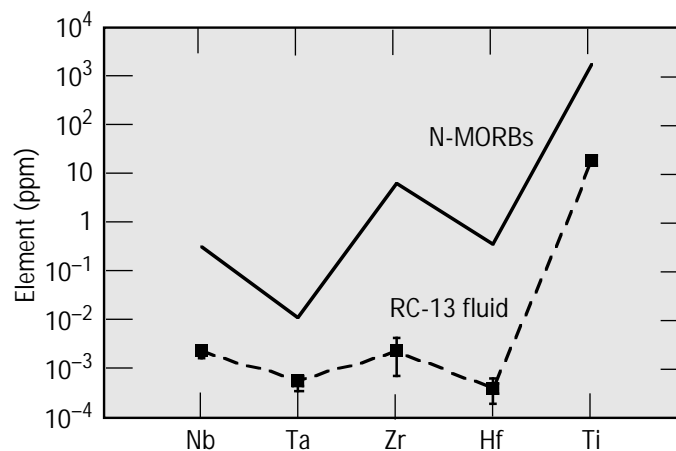


Figure 10. Summary of mineral–fluid partition for the high-field-strength elements, Ba, Pb, and Sr, all determined at 900°C and 2 GPa. Cpx = clinopyroxene; opx = orthopyroxene.

indicate that, following dehydration of the subducted lithosphere, the U/Pb ratio in basaltic crust is increased, whereas Rb/Sr is likely to be dramatically reduced. Subduction and prolonged aging of this material produce an isotopic reservoir with the characteristics of a mantle component sampled by some oceanic island basalts.

We also determined the partitioning of high-field-strength elements between rutile ( $\text{TiO}_2$ ) and aqueous fluid. Rutile is an important mineral in island-arc basalt source regions because the incorporation of high-field-strength elements (particularly Nb and Ta) in rutile has been used to explain the depletion of these elements in island-arc basalts. Previous work by our group showed that rutile could not coexist with an island-arc magma within the zone of partial melting because the  $\text{TiO}_2$  content of these magmas was too low to allow rutile stability. However, the presence of rutile in the subducted lithosphere during dehydration remained a possibility. Our new results, coupled with the compositions of rutiles found in natural eclogites, allows us to calculate the composition of the fluid derived during dehydration of the slab (Figure 11). This fluid is depleted in the high-field-strength elements relative to MORB and cannot enrich the island-arc basalt source region in these components. Conversely, the elements that are enriched in island-arc basalts (the alkalis) will not be retained in the slab. The depletion of high-field-strength elements in island-arc basalts can then be explained by increased degrees of partial melting induced by a fluid depleted in these elements.

*Figure 11.*  
Concentrations of high-field-strength elements in N-MORB and a subduction-related fluid (RC-13). The latter was calculated using our experimentally determined rutile-fluid partition coefficients and the compositions of metamorphosed oceanic gabbros from the Rocciavre Massif, Western Alps.



## Microstructure of Volatile-Rich Melts in Mantle Source Regions

We know from volcanoes and other evidence that magma formed at depth in the Earth can migrate to the surface before it solidifies. High concentrations of some trace elements in this magma, along with the water in the magma itself, also indicate that fluid can migrate long distances through solid rock. This fluid alters the composition of minerals and magma that it encounters and promotes the creation of the melt. Low-degree, volatile-rich melts may be important in mobilizing  $\text{H}_2\text{O}$ ,  $\text{CO}_2$ , and highly incompatible trace elements. Thus, they are effective agents of chemical modification in the lithospheric upper mantle. Knowledge of the grain-scale distribution of such melts in mantle rocks is key to defining the processes by which such small melt fractions may become mobile. Complementing the IGPP studies of the equilibrium distribution of trace elements, we are studying the microstructure of two-fluid systems (silicate melt and hydrous fluid) and the segregation of these fluids between lithologies. Participants in this study include Bill Minarik and James Brennan (LLNL).

Past laboratory studies of this problem focused on characterizing the textural properties of melts in olivine-rich matrices (i.e., wetting angle measurements); however, the combination of crystal faceting and multiple mineral phases suggests that inferences of melt connectivity based solely on these data may be ambiguous. Monitoring the bulk transport of melt-soluble elements provides a more accurate measure of melt connectivity, particularly at low melt fractions. New data, derived from iron-transport experiments, allow us to assess the connectivity—and hence the potential mobility—of carbonate- and water-rich melts in olivine-rich lithologies. To determine melt connectivity, we monitored the enhancement of diffusive iron loss from the constituent ferromagnesium silicates of partially molten vs melt-free dunite and lherzolite.

Textural observations of run products indicate that mineral/melt dihedral angles for both hydrous and carbonate-rich melts are low ( $<50^\circ$ ), and faceted crystal/melt contacts are common. Experiments involving hydrous melts are vapor saturated, and vapor is typically isolated from mineral contact by the preferential wetting of grains by melt (Figure 12). This implies that at low vapor and melt abundance, the pathways for iron transport are controlled by the topology of intergranular melt. We observe

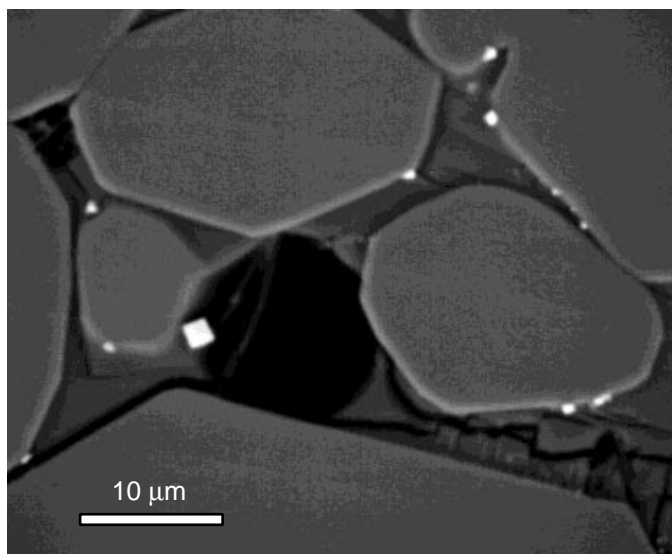


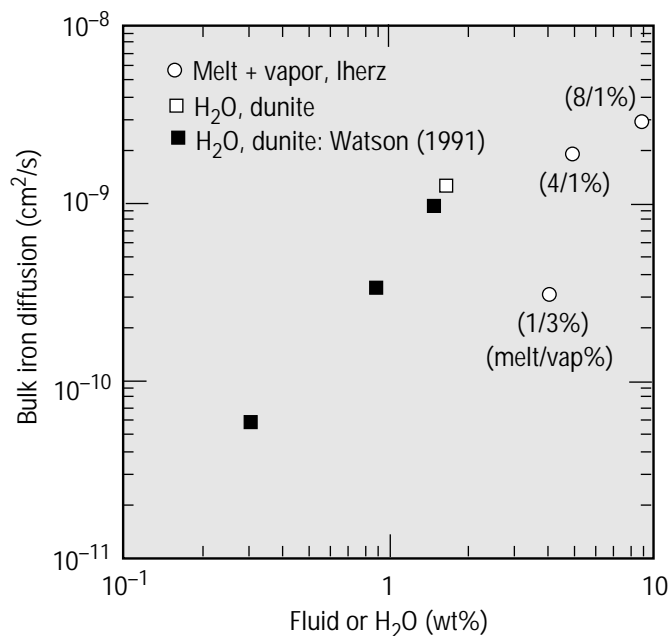
*Figure 12. A backscattered electron image of water-rich fluid pockets (dark), silicate melt quenched to glass (dark gray), and olivine crystals (light gray). The bright spots are spinel formed when the experiment was quenched from the run conditions of 1.5 GPa pressure and 1050°C temperature. Silicate melt wets the grain edges preferentially and forces the fluid into the center of the pockets. Fluid contacts olivine grains at flat faces—the low-interfacial-energy surfaces on the olivine. Because the fluid pockets are separated from each other by silicate melt, chemical transport between fluid pockets must take place through the silicate melt.*

enhancement in bulk iron diffusion from 10 to  $10^3$  times relative to melt and fluid-free samples over the entire range of melt fractions studied (1 to 8 wt% hydrous melt, 0.01 to 5 wt% carbonate melt). Our finding indicates that interconnected melts are present in all cases except at the lowest abundances of carbonate melt.

In the experiments involving carbonate melt, we also performed a series of runs to assess iron diffusivity as a function of melt fraction. These experiments indicate that the functional form of this relation is discontinuous and that at melt fractions less than 0.05 wt%, the iron diffusivity decreases rapidly. We interpret this effect as resulting from the partial closure of interconnected porosity (i.e., an increase in tortuosity), perhaps arising from the stabilization of dry grain edges in response to surface energy anisotropy. The melt fraction marking the onset of partial interconnectivity may be lower still in a mantle assemblage with a typical grain size of about 1 mm because with a larger grain size, there are volumetrically fewer grain-grain contacts. The presence of pyroxenes and other minor phases may, however, offset this effect. Diffusion through a system containing both fluid and melt is limited by the rate of diffusion through the melt, consistent with the textural observations (Figure 13).

Our results indicate that small-degree, volatile-rich melts may be interconnected in mantle rocks at melt fractions much less than 0.01 for carbonate-rich and hydrous compositions. Owing to the extreme efficiency with which highly incompatible trace elements and C–O–H fluids may dissolve in such materials, these results supply the physical basis for the process of chemical transfer and metasomatism inferred by geochemical models and petrologic observation.

*Figure 13. Bulk iron diffusion vs weight percent of added fluid (silica melt and H<sub>2</sub>O-rich fluid). The presence of melt along the grain edges slows the bulk transport of iron below that expected for H<sub>2</sub>O-rich fluid alone.*



## Textural Entrapment of Sulfide Melts: Implications for the Formation of the Earth's Core

The Earth's core comprises more than half of the planetary radius and consists mainly of iron and nickel. Other terrestrial planets, moons, and smaller bodies also have metallic cores, but the process by which these cores separate from the silicate mantles is still a matter of debate. Did the Earth's core separate by metal-silicate liquid immiscibility in a planet-scale magma ocean formed after a large accretionary impact, or did metal-sulfide melt percolate down through a solid assemblage of silicate minerals? Assembly of the Earth by the accretion of differentiated planetesimals pushes the question back one step—how did the cores of these smaller bodies separate? Constraints on the physical plausibility of the separation process are generally lacking and are needed to develop better models of the composition of the Earth's core and mantle, as well as its early thermal history.

Core separation accomplished by porous flow of Fe–Ni–S–O melt through a solid matrix has been viewed as unlikely because metal-rich melts, as a result of their high melt–solid interfacial energy, do not wet silicate grains at low pressures. Therefore, they preclude formation of an interconnected melt at low melt fraction. The melt–solid interfacial energy is minimized by a microstructure consisting of melt pockets isolated at grain corners, which thus lead to a permeability of zero. At higher pressures, increased solubility of oxygen in the metal-sulfide melt may reduce its interfacial energy against silicate minerals and may allow the metal-sulfide melt to wet grain edges and interconnect. To address this suggestion, we performed experiments at pressures up to 9 GPa to determine the microstructure of metallic melts in an olivine matrix. Participants in this project include Bill Minarik and Rick Ryerson (LLNL) and Bruce Watson (Rensselaer Polytechnical Institute).

Our results demonstrate that metal-rich sulfide melts do not wet olivine at pressures less than 9 GPa and hence do not form an interconnected grain-edge phase (Figures 14, 15). These melts cannot separate from a solid or mostly solid silicate matrix up to these pressures. This finding implies that the core material must have separated from Earth's upper mantle (at depths less than 320 km) via

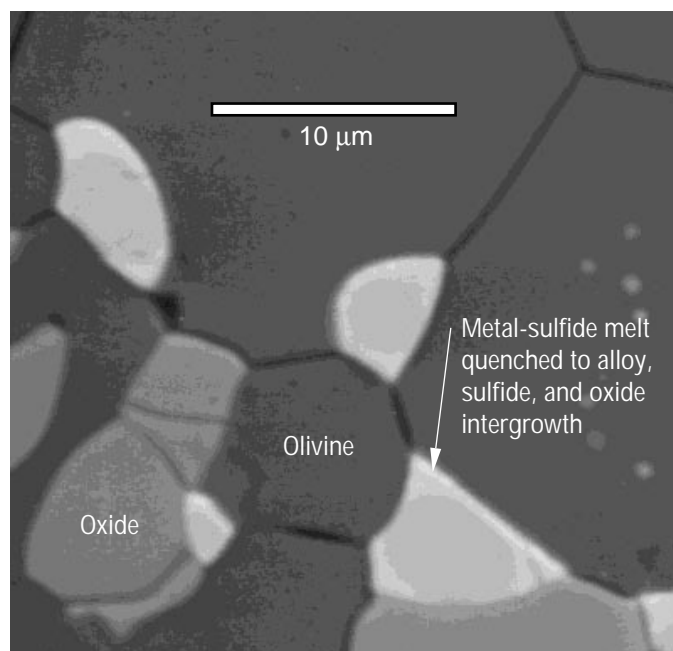


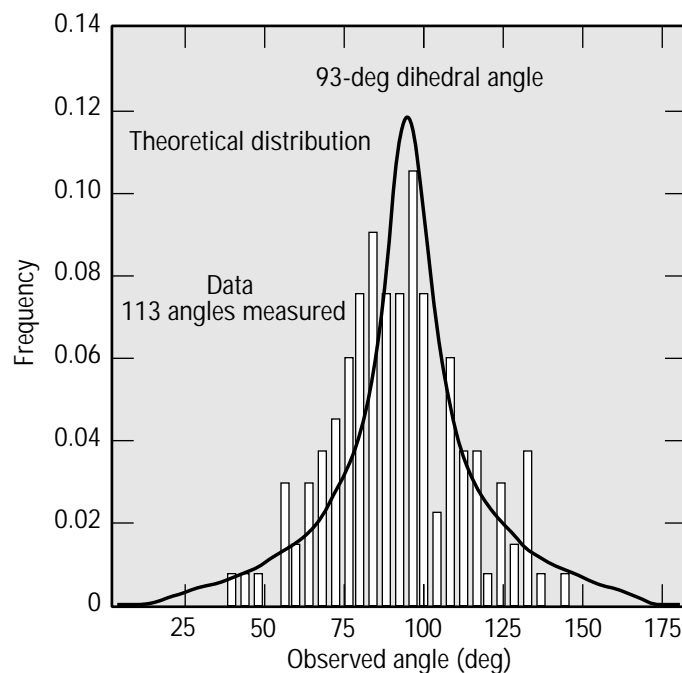
*Figure 14. A backscattered electron photo of a 9-GPa experiment showing metal-sulfide pockets at olivine grain corners, now composed of an intergrowth of metal alloy, sulfide, and oxide formed on quench. Oxide has separated on quench as a thin rim on the sulfide pockets and is also present as a stable phase. Note the generally large apparent dihedral angles between sulfide and olivine, sulfide-free grain edges, and the presence of sulfide included within the olivine grains.*

silicate-liquid/metal-sulfide liquid separation at high temperatures in a magma ocean. If the magma ocean did not encompass the entire volume of the body, it would have to be of sufficient extent to allow enough metal or metal sulfide to collect at its base as pods sufficiently massive to sink diapirically through the solid silicate below. It could not leak downward by percolating along olivine grain boundaries.

This conclusion also applies to core formation in bodies less than 2000 km in diameter (corresponding to center pressures of 9 GPa). The pressure at the center of the Earth's moon is 4.6 GPa, well within the olivine stability field; therefore, separation of a sulfur-poor metal core in the Moon (the Moon's core is estimated to be between 0 and 2% of its mass) would require extensive silicate melting.

Nonwetting metal-sulfide melts provide a physical mechanism for models of core formation that invoke incomplete separation of metal-sulfide core from silicate mantle. For example, in the inefficient core formation model, small amounts of metal sulfide could be left behind after core separation and trapped in isolated pockets at grain corners. In the late-stage veneer model, metal that accreted after core formation and the last large impact melting could also be retained in the mantle. In both cases, the metal sulfide retained in the mantle would contribute siderophile elements and produce a mantle out of chemical equilibrium with the core.

*Figure 15. Measured angles for sulfide-olivine contacts in the 9-GPa experiment along with the expected distribution for a single dihedral angle centered at the median angle of 93 deg, in excess of the pinch-off angle of 60 deg above which the melt is not interconnected. The solid-solid-melt boundaries of a sectioned experiment will show a distribution of apparent dihedral angles due to the plane of the section crossing the grain edge at a random angle. The true dihedral angle is approximated by the median angle of a large number of apparent dihedral angle measurements.*



## References

1. Tapponnier, P., G. Peltzer, A. Y. Le Dain, R. Armijo, and P. Cobbold (1982), "Propagating Extrusion Tectonics in Asia: New Insights from Simple Experiments with Plasticine," *Geology* **10**, 611–616.
2. Tapponnier, P., G. Peltzer, and R. Armijo (1986), "On the Mechanics of the Collision between India and Asia," in *Collision Tectonics*, M. P. Coward and A. C. Ries, Eds., *Geol. Soc. Am. Spec. Publ.* **19** (Geological Society of America, Washington, DC), pp. 115–157.
3. Peltzer, G., and P. Tapponnier (1988), "Formation and Evolution of Strike-Slip Faults, Rifts, and Basins during the India-Asia Collision: An Experimental Approach," *J. Geophys. Res.* **93**, 15,085–15,117.
4. Briais, A., P. Patriat, and P. Tapponnier (1993), "Updated Interpretation of Magnetic Anomalies and Seafloor Spreading Stages in the South China Sea: Implications for the Tertiary Tectonics of SE Asia," *J. Geophys. Res.* **98**, 6299–6328.
5. Lacassin, R., P. H. Leloup, and P. Tapponnier (1993), "Bounds on Strain in Large Tertiary Shear-Zones of SE Asia from Boudinage Restoration," *J. Struct. Geol.* **15**, 677–692.
6. Benjamin, T. M., W. R. Heuser, and D. S. Burnett (1980), "Actinide Crystal Liquid Partitioning for Clinopyroxene and  $\text{Ca}_3(\text{PO}_4)_2$ ," *Geochim. Cosmochim. Acta* **44**, 1251–1264.
7. Beattie, P. D. (1993), "The Generation of Uranium Series Disequilibria by Partial Melting of Spinel Peridotite: Constraints from Partitioning Studies," *Earth Planet. Sci. Lett.* **117**, 379–391.
8. LaTourrette, T. Z., and D. S. Burnett (1992), "Experimental Determination of U and Th Partitioning between Clinopyroxene and Natural and Synthetic Basaltic Liquid," *Earth Planet. Sci. Lett.* **110**, 227–244.
9. Spiegelman, M., and T. Elliot (1993), "Consequences of Melt Transport for Uranium Series Disequilibrium," *Earth Planet. Sci. Lett.* **118**, 1–20.
10. Lundstrom, C. C., H. F. Shaw, F. J. Ryerson, D. L. Phinney, et al. (1994), "Compositional Controls on the Partitioning of U, Th, Ba, Pb, Sr, and Zr between Clinopyroxene and Haplobasaltic Melts—Implications for Uranium Series Disequilibria in Basalts," *Earth Planet. Sci. Lett.* **128**(3–4), 407–423.

## Center for High-Pressure Sciences

The Center for High-Pressure Sciences makes available LLNL's high-pressure experimental, theoretical, and computational modeling capabilities for collaborations between university researchers and LLNL scientists. The collaborations include the use of experimental facilities at LLNL, joint theoretical research, use of LLNL supercomputers, and experimental work prepared at university campuses on specimens and subjected to high pressures at LLNL. University faculty, graduate students, and postdoctoral researchers participate in the program. IGPP high-pressure research encompasses geophysics, planetary physics, condensed-matter physics, chemistry, materials science, and engineering. LLNL researchers in High-Pressure Sciences are located in the Condensed-Matter Physics Division (H Division) and in Earth Sciences. The High-Pressure Sciences Center Head is William Nellis. Peter Fiske is a postdoctoral fellow.

Principal facilities and capabilities at LLNL include

- *Two-stage, light-gas guns* to measure equations of state; shock-wave profiles; electrical conductivities; and emission, Raman, and absorption spectra of minerals, liquids, and metals shocked to dynamic pressures up to 100 GPa (1 Mbar) and up to several thousand kelvins. A gas gun can also be used to synthesize new materials by applying high dynamic pressures and temperatures followed by rapid quenching.
- *Diamond anvil cells* to measure equations of state up to 100 GPa by x-ray diffraction, laser heating, and Raman spectroscopy.
- *High-pressure systems* to determine stress-strain behavior, ultrasonic velocities, permeability, phase equilibria, fracture and flow properties, diffusion kinetics, and electrical and optical properties of minerals and ceramics up to 25 GPa and 2500°C.
- *Condensed-matter theory*, including electron-band theory of bulk and layered materials, fluid perturbation and mixture theories, Monte Carlo and molecular-dynamics methods, and dense-plasma theory.
- *Computational simulations* of the response of materials to high pressures.

## Research Highlights

These various high-pressure facilities complement each other, many offer unique research opportunities, and many are in unclassified areas. Computational simulations and theories of high-pressure phenomena are strong capabilities at LLNL. Therefore, researchers from UC and other universities, industry, and LLNL programs interact with the center on issues of scientific importance.

For example, the two-stage gun achieves pressures up to 100 GPa, temperatures up to several thousand kelvins, and quench rates up to  $10^{12}$  bar/s and  $10^9$  K/s in specimens that are recovered for characterization. Quartz has been shocked in this way, and its microstructure shown to agree with that found in the Cretaceous–Tertiary boundary, the stratigraphic level at which the dinosaurs became extinct. Also, facilities at both LLNL and the National Institute of Standards and Technology (NIST) have been integrated into one project. For example, Hans-Rudolph Wenk and Kristin Bennett of UC Berkeley and William Durham of LLNL deformed ice and ice-rich specimens at LLNL's low-temperature static high-pressure facilities. The crystallographic phases and textures induced at LLNL were then characterized by neutron diffraction spectroscopy using a reactor and a low-temperature specimen holder at NIST. In the following pages, we describe the highlights of our FY 1994 research.



## Planetary Interiors

Jupiter and Saturn, the two largest planets in the solar system, have long been of considerable interest to astronomers. Jupiter and Saturn are composed primarily of hydrogen with about 10 at.% helium. The interiors are at high pressures and high temperatures because of the planets' large mass and low thermal conductivity.

For example, in Jupiter the boundary between the molecular hydrogen mantle and the metallic hydrogen core is estimated to be 300 GPa (3 Mbar) and 10,000 K at 0.77 of Jupiter's radius. Interior planetary conditions calculated from theoretical models are consistent with observed mass, radius, rotational rate, gravitational moments, and surface chemical composition. Density distributions are calculated from the gravitational moments, which are very sensitive to the equation of state at very high pressures and temperatures. Because of the high pressures and temperatures in the Jovian planets, we measured representative shock temperatures up to 5200 K at pressures up to 87 GPa. The experimental data were used to develop a theory for hydrogen. Because hydrogen is in thermal equilibrium in these shock experiments, the theory was applied to the interior of Jupiter. Participants in this project include William Nellis and Neil Holmes (LLNL) and Marvin Ross (LLNL emeritus).

## Hydrogen at Extreme Conditions

A two-stage, light-gas gun that is 20 m long was used to generate high pressures and temperatures by impacting liquid-hydrogen sample holders with metal projectiles accelerated up to 7 km/s. Figure 1 shows the temperature measurement. The measured impactor velocity together with the known compressive properties of the various materials gives the pressure and density in hydrogen. The impact generates a shock wave in the baseplate, which is transmitted into the liquid and then double shocks off the window. The first shock in the liquid is observed as a sharp rise lasting a few nanoseconds, to a steady optical emission when the shock from the baseplate breaks into the liquid. The second shock in the liquid is observed as a second sharp increase in optical intensity when the first shock reflects off the window. The emitted thermal radiation is coupled to a six-channel photomultiplier (PMT) array with fiber optics. The temperatures and emissivities of hydrogen are obtained by fitting the PMT data to a Planck spectrum.

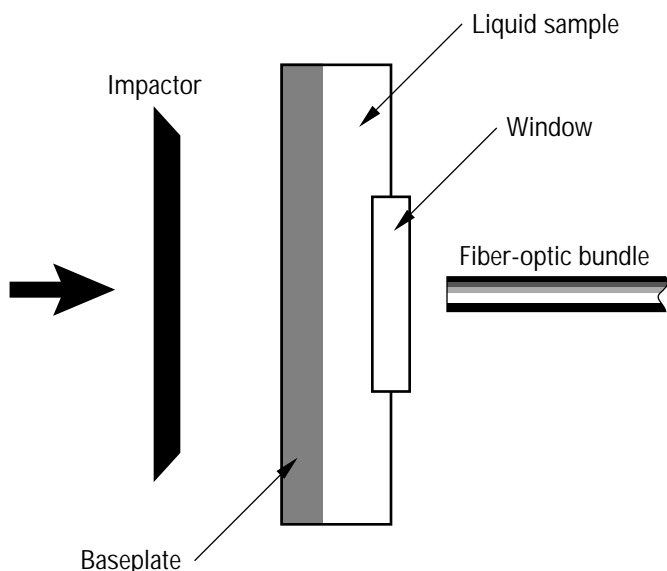


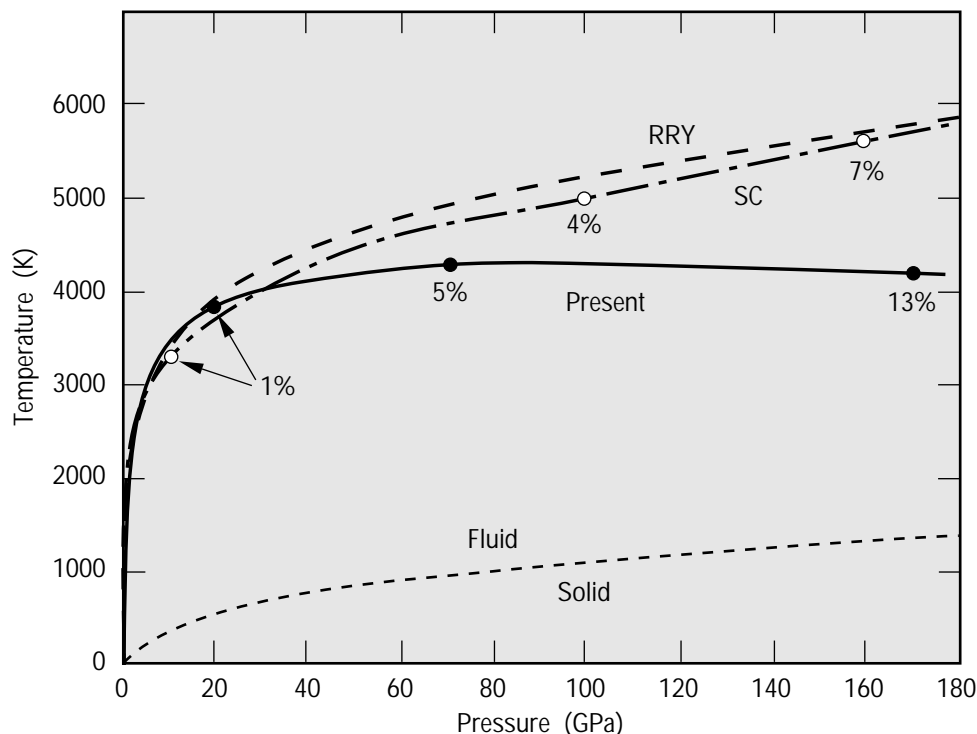
*Figure 1. Schematic of the experiments. The impactor is accelerated to velocities up to 7 km/s and generates a strong shock wave on impact with the baseplate.*

The first shock temperatures at pressures up to 22 GPa agree well with predictions that neglect dissociation. However, the second shock temperatures at highest pressures (87 GPa), densities, and temperatures are substantially lower than predicted for a purely molecular fluid. These lower temperatures are caused by partial and continuous molecular dissociation into monatomic hydrogen. The measurements were used to derive a density- and temperature-dependent dissociation energy. Our present theory was used to calculate the isentrope of hydrogen starting from 1 bar and the surface temperature of Jupiter (165 K). Figure 2 shows the isentrope plotted as temperature versus pressure, together with the previous Ross, Ree, and Young result<sup>1</sup> for pure molecular  $H_2$  and the Saumon and Chabrier result,<sup>2</sup> which includes some calculated dissociation. The present model in Figure 2 shows that the continuous dissociation of molecular hydrogen to the monatomic state keeps the isentropic temperatures relatively constant near 4000 K over a wide range of pressures (and thus depth in Jupiter) from 30 to 180 GPa. Also, temperature possibly decreases slightly at highest pressures. At 180 GPa, the present model predicts that the isentropic temperature of hydrogen is about 25% lower than previously expected, and the lower temperature is caused by the dissociation of 13% of the hydrogen molecules.

The continuous dissociative phase transition in hydrogen suggests that no sharp boundary exists between the molecular mantle and the metallic hydrogen core. That is, as molecular hydrogen dissociates continuously to the monatomic phase and eventually metallizes, there may be no sharp discontinuity in the relative composition of the molecular and metallic phases nor in density.

Because the variation of the equilibrium temperature with pressure, and thus with depth in Jupiter, is small, then it is quite possible that hydrogen convects in the molecular mantle of Jupiter. The possible existence of a maximum in temperature (Figure 2) depends on the actual details of this curve and, in Jupiter, on the presence of He and the ices. Nevertheless, a temperature maximum might actually exist in

Figure 2. Isentropes of hydrogen (calculated from 165 K and 1 bar) plotted as temperature versus pressure for our model; the Ross, Ree, and Young (RRY) result;<sup>1</sup> and the Saumon and Chabrier (SC) result.<sup>2</sup> Dissociation fractions calculated with our model and with the SC model are indicated. A calculated melting curve is also shown.



Jupiter as a function of pressure and thus of depth. As the dominant heat conduction mechanism in Jupiter, convection causes the temperature distribution to approach the isentropic one. Convection also causes magnetic fields by dynamo action. Magnetic effects are important in the molecular layer of Jupiter, and a portion of the magnetic field might be generated there. In addition, if a maximum temperature were to exist in Jupiter, then a quiescent boundary layer might be expected at depths corresponding to pressures between 30 and 180 GPa.

A boundary has been proposed in the molecular layer at 42 GPa, based on analysis of gravitational field data. At greater depths, the pressure becomes sufficient to metallize hydrogen. A further increase in depth causes the temperature to increase monotonically. Hence, there may also be a local minimum in temperature near the radius of what is now called the molecular mantle–metallic core boundary. In this case, convection would be driven toward the temperature minimum from both larger and smaller radii, causing a convectively turbulent region.

When the curves in Figure 2 are plotted as density versus pressure, their differences are much less. Thus, our new results have a weak effect on the calculated density variation with depth and a relatively weak effect on modeling the Jovian density distribution needed to match flyby data of the gravitational field.

## Impact Processes

The processes and products of meteorite impacts were studied using a combination of laboratory, theoretical, and field-oriented studies. Participants of this project include William Nellis, Peter Fiske, and Neal Hinsey. Using the 6.5-m-long, two-stage, light-gas gun to achieve velocities up to 4 km/s, we simulated hypervelocity meteorite impacts and study their effects on natural and synthetic materials. We then compared the experimental products recovered after impact to those found in nature and to those predicted theoretically.

We are continuing our research on the shock deformation of quartz using novel sample containment techniques. By containing samples in aluminum instead of steel, we have been able to better simulate the pressure history and the rapid strain rate of rock subjected to a meteorite impact. We have recovered quartz held in aluminum capsules from pressures as high as 56 GPa (560 kbars). These samples show high strain-rate effects, including the formation of diaplectic  $\text{SiO}_2$  glass, pseudotachylite-like veins of molten material, and the reduction of  $\text{SiO}_2$  to nanocrystalline Si in thin layers between grains of diaplectic glass. These thin layers experienced extremely high temperature, reduced the oxygen, and produced only Si. Because this happens so rapidly, only very fine-grained nanocrystalline Si is formed.

By comparison, it has not been possible to form amorphous fayalite,  $\text{Fe}_2\text{SiO}_4$ , by shock-compressing single crystals to 75 GPa, more than twice the pressure required to amorphize the same mineral at static high pressures in a diamond-anvil cell. Novel methods were devised to produce virtually a single shock wave in fayalite at pressures higher than those reported to induce a phase transition in polycrystalline  $\text{Fe}_2\text{SiO}_4$ . The sample was precooled to 100 K to quench any high-pressure phase that formed, but without success. It remains an unanswered question as to why high shock pressures readily cause  $\text{SiO}_2$  to amorphize but not  $\text{Fe}_2\text{SiO}_4$ . This work was done with Raymond Jeanloz and Abby Kavner of UC Berkeley.

Our work also continues on the shock effects in zircon ( $\text{ZrSiO}_4$ ). Zircon is a ubiquitous trace mineral in most rocks and is used for radiometric age dating of meteorite impacts. Zircon is unusual because it undergoes a first-order crystalline-to-crystalline phase transition to the scheelite structure both under shock compression and in a diamond-anvil cell at room temperature. This high-pressure phase is

extremely resistant to reverting back to the initial equilibrium phase and may survive in impact craters around the world. In FY 1994, we calibrated the pressure range of the zircon-to-scheelite structural phase transition and measured the kinetics of thermal reversion of the scheelite phase at 1 bar. Together, these data will be used to calibrate a shock geobarometer.

Finally, we have carried out large-scale hypervelocity impact experiments into dry quartz sand using the Super-High-Altitude Research Project (SHARP) gas-gun facility. We collaborated, by providing the target, on a project to develop a scramjet engine for hypervelocity jet engine technology. In this experiment, a 4.6-kg scramjet engine traveling at 3.0 km/s impacted into quartz sand at an angle of 20 deg.

This test allowed us to study oblique hypervelocity impacts with a kinetic energy 3 orders of magnitude higher than that used in previous laboratory studies.

Thermocouples buried in and around the point of impact recorded temperatures in the ejecta as high as 150°C. Post-impact excavation of the target area exposed isolated fragments of shock-consolidated sand overlying shock-comminuted sand that graded into pristine sand. The fine-grained distal ejecta, analyzed by x-ray diffraction, consisted of quartz with a trace of Al, the principal constituent of the jet engine. These data provide a means of directly measuring the partitioning of energy during hypervelocity impact into unconsolidated materials. Future experiments at the SHARP facility would provide a unique opportunity to conduct large-scale hypervelocity impact experiments.

Other ongoing projects include a study of the field occurrence and preservation of tektites and a study of the shock compaction of diamond powders and the formation of carbonados, which are naturally occurring polycrystalline diamonds.

---

## References

1. Ross, M., F. H. Ree, and D. A. Young (1983), *J. Chem. Phys.* **79**, 1487.
2. Saumon, D., and G. Chabrier (1991), *Phys. Rev. A* **44**, 5122.

## *Astrophysics Research Center*

The Astrophysics Research Center serves the aims of the IGPP–LLNL in the area of astrophysics. This includes managing the astrophysics part of the UCRP and facilitating contacts between UC scientists and their LLNL counterparts. The Astrophysics Research Center also serves as the focus of astrophysics activities at LLNL by organizing the weekly astrophysics colloquium, by hosting visitors and collaborators, by editing an annual Observatory Report that covers all astrophysics activities at LLNL (and is published in the *Bulletin of the American Astronomical Society*), and providing a variety of other service functions. The staff and postdoctoral researchers of the Astrophysics Research Center carry out a significant program of research.

The scientific staff of the center are Charles Alcock (Center Head), Kem Cook, Claire Max, and Willem van Breugel. Administrative support is provided by Christina Budwine (Operations Manager), and by secretaries Arlene Manning and JoAnne McGuire. Alan Edwards manages the network of computers in the center. He has been assisted by Deanne Proctor, who supported the astronomical image processing codes AIPS and IRAF, and by Susan Peterson, who has taken responsibility for daily maintenance and for acquisitions.

Much of the research in the Astrophysics Research Center is carried out by the postdoctoral fellows, who have proved to be an energetic and stimulating group. Some fellows are supported entirely by IGPP funds, while some are supported partially by other groups at LLNL. In FY 1994, the postdoctoral fellows were David Bennett (previously at Princeton University), Leigh Brookshaw (Yale University), Susana Deustua (University of Michigan), Michael Gregg (Australian National University), George Hawkins (UC Los Angeles), Suzanne Hawley (Observatories of the Carnegie Institute of Washington), Karsten Jedamzik (UC San Diego), Scott Olivier (UC Santa Cruz), Robert Rogers (Harvard University), and Christopher Skinner (University of Manchester). Suzanne Hawley came with a Hubble Fellowship. In addition to the IGPP postdoctoral fellows, Maurice Aufderheide and Ted Ressel, who are postdoctoral fellows in the Physics Department, sit in the Astrophysics Research Center, participate in all the activities, and contribute to the intellectual vitality of the group.

The center hosts a large number of scientific visitors, not only from the UC campuses but also from around the United States and the world. These visitors stay for lengths of time ranging from a day to a year. Some who are affiliated with more local institutions spend large, ongoing portions of their time in the center. A prominent example is Robert Becker of UC Davis, who spends two or three days a week at the center and contributes significantly to the scientific program.

The center and its offices are housed in Building 319, which is close to the offices of many LLNL astrophysicists and is subject to minimal access controls. These features make the center ideal for the many collaborations that have developed between UC researchers and LLNL scientists.

The Astrophysics Research Center has access to a variety of machines for computing. Most day-to-day work, which includes code development, image processing, and symbolic manipulation, is carried out on the center's network of Sun workstations. This network comprises three server machines, twelve Sparcstations, and a few low-end workstations. One of the servers is on loan from UC Davis and is primarily used by Robert Becker for processing radio astronomy data. This network has increasingly been used for large-scale processing by the exploitation of codes that utilize a large fraction of the network for parallel processing; this is especially effective at night, when most of the network is otherwise quiet, and when the "invasive"

code will not adversely impact the image processing work. In addition, much greater computing power is available in other parts of LLNL: There is an eight-processor Solbourne and a network of fourteen IBM Risc stations in the Physics Department, and there are the Cray supercomputers in the LLNL Open Computing Facility and in the National Energy Research Supercomputer Center.

## **Research Highlights**

The Astrophysics Research Center has developed a research program that exploits the traditional strengths in astrophysics at LLNL, and in addition opens up new areas not previously represented at the Laboratory. This research ranges from smaller-scale theoretical and observational projects carried out by the staff and post-doctoral fellows to large collaborative ventures that involve scientists from outside IGPP. The following pages give a summary of some of this research.

### **Laser Guide Stars**

Claire Max, Clifford Choccol, and Herbert Friedman, plus four other LLNL collaborators and five collaborators from three UC campuses, are developing laser guide stars for astronomical adaptive optics. The goal of this project is to improve the angular resolution achieved at ground-based observatories. If the project is successful, the angular resolution at major observatories might be improved by factors of 10 to 100.

The angular resolution of all ground-based telescopes with apertures larger than 10 to 20 cm is limited to about a second of arc because of turbulence in the atmosphere. In principle, one can use adaptive optics to correct for the wavefront distortions, which are measured with a wavefront sensor, by deforming a flexible secondary mirror to make the wavefront nearly flat. This correction would allow ground-based telescopes to be operated at or near their diffraction limits. For example, at a wavelength of 0.5  $\mu\text{m}$ , the diffraction-limited resolution would be 0.04 arcsec for a 3-m telescope (such as that at UC's Lick Observatory) and 0.01 arcsec for a 10-m telescope (such as the new Keck Telescope). These represent improvements in resolution of factors of 25 and 100, respectively, relative to the atmospheric resolution of about 1 arcsec.

To accomplish this correction in the visible range, however, one needs a bright reference object within a few arcseconds of the object being imaged. The statistics of bright stars are such that, at most, a few percent of the sky is accessible for diffraction-limited viewing, using nearby bright stars as the wavefront reference.

To make up for the lack of bright reference stars, this consortium is developing the ability to produce artificial stars using a powerful laser. Specifically, the idea is to use a laser tuned to the sodium D lines to resonantly excite the atmospheric sodium layer at 90-km altitude, making an artificial star to serve as a reference beacon. A wavefront sensor then detects the tilts of the reference wavefront, and a wavefront computer uses the reference wavefront to calculate the necessary adaptive-optics corrections. Finally, the correction is applied to a deformable mirror. The images recorded using the deformable mirror, together with the telescope's primary mirror, will then have most of the atmospheric distortions removed.

During the first phase of this long-term project, the team created artificial stars using one of the powerful lasers at LLNL. Specifically, the copper-vapor-pumped dye laser developed for LLNL's Atomic Vapor Laser Isotope Separation (AVLIS) program was used to create an artificial star by illuminating the atmospheric sodium layer at 90 km. The guide star is fifth magnitude when the laser power is 1100 W,

and will be brighter once an optical pulse stretcher is brought into operation. The guide-star brightness as a function of laser power and central frequency has been measured, and preliminary wavefront sensor measurements have been performed using a wavefront sensor with 8-cm subapertures on a half-meter telescope.

LLNL's AVLIS program developed a high-repetition-rate laser that is compact in footprint and easily transportable to a remote site, where it can be reassembled and perform reliably and reasonably efficiently. Simultaneously, this group has performed preliminary adaptive optics corrections on the 1-m telescope at UC's Lick Observatory. This adaptive optics system will be combined with the new laser and then operated as a laser-guide-star adaptive optics system at the 3-m telescope at Lick Observatory. The long-term goal is to establish a laser guide star system on the UC-Cal Tech Keck telescope at Mauna Kea, Hawaii.

## **The MACHO Project**

The MACHO project is an experimental search for the dark matter, which makes up at least 90% of the mass of our galaxy. It was initiated at LLNL and now involves scientists from five institutions: Charles Alcock, Robyn Allsman, Timothy Axelrod, David Bennett, Kem Cook, and Hye-Sook Park at LLNL; Stuart Marshall and Christopher Stubbs of the Center for Particle Astrophysics at UC Santa Barbara; Kim Griest of the Center for Particle Astrophysics at UC San Diego; Saul Perlmutter and Will Sutherland of the Center for Particle Astrophysics at UC Berkeley; and Kenneth Freeman, Bruce Peterson, Peter Quinn, and Alex Rodgers of the Mount Stromlo and Siding Spring Observatories in Australia.

Dark matter is known to exist and to be distributed in a large, spherical halo. However, the constitution of this matter is unknown because it emits no detectable radiation. Most hypotheses for the constitution of this matter involve speculations drawn from particle physics. The experiment will search for planets, brown dwarfs, and black holes (or any other massive objects, which are now collectively called MACHOs, for massive compact halo objects) in the mass range  $10^{-7} M_{\odot} < M < 1 M_{\odot}$ . These objects represent the conservative hypothesis for the constitution of the dark matter.

If the dark matter is made of MACHOs, they will occasionally magnify the light from extragalactic stars by the gravitational lens effect. The magnification can be large (up to factors of many). An event can be recognized by fitting a theoretical light curve to the observations (three-parameter fit) and by the lack of color variation in the event (it is achromatic). Unambiguous recognition by microlensing thus requires that there be adequate numbers of data points on the light curve (10) and measurements in at least two filter bands. The expected event rate, however, is low. It is necessary to monitor millions of stars for several years to detect tens of events. The original design goal was to detect at least 10 "good" events (maxima greater than 0.25 magnitudes, more than 10 points a light curve, good three-parameter fit, no color variation) per year of operation, if MACHOs make up the halo. The experiment will operate for a minimum of four years.

The MACHO project is operating with the 130-cm reflecting telescope of the Mount Stromlo Observatory, near Canberra, Australia. Operating at prime focus with an innovative optical system gives a field of view 1 deg in diameter, and the use of a dichroic filter allows simultaneous imaging in two spectral bands, doubling the effective exposure rate. The beams leaving the beam-splitter are imaged onto mosaics of four  $2048 \times 2048$ -pixel charge-coupled devices (CCDs), where  $15 \text{ m} = 0.6\text{-arcsec}$  pixels. The typical exposure is 300 s, followed by  $\sim 60$  s to read out the CCD chips. The data rate from this experiment is large, with an average rate of

4 Gbytes per night. The data are processed at the telescope using a dedicated computer system and software developed for the project. This system can measure the brightnesses of several million stars, twice per night, in the Large Magellanic Cloud. Working in the crowded regions at the central bar in the Large Magellanic Cloud, it is possible to record more than 500,000 stars in one image. In the even more crowded regions near the center of the Milky Way, it is possible to record more than 600,000 stars in one image.

The system had some spectacular successes in FY 1994, including the first detection of gravitational microlensing (Figure 1), which was made simultaneously with a French group, and the later discovery of an unexpectedly high gravitational microlensing event rate toward the center of the Milky Way. These results are extremely exciting, but preliminary. The next few years of observation and analysis will disclose what is really happening in this field.

With the system described above, the MACHO group expects to answer definitively whether the dark matter in our galaxy is made up of objects with mass in the range of  $10^{-7} M_{\odot} < M < 1 M_{\odot}$ .

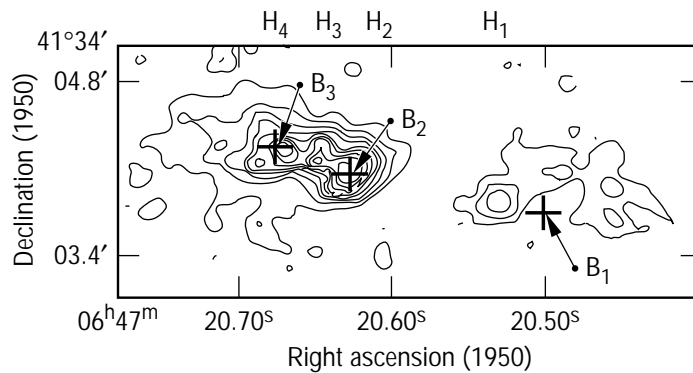


*Figure 1. A linear contour representation of a deconvolved image from the Hubble Space Telescope showing the most distant galaxy, 4C 41.17 at a redshift  $z = 3.80$  (Ref. 1). The positions of the radio components  $B_1$ ,  $B_2$ , and  $B_3$  are marked by crosses. Compact optical components denoted by  $H_1$ ,  $H_2$ ,  $H_3$ , and  $H_4$  are also indicated. Note that there is an uncertainty of a few tenths of an arc-second between the radio and optical components.*



---

## **Active Galaxies at High Redshift**

Active nuclei—whether their energy source is a supermassive black hole accreting matter (as is thought to be the case for quasars, radio galaxies, and Seyfert galaxies) or massive stars (as in the case of starburst galaxies)—can have a great impact on their galactic surroundings through their prodigious output of luminous and mechanical energy. Moreover, since the process of galaxy formation is thought to be accompanied by high rates of star formation, active galaxies (such as starburst galaxies, which are forming stars at nearly the predicted rates that occurred during galaxy formation) might be the most suitable analogs of forming galaxies in the local universe. Therefore, by studying starburst galaxies specifically and active galaxies in general, one might be able to elucidate the important physical processes that shaped galaxies during their formation and subsequently drove their evolution.

IGPP–LLNL has a small but active group studying galaxies exhibiting a wide range of nuclear activity. Two of the most important studies are focusing on investigating the most distant and powerful active galaxies in the universe—high redshift quasars and radio galaxies, which are being observed when the universe was only about 10% of its current age—and studying the energetic outflows of starburst galaxies, which may have important implications for our understanding of the main physical processes that drive galaxy evolution.

In collaboration with astronomers at other institutions, we found that the most distant quasars and radio galaxies are located in some of the most luminous galaxies known (about 100 times more luminous than a typical galaxy such as our Milky Way), and that these galaxies have very complex, often multimodal morphologies. Our results suggest that these distant galaxies may be at a much earlier phase of evolution when galaxies were conglomerating for smaller subgalactic pieces. Interactions between the merging pieces are thus bringing gas into the centers of the galaxies that then energize their active nuclei.

We are also studying energetic galactic-scale outflows from starburst galaxies (called superwinds). These outflows result when the kinetic energy of overlapping supernova explosions within the starburst region is effectively thermalized to form a hot ( $\sim 10^7$ - to  $10^8$ -K) cavity of gas. This hot thermal plasma has a pressure much higher than the ambient pressure within a galaxy and, thus, flows out of the galaxy. We found that starburst galaxies exhibit evidence for these outflows and that such outflows can propel a large fraction of the interstellar medium (the pervasive gas that lies between the stars within a galaxy) of the starburst galaxy out of the galaxy. Such winds may be a mechanism whereby galaxies can expel metals and globally rearrange their interstellar media. Superwinds may, therefore, have had a tremendous effect on determining the structure we see in galaxies today.

## Searching for Asteroids

Kem Cook and Charles Alcock, working with Eugene Shoemaker (U.S. Geological Survey) and Ted Bowell (Lowell Observatory), are developing a new CCD camera to use for a preliminary search for near-Earth asteroids. The camera is similar to the cameras developed for the MACHO project, but it has been modified for use in scan mode. With scan mode, the camera/telescope system is moved rapidly along great circles across the sky, and the CCD chips are read out constantly. This mode is an effective way to cover very large regions of sky with short exposures, which is needed for this project. The camera will be installed on the 24-in. Schmidt telescope at Anderson Mesa, Arizona, and is expected to go into operation in FY 1995. This system is expected to greatly enhance the present discovery rate for near-Earth asteroids. It will also serve as a development stage for the much more ambitious Spaceguard project, which aims to detect more than 90% of all large (>1-km) near-Earth asteroids.

---

## References

1. Miley, G. K., K. C. Chambers, W. J. M. van Breugel, and D. Macchetto (1992), "HST Imaging of Distant Galaxies: 4C 41.17 at  $z = 3.8$ ," *Astrophys. J.* **401**, L69.

---

## Section III. Research Summaries of Collaborative Projects

### *Geosciences*

---

#### **A Global Survey for the 80-km Discontinuity Using Three-Component Broadband Data**

**Principal Investigator:** Peter Shearer (UC San Diego)

**LLNL Collaborators:** George Zandt and William R. Walter

**Student:** Paul Earle (UC San Diego)

---

#### **Abstract**

*In 1969, Anton Hales inferred the existence of an 80-km discontinuity south of Lake Superior from an observed change of apparent velocity in two long refraction lines. Several recent studies using various methods support the presence of an 80-km (Hales) discontinuity in some areas.<sup>1-3</sup> However, the Hales discontinuity is not a universally accepted feature and is absent from both the PREM and IASP91 velocity models. Reported depths to the Hales discontinuity differ. For example, Revenaugh and Jordan<sup>4</sup> observe regional variations in its depth from 43 to 89 km. Possible origins for the Hales discontinuity include strain-induced anisotropy or a phase change in the spinel to garnet facies. Our research involves a search for the global characteristics of the Hales discontinuity by focusing on the S-to-P converted phase  $SP_dP$ . Previous observations of strong  $SP_dP$  phases recorded on broadband seismic stations in North America<sup>1</sup> appear to require a Hales discontinuity. We plan to expand on this work by examining all available broadband global seismic records and modeling any observed  $SP_dP$  phases with synthetic seismograms.*

---

#### **Objectives**

Our objective is to constrain the global extent and properties (depth and impedance contrast) of the Hales discontinuity from observations of S-to-P converted phases and place upper bounds on its magnitude in regions that produce no observable reflections. We hope to examine enough data so that stacking techniques will prove useful in improving the signal-to-noise ratio of the seismograms, increasing the number of  $SP_dP$  observations. By conducting forward modeling using reflectivity synthetic seismograms, we plan to discriminate between 80-km discontinuity phases and Moho reflections. An improved knowledge of the seismological properties and global extent of the 80-km discontinuity would provide insight into its origin.

---

#### **Progress**

A search of more than 15,000 global broadband records, obtained from the IRIS Data Management Center, has produced observations of possible  $SP_nP$  arrivals (topside reflections from the Hales discontinuity) at 22 stations. Figure 1 shows an example observation. The  $SP_nP$  phase travels through the mantle as an S wave and is converted at the surface to a P wave, which undergoes a topside reflection from the Hales discontinuity (Figure 1a). Under some circumstances, the amplitude of this phase can be comparable to S (Figure 1c) but with a distinctly different particle motion.

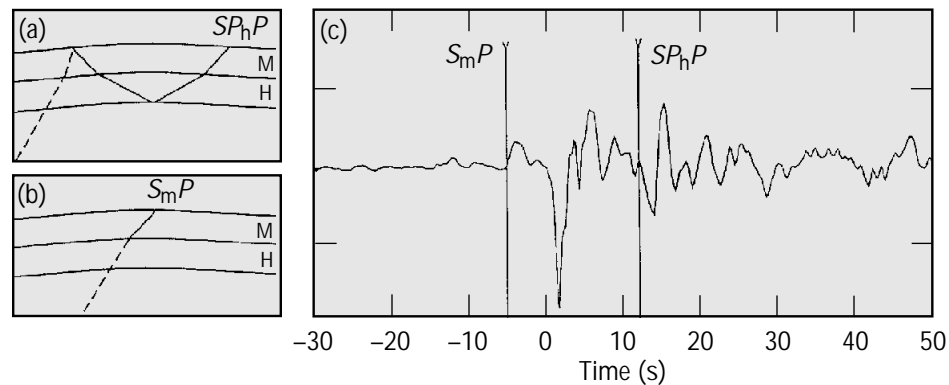


Figure 1. Raypath for (a)  $SP_hP$  (the  $SP_hP$  phase resulting from the topside reflection from the Hales discontinuity), and (b) the S-to-P conversion from the Moho ( $S_mP$ ). Dashed lines = S waves; solid lines = P waves; M = the Moho reflection; and H = the Hales discontinuity. (c) Radial-component broadband seismogram from ARU (Arti, Russian Federation). Arrival times for S-to-P converted phases are shown as vertical lines. Arrival times are calculated for a 35-km Moho and a 70-km Hales discontinuity. The S-wave arrival is aligned at zero time and was picked from the transverse component record. The large-amplitude  $SP_hP$  results from a postcritical reflection from the Hales discontinuity. The  $SP_mP$  arrival (topside reflection from the Moho) is not observed because it is obscured by the S coda. As a result of its precritical reflection, it is small in amplitude at this range.

The observations are concentrated in areas of continental shields including North America, Australia, and Asia. Some care is needed to distinguish between  $SP_hP$  arrivals and phases resulting from topside Moho reflections ( $SP_mP$ ). Thus, we are analyzing synthetic seismograms to model the effects of a Hales discontinuity. Reflectivity synthetics suggest that the observed anomalies occur at longer ranges than should be expected from  $SP_mP$  alone, implying the existence of a deeper discontinuity. However, further study is needed to increase confidence in this conclusion. In FY 1994, we reviewed the data and discussed ways to make the reflectivity calculations faster, thus allowing a more efficient search of model space.

The application of stacking techniques to improve the signal-to-noise ratio of the seismogram has so far been unsuccessful. This problem may be caused by regional variations in depths to the discontinuity. Reflections from different depths arrive at different times, resulting in incoherent stacks. One solution is to stack records from single stations. Unfortunately, topside reflections from the Hales discontinuity occur for a small range of ray parameters, limiting the number of single station records. The ongoing expansion of our database should lessen this problem. In FY 1995, we will experiment with developing a more robust stacking technique that emphasizes the difference in polarization of the S and the  $SP_hP$  arrivals.

## References

1. Zandt, J., and G. E. Randall (1985), *Geophys. Res. Lett.* **12**(9), 565–568.
2. Zhang, Z., and T. Lay (1993), *J. Geophys. Res.* **98**, 4389–4405.
3. Benz, H. M., and J. McCarthy (1994), *Geophys. Res. Lett.* **21**(7), 509–512.
4. Revenaugh, J., and T. H. Jordan (1991), *J. Geophys. Res.* **80**, 19781–19810.

# Shear-Wave Velocity Structure beneath Central California from Surface-Wave Dispersion

**Principal Investigator:** Jiajun Zhang (UC Santa Cruz)

**LLNL Collaborator:** William R. Walter

## Abstract

*We used a new method to measure the incident-azimuth anomalies of surface waves recorded at several broadband stations in California from six large, shallow earthquakes that have occurred since 1988. This method is based on analyzing polarization state vectors, which are calculated analytically from three-component seismograms. The earthquakes were located within an arc distance of 90 deg from the stations and lie either on the great-circle path connecting stations MHC and PAS or on another path connecting stations CMB and GSC. The first path (MHC-PAS) is near the San Andreas Fault System (SAFS), and the second (CMB-GSC) traverses the Sierra Nevada Batholith and the Basin and Range, parallel and to the east of SAFS. We observed strong incident-azimuth anomalies for Rayleigh waves with periods between 20 and 150 s. Anomalies were as large as 35 deg for a period of 30 s and 20 deg for a period of 150 s; however, the largest anomaly for Love waves with periods between 30 and 150 s is only 20 deg.*

## Objectives

Our goal was to use broadband surface-wave dispersion analysis to study earth structure and anisotropy in California, specifically to improve our understanding of processes associated with the evolution of the Pacific–North American plate boundary. Surface-wave velocities strongly correlate with the age of the oceanic lithosphere and asthenosphere with velocities for a young ocean being significantly reduced. The methods currently used in surface-wave dispersion analysis are applicable to regions with smooth velocity variations, but they are inadequate for regions encompassing strong lateral heterogeneities. The crust and upper mantle beneath California is highly heterogeneous, since it encompasses the active SAFS. Our objective is to develop new techniques for analyzing dispersion characteristics of waves propagating in laterally heterogeneous media. These techniques include a polarization analysis method and a high-resolution, two-station method of dispersion analysis.

## Progress

We analyzed a data set of broadband seismograms from six large, shallow earthquakes that have occurred since 1988 in the North Pacific Ocean and in South America. The seismograms were recorded by several broadband stations in California, including stations MHC (Mount Hamilton), PAS (Pasadena), CMB (Columbia College), and GSC (Goldston). These earthquakes lie either on the great-circle path connecting stations MHC and PAS or on the great-circle path connecting stations CMB and GSC. The events on the MHC-PAS path include the South of Alaska earthquake (on September 4, 1989, with a magnitude,  $M_s = 6.9$ ), the earthquake near the north coast of Chile (August 14, 1988,  $M_s = 6.5$ ), and the Northern Peru earthquake (April 5, 1991,  $M_s = 6.8$ ). The events on the CMB-GSC path include two earthquakes in the Komandorsky Islands region (on February 29, 1988,  $M_s = 6.8$  and on November 6, 1990,  $M_s = 7.0$ ) and the one near the east coast of Kamchatka (on March 2, 1992,  $M_s = 6.8$ ). These earthquakes were located in the northwest or southeast within an arc distance of 90 deg from the stations. The differences between backazimuths for these events at each station is less than 5 deg.

We determined incident-azimuth anomalies of Rayleigh and Love waves as a function of instantaneous periods using the method of pure-state polarization analysis, which is based on state vectors of three-component seismograms.<sup>1</sup> We corrected for the effects of possible mode contaminations on measured azimuth anomalies using synthetic seismograms computed for the laterally homogeneous earth model PREM following the procedure of Gilbert and Dziewonski.<sup>2</sup> For both Rayleigh and Love waves with periods between 20 and 150 s, the errors for the measured azimuth anomalies corrected for mode contaminations are in general less than 10 deg.

Figure 1a shows the incident-azimuth anomalies of Rayleigh and Love waves for the 1989 South of Alaska earthquake, which lies on the MHC-PAS great-circle path and was located in the northwest at arc distances of 29.9 deg from MHC, 30.0 deg from CMB, and 34.1 deg from PAS. Figure 1a indicates that: (1) Rayleigh wave anomalies show stronger station dependence than Love wave anomalies; (2) for periods between 60 and 100 s, Rayleigh wave anomalies are smaller than 5 deg for stations CMB and MHC but range between 10 and 20 deg for station PAS; and (3) for Rayleigh waves with a period of 20 s, the anomaly is about 15 deg at MHC and 25 deg at PAS. Therefore, we conclude that Rayleigh waves are strongly affected by low-velocity anomalies associated with the SAFS beneath central California with raypaths bending eastward as waves travel to the south. Love waves suffer much less, adding observables to constrain the depth extent of the anomalies.

Figure 1b shows the incident-azimuth anomalies of Rayleigh and Love waves for the 1992 East of Kamchatka earthquake, which lies on the CMB-GSC great-circle path and was located in the northwest at arc distances of 24.8 deg from the 1989 South of Alaska earthquake and 54.8 deg from CMB, 58.8 deg from GSC, and 58.9 deg from PAS. This figure indicates that: (1) for periods between 80 and 150 s, anomalies for both Rayleigh and Love waves are larger than 15 deg for station CMB but smaller than 10 deg for stations PAS and GSC; and (2) there is strong station dependence of incident-azimuth anomalies for both Rayleigh and Love waves with periods shorter than 80 s. The station dependence of incident-azimuth anomalies is also observed for other earthquakes used in this study, with the dependence becoming stronger for earthquakes in longer distances from stations.

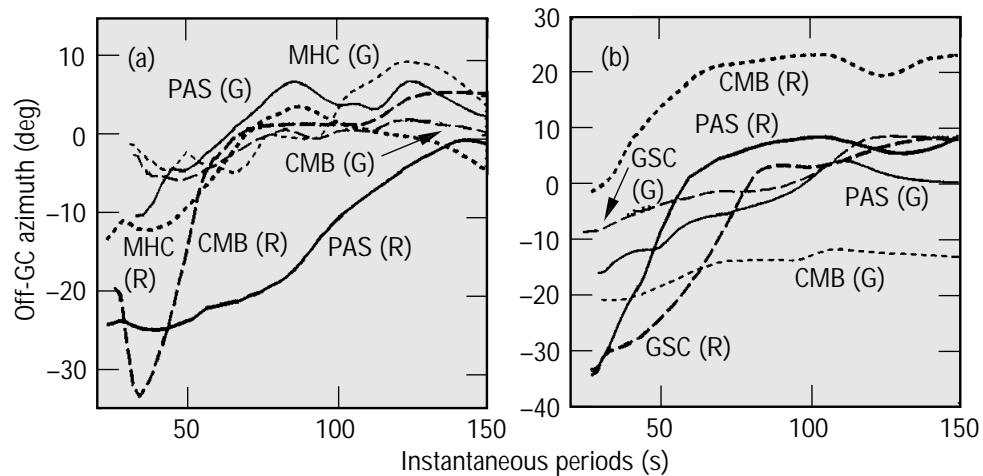
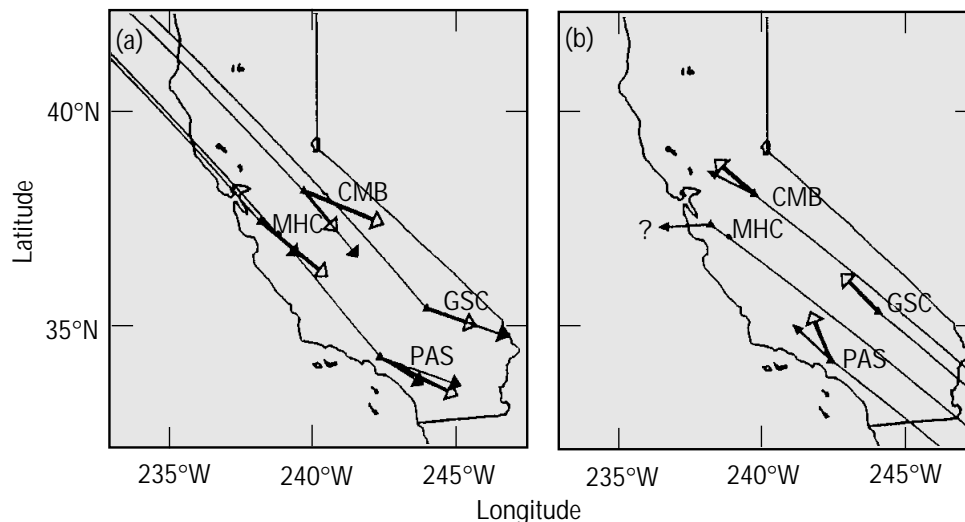


Figure 1. Incident-azimuth anomalies vs instantaneous periods for Rayleigh (thick lines) and Love (thin lines) waves recorded at several broadband stations in California from (a) the South of Alaska earthquake on September 4, 1989, and (b) the earthquake east of Kamchatka on March 2, 1992. Azimuth anomalies are measured from the great circle (GC) between source and station using polarization state vectors of ground displacements.

Figures 2a and b illustrate the incident directions for Rayleigh waves with a period of 30 s for various events used in this study. The azimuth of an arrow relative to the great circle that is shown for each station indicates the observed azimuth anomaly. Figure 2a indicates that for the earthquakes in the northwest, Rayleigh waves arrive at each station with raypaths bending eastward, and that incident-azimuth anomalies become larger as waves travel to the south from stations MHC and CMB to stations PAS and GSC. However, Figure 2b shows that for the earthquakes in the southeast, the wave arrival directions are more complex than those shown in Figure 2a. Improved understanding of the polarization characteristics of waves that arrive from the southeast direction should await further investigation using a larger data set.



**Figure 2.** Directions of arrivals for Rayleigh waves with a period of 30 s. (a) Directions of arrivals for the earthquakes located in the northwest, which include the 1988 Komandorsky Islands earthquake (distance to PAS,  $\Delta_{PAS} = 54$  deg, short solid arrows), the 1989 South of Alaska earthquake ( $\Delta_{PAS} = 34$  deg, long open arrows), the 1990 Komandorsky Islands earthquake ( $\Delta_{PAS} = 53$  deg, short open arrows), and the 1992 Kamchatka earthquake ( $\Delta_{PAS} = 59$  deg, long solid arrows). The solid lines indicate great-circle paths for the South of Alaska earthquake. The azimuth of an arrow relative to the solid line for each station indicates observed incident-azimuth anomaly. (b) Directions of arrivals for the earthquakes located in the southeast, which include the 1988 Chile earthquake ( $\Delta_{PAS} = 76$  deg, short solid arrows) and the 1991 Peru earthquake ( $\Delta_{PAS} = 56$  deg, short open arrows). The solid lines indicate great-circle paths for the Peru earthquake.

1. Samson, J. C. (1983), "Pure States, Polarized Waves, and Principal Components in the Spectra of Multiple, Geophysical Time-Series," *Geophys. J. R. Astron. Soc.* **72**, 647.
2. Gilbert, F., and A. M. Dziewonski (1975), "An Application of Normal Mode Theory to the Retrieval of Structure Parameters and Source Mechanisms from Seismic Spectra," *Philos. Trans. R. Soc. London, Ser. A* **278**, 187.

## References

## Investigation of the April 25, 1992, Cape Mendocino Aftershock Sequence

**Principal Investigator:** Susan Y. Schwartz (UC Santa Cruz)

**LLNL Collaborators:** George Zandt and Stanley Ruppert

---

### Abstract

*Source parameters of aftershocks from the magnitude 7.1 Cape Mendocino, California, earthquake on April 25, 1992, were determined from a grid search inversion of P, SH, and SV amplitude ratios recorded by a local network of three-component broadband stations jointly deployed by IRIS and IGPP–LLNL. The 1992 Cape Mendocino earthquake occurred at the intersection of the North American, Gorda, and Pacific plates. Although the mainshock was associated with underthrusting of the Gorda Plate beneath the North American Plate, fault plane solutions for 70% of the 38 largest aftershocks indicate that these events result from motion between the Gorda and Pacific plates. At the terminus of the buttressing, rigid Pacific Plate, the Gorda Plate responds to regional north–south compression by subducting beneath the Pacific Plate rather than by internal deformation, which is predominant to the northwest. At greater depth, all aftershocks have right-lateral strike-slip mechanisms with one nodal plane parallel to their northwest–southeast trend. These events define the extension of the Mendocino Fault as it approaches the Mendocino Triple Junction.*

---

### Objectives

Our goal in this study was to determine source parameters of aftershocks from the 1992 Cape Mendocino, California, earthquake and use this information to help elucidate faulting geometries in the complex region near the Cape Mendocino Triple Junction.

---

### Progress

Source parameters of 38 aftershocks from the magnitude  $M_w = 7.1$  Cape Mendocino, California, earthquake were determined using a grid search inversion of P, SH, and SV amplitude ratios recorded by a temporary local network of broadband stations. The inversion procedure consists of: computing synthetic seismograms for three fundamental fault orientations for all source receiver pairs over a range of source depths; calculating the complex envelopes of the seismograms to determine peak amplitudes of P, SH, and SV waves; combining the fundamental fault amplitudes for all possible values of strike, dip, and rake, at 10-deg increments; and determining the best fault orientation and depth as the one that yields the smallest misfit between observed and synthetic P/SH, P/SV, and SV/SH amplitude ratios. The ambiguity in the sense of motion on the nodal planes, which arises because amplitude ratios are used, is resolved by examining P-wave polarities. Source parameters for the largest events ( $M > 3.4$ ) were also determined by inversion of broadband displacement waveforms using a similar grid-search technique. Comparable results were obtained using both broadband waveforms and amplitude ratios.

The majority of aftershocks in the depth range between 0 and 12 km (in the crust of the North American Plate) show a large variety of fault-plane solutions; however, most solutions have north–south, nearly horizontal pressure axes. North–south, horizontal pressure axes also dominate the fault-plane solutions determined for events in the depth range between 15 and 22 km, but there is more consistency in the orientation of the nodal planes for events in this depth range. Seven of ten events have one nodal plane that dips to the south-southeast with a slip vector between 160 and 180 deg. If we interpret this plane to be the fault plane, the motion



on this plane suggests underthrusting of the Gorda Plate beneath the Pacific Plate. The observed slip direction of 160 to 180 deg is consistent, although more southerly, than the expected motion between the Gorda and Pacific plates. No evidence of convergent motion is found between the Gorda and Pacific plates along the Mendocino Fault farther to the west, suggesting that the rigid Pacific Plate prevents southward displacement of the Gorda Plate and the convergent motion is fully accommodated by internal deformation within the Gorda Plate. Toward the Mendocino Triple Junction where the Pacific Plate ends, it is reasonable to assume that the convergent motion will be accommodated by southward displacement of the Gorda Plate.

The focal mechanisms in the depth range between 23 and 35 km show the most consistency. These events form a tight northwest–southeast linear trend parallel to the events in the 15- to 22-km depth range. They all have one nodal plane parallel to this alignment, which we interpret as the fault plane. The motion across this plane is right lateral, consistent with this fault being the nearshore extension of the Mendocino Fault. This provides further evidence for the southward bend of the southern edge of the Gorda Plate as the Mendocino Triple Junction is approached. Figure 1 shows a schematic of the Gorda–Pacific plate geometry deduced from these fault-plane solutions. Near the Gorda Rise where the Gorda Plate is young and buoyant and the Pacific Plate is old and acts as a buttress, the convergent motion between the Gorda and Pacific plates is manifested as internal deformation within the Gorda Plate. As the Cape Mendocino Triple Junction is approached, the Gorda Plate has cooled a bit, and the buttressing effect of the Pacific Plate is diminished at its terminus, allowing the convergent plate motion to be taken up as southeast-directed underthrusting of the Gorda Plate beneath the Pacific Plate at depths between about 15 and 25 km. Below this depth, motion between the Gorda and Pacific plates occurs as right-lateral shear along the clockwise-rotated Mendocino Fault. The southeast convergence of the Gorda Plate relative to the Pacific Plate produces a tongue of southward-dipping Gorda Plate beneath North America (southern drag of Gorda Plate in Figure 1).

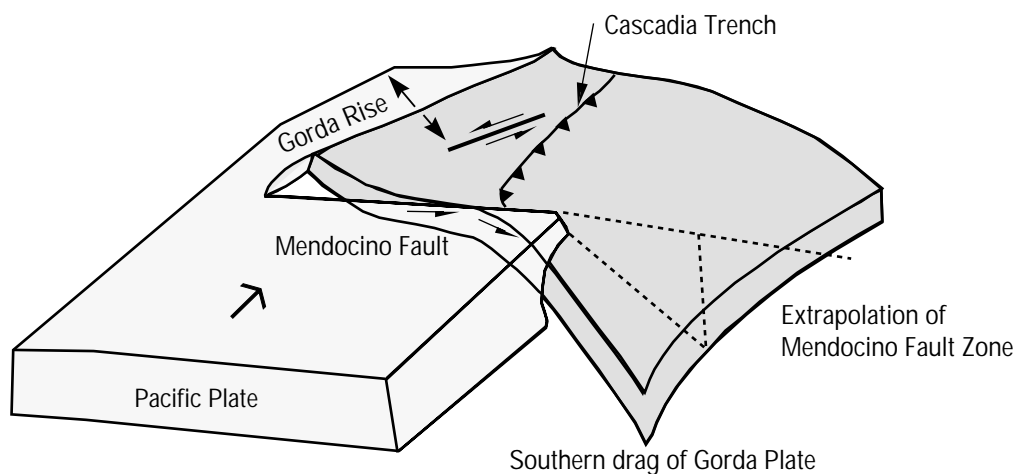


*Figure 1. Schematic interpretation of Gorda–Pacific plate interactions as determined from focal mechanisms of aftershocks of the Cape Mendocino earthquake. Subduction of the Gorda Plate beneath the Pacific Plate near the Cape Mendocino Triple Junction produces a tongue of Gorda Plate that extends south of the Mendocino Fault.*

1. Schwartz, S. Y. (1993), "Source Parameters of Local Earthquakes from Inversion of P and S Wave Amplitudes," *Trans. Am. Geophys. Union* **74**, 399.
2. Hubert, A., and S. Y. Schwartz (1993), "State of Stress at the Cape Mendocino Triple Junction from Inversion of Focal Mechanisms of the 1992 Petrolia, CA, Earthquake Sequence," *Trans. Am. Geophys. Union* **74**, 200.

## References

## Continuous Global Positioning System Monitoring in Northern California

**Principal Investigator:** Barbara A. Romanowicz (UC Berkeley)

**LLNL Collaborator:** Shawn Larsen

**Other Collaborator:** Richard Clymer (UC Berkeley)

### Abstract

*This project has helped establish a network of permanent global positioning system (GPS) receivers in northern and central California, called BARD—the Bay Area Regional Deformation network. The receivers and resources are being pooled between UC Berkeley (four receivers), LLNL (one receiver), and the U.S. Geological Survey (USGS, four receivers, previously installed). During FY 1994, three permanent receivers were installed at Columbia (CMBB), the Farallon Islands (FARB), and Tiburon (TIBB). The site at Tiburon is temporary. Data acquisition and archiving also were initiated at UC Berkeley. The data are available over Internet through the Northern California Earthquake Data Center (NCEDC).*

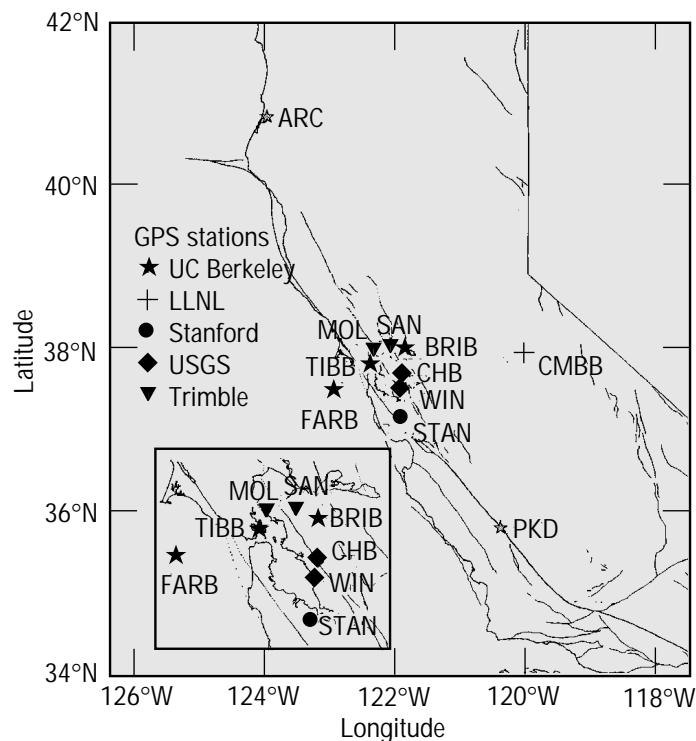
### Objectives

Our goal in this project is to establish a network of permanent GPS receivers, called BARD, in central and northern California, complementing the southern California effort, called Permanent GPS Geodetic Array (PGGA), and to make the data available through the NCEDC.

### Progress

Figure 1 shows the distribution of current and planned permanent GPS stations of the BARD network. Stations CMBB, FARB, and TIBB have been installed since October 1993, with partial support from this grant. Station CMBB is collocated with a broadband seismographic station of the Berkeley Digital Seismic Network

*Figure 1. Distribution of the GPS stations on the BARD network.*



(BDSN). Both CMBB and TIBB are linked to UC Berkeley through dial-up phone lines. Station FARB was made possible through cooperation with Jean Takekawa at the San Francisco Bay National Wildlife Refuge. This station represents a particular challenge, because access to the island is limited and thus the radio telemetry allows us to download data only once every 24 hours at UC Berkeley. As of September 1994, eight stations of the BARD array are operational.

Stations BRIB, CMBB, FARB, and TIBB are equipped with Ashtech Model “Z” GPS receivers, which are programmed to collect data in daily files, opening a new file each midnight UTC. The previous day’s files are downloaded daily via telephone modem to a networked personal computer on the UC Berkeley campus. Each downloaded RAM image file is then automatically converted to three working files. These four files, in Ashtech binary formats, are collectively called the raw files and are in turn converted to ASCII RINEX files (RINEX is the widely accepted standardized GPS data exchange format).

Using an archiving methodology developed for our seismic data, the daily files are automatically copied to an import directory on the UC Berkeley Data Center computer, where several consistency checks are made. All files, raw and RINEX, are then installed on the NCEDC optical jukebox, where they are available to the scientific community at large by anonymous file transfer protocol (ftp).

The shell script controlling this entire automated operation originated at Scripps Institute of Oceanography (authored by Keith Stark) and was modified by Douglas Neuhauser for use at the Seismographic Station.

The NCEDC archives continuous GPS data from the BARD network in both RINEX and the native binary format of the GPS receiver. Recent data are available in both RINEX and native binary formats; older data are available in RINEX format only.

The BARD data are available from the NCEDC system via anonymous ftp and are therefore accessible to anyone connected to the Internet.

```
host:      quake.geo.berkeley.edu (128.32.146.106)
account:   anonymous
password:  <your-email-address>
directory: /pub/gps
```

The BARD continuous data are organized into daily directories. For example, all RINEX data for day 120 of 1994 are located in the directory:

```
/pub/gps/rinex/1994/1994.120
```

The RINEX files are archived in UNIX compressed format, but they can be automatically uncompressed by the NCEDC ftp server upon retrieval. As an example of the data quality, Figure 2 shows the data obtained on the line BRIB to CMBB for the period 1993 day 96 to 1994 day 08.

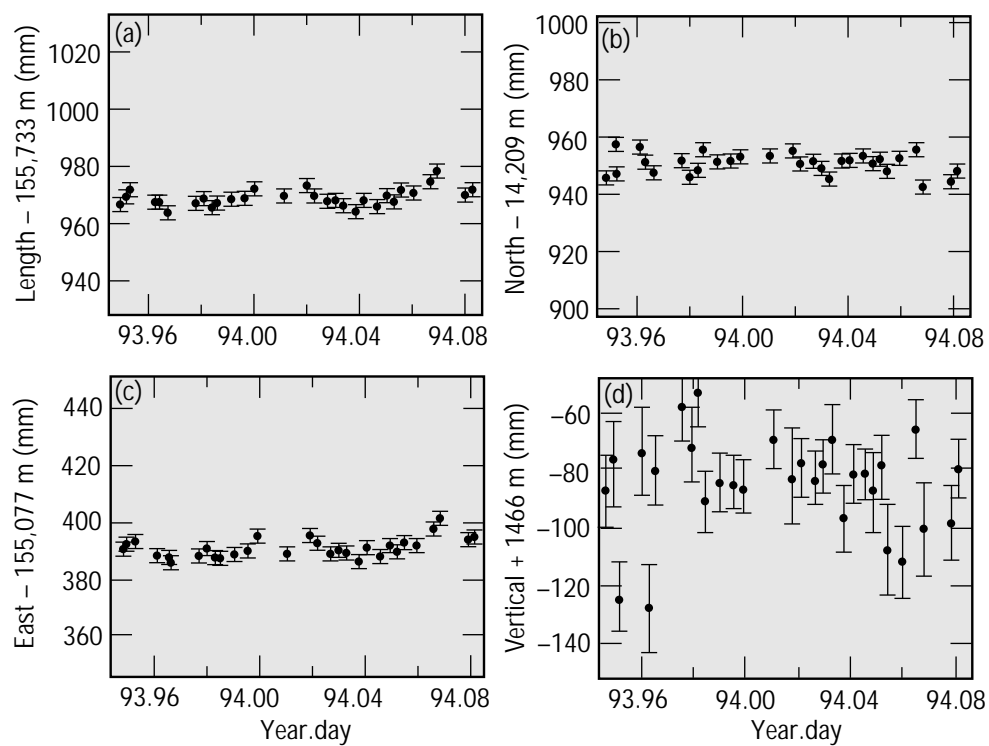


Figure 2. Data obtained on the line BRIB to CMBB for the period 1993 day 96 to 1994 day 08. Components shown are (a) length, (b) north, (c) east, and (d) vertical. Bias is fixed on all.

## Modeling Small-Scale Asthenosphere Convection under California

**Principal Investigator:** Jason Phipps Morgan (UC San Diego)

**LLNL Collaborators:** George Zandt and Charles Carrigan

**Student:** Mara Yale (UC San Diego)

*In FY 1994, we performed a series of two-dimensional numerical experiments to study small-scale convection in the asthenosphere beneath California. Plate reconstructions in this region constrain the timing of the opening of a slab window that is caused by the northward migration of the Pacific–Juan de Fuca–North America Triple Junction. Regional seismic tomographic inversions provide a snapshot of the current thermal structure of the upper mantle beneath California, showing several seismically fast fingers that drip off from the lithospheric lid. Using the timing provided by the history of the opening of the slab window and knowledge of the current thermal state, we performed numerical experiments to provide upper and lower bounds on the asthenosphere viscosity and demonstrate the effects of rheologies that depend on temperature, pressure, and strain rate.*

### Abstract

Our objective is to improve knowledge of asthenosphere properties under California by combining numerical modeling experiments with seismic data and tectonic reconstructions. We want to determine the effects of various physical parameters on the convective downwellings that have been imaged with seismic tomography in the asthenosphere under California. Spatial characteristics that are observed in tomographic images<sup>1</sup> include the aspect ratio of individual downwellings and the lateral spacing of the downwellings. Constraints on the timing of the development of these instabilities are provided by the depth of penetration and the known tectonic history, which fixes the timing of the initiation of the slab window. An additional constraint on the models is that the temperature contrast within the experimental downwellings must be large enough to be consistent with observed seismic velocity contrasts between the drips and ambient asthenosphere.

### Objectives

For the numerical experiments, we used a two-dimensional finite-element model. The model box was designed to mimic a vertical cross section running the length of California, 630 km long by 400 km deep. The initial temperature conditions define the lithosphere and the asthenosphere. Initially, temperature varies as a function of depth, such that within the lithosphere, there is a linear temperature gradient up to 800°C. Below the 800°C isotherm, the entire asthenosphere has an initial temperature of 1325°C (simulating hot asthenosphere filling in the slab window). The temperature of the top two rows of nodes within the asthenosphere are perturbed randomly with a 1% variation from 1325°C to seed the instability. Four rheologies were tested to determine the effects of a range of uniform viscosities and the effect of temperature- and pressure-dependent viscosity on the downwellings.

In the two uniform viscosity tests, the lithosphere is 1000 times more viscous than the asthenosphere. In the first experiment, the viscosity of the asthenosphere,  $\mu_{\text{asth}}$ , is  $10^{18}$  Pa · s, and the viscosity of the lithosphere,  $\mu_{\text{lith}}$ , is  $10^{21}$  Pa · s. Instabilities that develop in this experiment are significantly more narrow than the inferred downwellings observed in the tomographic image. The timing is also too fast with this rheology, as the downwellings reach a depth of 200 km in less than 2 million years.

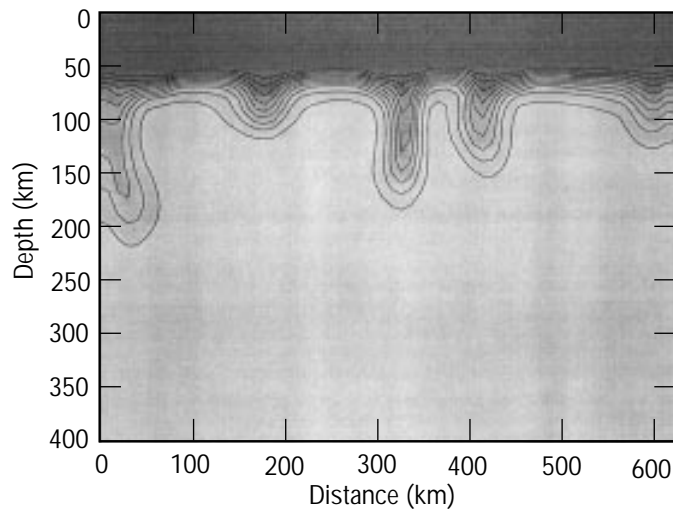
### Progress

In the second experiment (see Figure 1),  $\mu_{asth} = 10^{19} \text{ Pa} \cdot \text{s}$  and  $\mu_{lith} = 10^{22} \text{ Pa} \cdot \text{s}$ . This test results in downwellings that are much more consistent with those observed seismically both in terms of shape (aspect ratio) and in terms of timing. Downwellings reach ~200-km depth in ~8 million years. The temperature contrast is several hundred degrees, which is within the range that would be detected by a tomographic inversion.

We tested two different rheologies that are temperature- and pressure-dependent, according to experimentally derived diffusion and dislocation creep laws.<sup>2</sup> Both models result in a period of conduction that is significantly longer than that for the constant viscosity cases, followed by the development of downwellings that do not have significant temperature contrast (i.e., ~50°C). The temperature contrast within these downwellings is likely to be too small to be sensed seismically. These initial results suggest that temperature- and pressure-dependent viscosity mute rather than enhance the instabilities generated by our model.

We are developing techniques to animate the temporal evolution of the instabilities under California. Animation provides a means to visualize the time-dependent development of downwelling blobs. This collaborative effort is continuing. Future efforts will be focused on exploring a wider range of viscosity structures and on determining the resolution of the tomographic inversions by performing synthetic tomographic inversions on the temperature fields generated by the numerical models.

*Figure 1. Thermal state of the mantle 7.4 million years after initiation of instabilities for a two-layer constant viscosity case ( $\mu_{asth} = 10^{19} \text{ Pa} \cdot \text{s}$  and  $\mu_{lith} = 10^{22} \text{ Pa} \cdot \text{s}$ ). Contours are 50°C isotherms from 900°C to 1300°C.*



## References

1. Zandt, G., and C. R. Carrigan (1993), "Small-Scale Convective Instability and Upper Mantle Viscosity under California," *Science* **261**.
2. Karato, S., and P. Wu (1993), "Rheology of the Upper Mantle: A Synthesis," *Science* **260**, 771–778.

# Upper-Mantle P-Velocity Structure beneath Central and Northern California

**Principal Investigator:** Charles J. Ammon (UC Santa Cruz)

**LLNL Collaborators:** George Zandt and Stanley Ruppert

*The availability of thousands of travel times recorded on the central and northern California (CALNET) array provides an opportunity to study the uppermost mantle velocity variations beneath this part of California. We are using these data and tomographic imaging techniques to estimate the lateral variations in P velocity in the upper mantle beneath the region. Our preliminary modeling has delineated a relative low-velocity region beneath the northern California Coast Ranges that we interpret as an expression of the slab window produced by the northward migration of the Mendocino Triple Junction.*

## Abstract

Knowledge of the interaction between the mantle and the crust in California is critical for the development of regional tectonic models, which may provide important information for evaluating seismic hazards in the region. Several studies have suggested that at depth, the plate boundary has jumped from beneath the San Andreas Fault to beneath the Hayward–Calaveras Fault System in central California.<sup>1,2</sup> Detailed upper-mantle structure information is the key to identifying the Pacific–North American boundary at depth. Our objective is to use a large set of travel time measurements for the Pn wave to image lateral variations in the shallow upper mantle beneath central and northern California. Improved vertical resolution of velocity variations in the upper 30 km of the mantle will provide better constraints for convection models of the California upper mantle,<sup>3</sup> particularly the interaction between the mantle convection and the crust.

## Objectives

For this project, we selected a simple imaging technique to perform the travel time inversions, and we assumed the rays follow great-circle paths. As with most tomographic applications, ours requires care in selecting the best-quality measurements and equity in geographic sampling. In FY 1994, we performed inversions on geographically weighted data. The results are in two parts: relative station corrections that identify regions with relatively slow or thick crust, and the tomographic results that show lateral velocity variations in the shallow upper mantle.

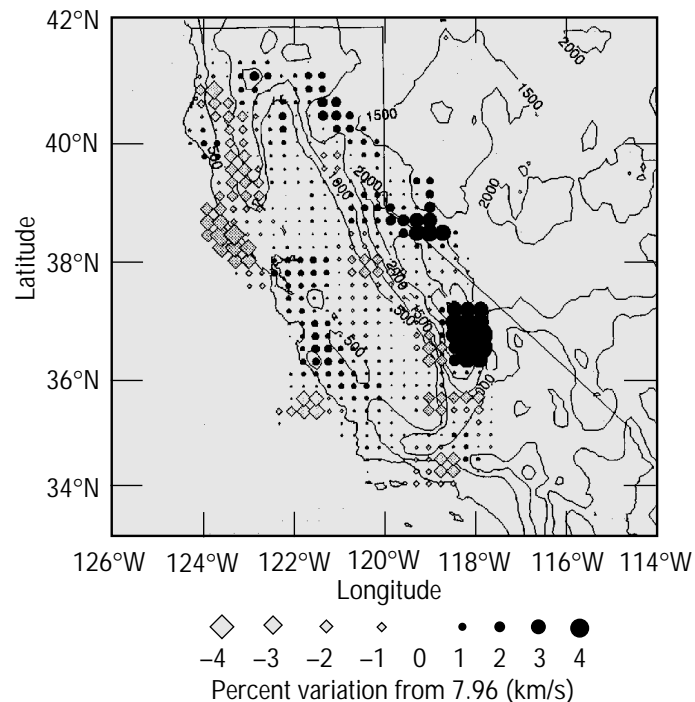
## Progress

From the relative station corrections, we infer a general trend of increasing crustal thickness in the northern Coast Ranges. Changes in geology across the San Andreas Fault south of San Francisco are also apparent in the station residuals. In Figure 1, we present relative velocity variations in the upper mantle beneath the study area. Diamonds represent relatively slow regions, and circles show relatively fast regions. These results are constrained to correlate geographically so we can estimate the most robust features in the travel-time data. The San Francisco Bay area is relatively fast, compared with the region in the northern Coast Ranges. We believe the large anomalies on the edges of the study area are artifacts, so we do not interpret them.

The major anomaly within the study area is the low-velocity region associated with the northern Coast Ranges between 39° and 41°N that agrees with teleseismic imaging of northern California.<sup>4</sup> These results are consistent with simple models of

the thermal evolution of northern California associated with the northward migration of the Mendocino Triple Junction and probably contribute to the high elevation of the northern Coast Ranges (Figure 1).

*Figure 1. Relative velocity variations in the upper mantle beneath the study area. Diamonds = relatively slow regions; circles = relatively fast regions. Results are constrained to correlate geographically so the most robust features in the travel-time data can be estimated. The San Francisco Bay area is relatively fast, compared with the region in the northern Coast Ranges.*



## References

1. Zandt, G., and K. P. Furlong (1982), "Evolution and Thickness of the Lithosphere beneath Coastal California," *Geology* **10**, 376–381.
2. Furlong, K. P., W. D. Hugo, and G. Zandt (1989), "Geometry and Evolution of the San Andreas Fault Zone in Northern California," *J. Geophys. Res.* **94**, 3100–3110.
3. Zandt, G., and C. R. Carrigan (1993), "Small-Scale Convective Instability and Upper Mantle Viscosity under California," *Science* **261**, 460–463.
4. Benz, H. M., G. Zandt, and D. H. Oppenheimer (1992), "Lithospheric Structure of Northern California from Teleseismic Images of the Upper Mantle," *J. Geophys. Res.* **97**, 4791–4807.



## Monazite as a Prograde Geochronometer: Determination of Pb Diffusion Rates in Monazite

**Principal Investigators:** Daniel L. Farber, Kevin D. McKeegan, and  
T. Mark Harrison (UC Los Angeles)

**LLNL Collaborator:** Frederick J. Ryerson

### Abstract

*Monazite has been shown to be a particularly useful geochronometer for obtaining information along the prograde path of metamorphic pressure–temperature–time histories. Below temperatures of ~700°C, the growth history of the monazite in a metamorphic rock may be preserved by Pb isotopes within concentric growth zones. However, the preservation of these values is affected by subsequent monazite growth and diffusive processes. Thus, we are measuring diffusion coefficients of Pb, Th, and U in monazite to attempt to quantify the chemical relaxation of isotopic growth profiles.*

### Objectives

Among common accessory phases, monazite is singular in its potential for use as a prograde thermochronometer. Thus, to obtain the information needed to apply monazite thermochronology, we are trying to quantify Pb, Th, and U diffusion in monazite. We also are studying the stability and kinetics of monazite growth reactions in metamorphic assemblages, and we are developing U–Pb microanalysis in monazite. In FY 1994, we focused on developing experimental techniques for measuring Pb diffusion in monazite.

The kinetic properties of monazite are somewhat unique among the accessory minerals commonly used for geochronology. Lead diffusion in restitic zircons is generally too sluggish to record (in the form of concentration profiles) details of the melt history. Apatite is insufficiently retentive to preclude complete isotopic homogenization during anatexis. Monazite, however, has intermediate retention characteristics that endow it with unique potential. Although once perceived to have relatively low closure temperature for Pb (approximately 500 to 650°C), these estimates were little more than speculation or minimum estimates. However, Copeland et al.<sup>1</sup> clearly documented a closure temperature of >730°C for monazite, which has been confirmed in subsequent studies. Thus, provided peak temperatures do not exceed about 700°C, the growth history of the monazite in a metamorphic rock is preserved by Pb isotopes within concentric growth zones.

Indeed, what makes this phase particularly appealing for the study of orogeny is that monazite, although not uncommon as a detrital phase in quartzites,<sup>2</sup> is essentially unknown in low-grade pelitic rocks. Monazite is unstable during diagenesis and does not reappear until epidote-amphibolite facies. Therefore, unlike zircons, Pb isotopic zoning in metamorphic monazites preserves only the prograde metamorphic history.

### Progress

Previous attempts to measure Pb diffusion in monazite were hampered by a lack of gem-quality natural monazites or by the presence of lead inclusions in synthetic material grown in lead phosphate flux. Thus, we developed a new hydrothermal technique for growing monazites in the piston cylinder apparatus. Using strong

nickel capsules and noble metal liners, we can grow crystals with diameters up to 500  $\mu\text{m}$  for subsequent use in the diffusion anneals (Figure 1). The synthetic crystals grown with this technique are free of the lead inclusions that hampered our earlier work and have provided stable crystal faces in several exchange media. Figure 2 shows a typical  $^{208}\text{Pb}$  diffusion profile collected from a sample annealed at 1100°C for  $5.8 \times 10^5$  s. The excellent agreement of the calculated profile with our data suggests that both the constant surface concentration and a stable crystal were maintained during the diffusion anneal. This combination of hydrothermally grown monazites and subsequent diffusion anneals should yield accurate kinetic parameters for the inversion of Pb isotopic profiles in natural monazites.

*Figure 1. Secondary electron image of a monazite crystal grown in the piston cylinder apparatus at 5 kbar and 600°C (scale bar = 100  $\mu\text{m}$ ). The well-developed crystal faces provide excellent surfaces for the subsequent diffusion anneal. Note that the grayish quench material adhering to the crystal faces is removed prior to the diffusion anneal.*

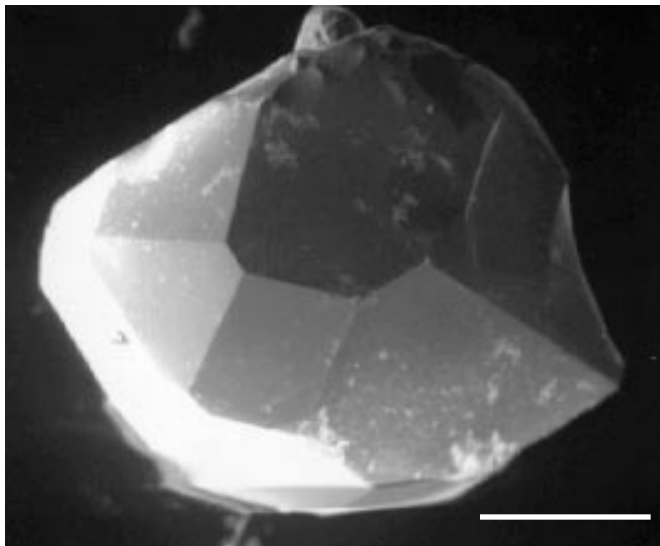
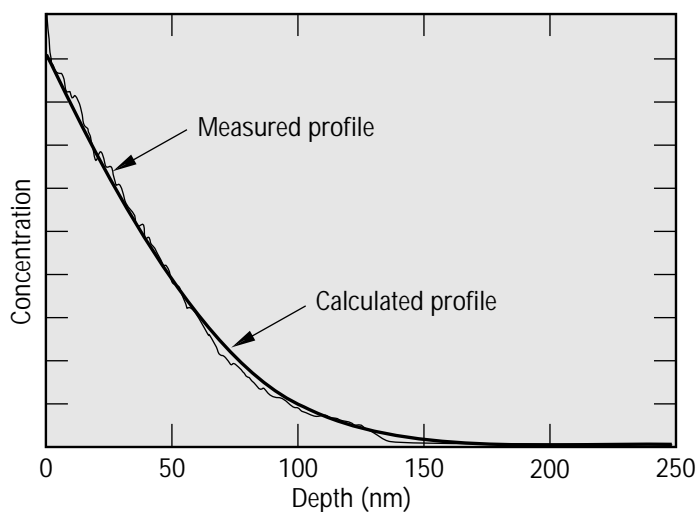


*Figure 2. Typical Pb diffusion profile in monazite produced from an anneal between monazite and PbS-liquid in an evacuated quartz tube. In the calculated profile, we assumed a run duration of  $5.8 \times 10^5$  s, a diffusion coefficient of  $3.3 \times 10^{-17} \text{ cm}^2/\text{s}$ , and a constant surface concentration.*



---

**References**

1. Copeland, P., R. R. Parrish, and T. M. Harrison (1988), "Identification of Inherited Radiogenic Pb in Monazite and Its Implications for U–Pb Systematics," *Nature* **333**, 760–763.
2. Overstreet, W. C. (1967), *The Geological Occurrence of Monazite*, U.S. Geol. Surv. Prof. Paper 530, 327 p.

## Actinide Element Partitioning at High Pressures between Coexisting Silicate Melts and Crystals: Constraints on Magmatic Segregation Processes

**Principal Investigator:** Quentin Williams (UC Santa Cruz)

**LLNL Collaborators:** Frederick J. Ryerson and Henry Shaw

**Students:** Charles C. Lundstrom and Daniel L. Farber (UC Santa Cruz)

---

### Abstract

*In this project, we are characterizing the manner in which geochemical heterogeneity is produced and annihilated within the planet. We have nearly completed our work on chemical diffusion rates in the phases presumed to predominate in the Earth's mantle between 400- and 670-km depth. These results demonstrated that the high-pressure polymorphs of  $\text{Mg}_2\text{SiO}_4$ ,  $\beta$ -phase and  $\gamma$ -spinel, each have cation diffusion rates that are nearly 3 orders of magnitude faster than those within the lower-pressure, olivine-structured phase. Such a profound difference in diffusion rates was not only unexpected but also has profound implications for the rates at which subducted oceanic crust is rehomogenized into the Earth's mantle. Over Earth history, the total volume of subducted, geochemically differentiated material (slabs) is likely to approach or exceed the present-day volume of the Earth's silicate mantle. Yet, from both seismological and geochemical probes, the Earth's mantle appears to be largely chemically homogeneous. Thus, the principal question this facet of our work addresses is: Where are the slabs of yesteryear?*

---

### Objectives

Our objective in this project is to place experimental constraints on the mechanisms and rates of formation and destruction of the lithosphere.

---

### Progress

Our results<sup>1</sup> provide a possible solution to the fundamental dilemma of Earth evolution. The fast diffusion rates we document within the high-pressure polymorphs of olivine imply that if, as appears likely, subducted material spends a significant amount of time in the depth range between 400 and 670 km, this material is homogenized relatively rapidly by a mixture of convective stirring and diffusive equilibration. In short, as phrased by others,<sup>2</sup> slabs can rapidly become ghosts of their former selves in this region of the planet. Thus, this region of the Earth's mantle can effectively function as an eraser of subducted material, by reincorporating material that previously was chemically stratified into the mainstream of mantle convection. These results have implications for the manner in which the Earth has geochemically differentiated, for the ultimate fate of material in the downgoing portion of the plate tectonic cycle, and for the chemical stratification of the Earth's interior.

Our second major area of effort has been oriented toward drawing experimental constraints on the timescale and depth range over which oceanic crust (basalt) is generated through melting at mid-ocean ridges. Among the primary data that constrain this melting process are the varying amounts of elements in the radioactive decay series of uranium and thorium, which appear in both recently generated oceanic crust and where available, in solid residua from the melting process. Correct interpretation of such data requires a detailed knowledge of the solid-liquid partitioning behavior of the elements of the uranium decay series. We have characterized the partitioning behavior of U, Th, Ba (an analog for Ra), and Pb between basaltic liquid and a major mantle phase, clinopyroxene (ideally  $\text{CaMgSi}_2\text{O}_6$ ), over

a range of different chemical conditions.<sup>3</sup> Our results document that the partitioning behavior of these elements crucially depends on the trivalent ion (particularly aluminum and chromium) content of the clinopyroxene. This chemical dependence not only resolves discrepancies between previous datasets, but it also provides a means for assessing chemical differences observed between basalts. Because the aluminum content of clinopyroxene typically increases with depth, shifts in the abundance of different members of the uranium decay series may reflect variations in the depth of melting, which ultimately produces the oceanic crust.<sup>3</sup> Thus, these results have the prospect of providing an additional means by which one may constrain the location, composition, and degree of partial melting of a source region from the chemical composition of an igneous rock. Such constraints are not only the ultimate goal of igneous petrologists and geochemists, but in this case, they also provide further insight into the genesis and chemical variability of the most abundant igneous rock type on the surface of the solid Earth.

1. Farber, D. L., Q. Williams, and F. J. Ryerson (1994), "Diffusion in  $\text{Mg}_2\text{SiO}_4$  Polymorphs and Chemical Heterogeneity in the Mantle Transition Zone," *Nature* **371**, 693–695.
2. Kellogg, L.H. (1994), "Geochemistry—Fast Cleaning in the Deep," *Nature* **371**, 656.
3. Lundstrom, C. C., et al. (1994), "Compositional Controls on the Partitioning of U, Th, Ba, Pb, Sr, and Zr between Clinopyroxene and Haplobasaltic Melts—Implications for Uranium Series Disequilibria in Basalts," *Earth Planet. Sci. Lett.* **128**(3–4), 407–423.

## References

## Point-Defect Diffusion in Olivine Rock

**Principal Investigator:** Steven Constable (UC San Diego)

**LLNL Collaborator:** Alfred G. Duba

---

### Abstract

*We have made extensive measurements of electrical conductivity and thermopower on an olivine-rich rock as a function of temperature between 850 and 1200°C and oxygen fugacity between  $10^{-10}$  and 1 Pa. The reequilibration of conductivity after changes in oxygen fugacity was also modeled to recover the diffusivity of the point defect responsible for the oxygen fugacity dependence of conductivity.*

*The observed electrical conductivities and thermopowers are incompatible with small polaron conduction (the accepted mechanism in olivine at this temperature) and require the addition of a second conducting defect. The diffusivity, although previously considered to be consistent with magnesium vacancy diffusion, exhibits a negative dependence on oxygen fugacity, which has not previously been observed. The behavior of diffusivity, thermopower, and conductivity all imply that electrical properties change from one dominant defect to another across the range of oxygen fugacity in which olivine is stable.*

---

### Objectives

An understanding of defect chemistry is important in the study of the electrical conductivity of Earth's mantle. Currently, it is difficult to measure the electrical conductivity of mantle materials under simultaneously controlled conditions of pressure, temperature, oxygen fugacity, water activity, silica activity, and iron activity. A thorough understanding of the point-defect mechanisms that determine conductivity in olivine rocks will help us extrapolate measurements to conditions applicable to the mantle. We also have an insufficient understanding of the conductivity of high-pressure mineral phases in the mantle. Again, an understanding of the factors that control conductivity in the low-pressure phase may help us predict and understand the conductivity of the high-pressure minerals.

Because silicates are insulators or, at best, poor semiconductors, their electrical conductivity depends strongly on the defect population. Also, because electrical measurements are relatively straightforward, we can monitor easily and accurately how variation of environmental parameters can affect the defect population. Conductivity can be determined within an error of 0.1 of a log unit, temperature within 3 K, and oxygen fugacity within 0.1 of a log unit. In each case, the precision of the measurement is at least 10 times better than the stated accuracy. We use the variation of the conductivity resulting from changes in oxygen fugacity, at constant temperature, to calculate the diffusion of the defects responsible for conduction in olivine. To sort among possible mechanisms that could be responsible for conduction in olivine at any given temperature, we used the defect model of Hirsch and Shankland,<sup>1</sup> our measurements of diffusion, and our measurement of the sign and oxygen fugacity dependence of thermoelectric power over the relatively large temperature range.

---

### Progress

The rock used in this study is a lherzolite from Mount Porndon, Australia, with approximate modal composition of 3% clinopyroxene, 31% orthopyroxene, 1% spinel, and 65% olivine and a grain size of about 1 mm. Electrical conductivity and thermopower were measured in an apparatus that is described in detail by Duba et al.<sup>2</sup> Oxygen fugacity is controlled by a metered flow of CO and CO<sub>2</sub> through the apparatus, and electrical conductivity measured as a function of oxygen fugacity

exhibits approximately a 1/11 power dependence. Because of this dependence, step-function changes in the gas mix cause a reequilibration that can be monitored by electrical conductivity measurements. Mathematical models of diffusion can be fitted to the reequilibration data to recover the diffusivity of the rate-limiting defect. Thermopower was also determined, using the method described by Schock et al.<sup>3</sup> This measurement determines the sign and abundance of the dominant charge carrier as the result of the migration of the conducting species from the hotter electrode of a sample in a temperature gradient.

We collected 5800 hours of data at temperatures between 850 and 1200°C, with 67 changes of gas mix and 6 determinations of thermopower. Thermopower at 1200°C is about 170  $\mu\text{V}/\text{m}/\text{K}$  and has a positive dependence on oxygen fugacity. The observed activation energy for diffusivity (2.1 eV) between 850 and 1200°C is in good agreement with published values for magnesium vacancies and previous measurements using electrical conductivity.<sup>4</sup> The magnitude is higher ( $1.0 \times 10^{-10} \text{ m}^2 \text{ s}^{-1}$  at 1200°C). However, taking a smaller effective grain size to allow for cracking within grains would lower this value by as much as an order of magnitude. Although our data seem compatible with a magnesium vacancy mechanism, diffusivity exhibits a dependence on oxygen fugacity of approximately a  $-1/5$  power. This dependency is not seen in similar experiments on larger, single-crystal specimens, suggesting that a rate-limited reaction with the atmosphere is not the reason. Rather, we consider that grain boundary diffusion or a rate-limited buffer reaction with the pyroxene in the sample is responsible.

We constructed a mathematical model for conductivity and thermopower as a function of oxygen fugacity and attempted to fit it to our data. A model for small polarons, which are considered to be the conducting defect in olivine at these temperatures, predicts a larger thermopower than observed with a negative, rather than positive, oxygen dependence. The model also predicts an electrical conductivity with a 1/5, rather than 1/11, power dependence on oxygen fugacity. At least one other conducting defect species must be invoked to explain the observed magnitude and oxygen dependence of thermopower, and both electron/polaron and polaron/magnesium vacancy conduction can be made to fit the conductivity and thermopower data if a constant polaron or magnesium vacancy term is included (or a 1/11 power dependence of defect population taken). However, in our model, the small magnitude of the thermopower requires unrealistically high concentrations of polarons. Again, conduction along grain boundaries may be responsible for the lowered thermopowers.

1. Hirsch, L. M., and T. J. Shankland (1993), "Quantitative Olivine-Defect Chemical Model: Insights on Electrical Conduction, Diffusion, and the Role of Fe Content," *Geophys. J. Int.* **114**, 21–35.
2. Duba, A. G., R. N. Schock, E. Arnold, and T. J. Shankland (1990), "An Apparatus for Measurement of Electrical Conductivity to 1500°C at Known Oxygen Fugacity," in *The Brittle-Ductile Transitions in Rocks*, A. G. Duba, W. B. Durham, J. W. Handin, and H. F. Wang, Eds., *Geophys. Monogr. Ser.* **56** (American Geophysical Union, Washington, DC), pp. 207–210.
3. Schock, R. N., A. Duba, and T. J. Shankland (1989), "Electrical Conduction in Olivine," *J. Geophys. Res.* **94**, 5829–5839.
4. Duba, A., and S. C. Constable (1993), "The Electrical Conductivity of a Lherzolite," *J. Geophys. Res.* **98**, 11885–11900.

## References

## Measurements of Muon-Induced $^{10}\text{Be}$ and $^{26}\text{Al}$ in Terrestrial Quartz

**Principal Investigator:** Kunihiko Nishiizumi (UC Berkeley)

**LLNL Collaborators:** Robert C. Finkel and Marc W. Caffee

---

### Abstract

*We have been investigating the concentration of the muon-induced radionuclides  $^{10}\text{Be}$  (half-life = 1.5 million years) and  $^{26}\text{Al}$  (0.71 million years) in terrestrial quartz. The goal of this work is to determine the production rates of  $^{10}\text{Be}$  and  $^{26}\text{Al}$  in quartz by cosmic-ray muons underground. We collected samples from three deep mines. Quartz purification for all samples has been completed, and the  $^{10}\text{Be}$  and  $^{26}\text{Al}$  measurements are under way. Preliminary radionuclide measurements on three samples have been completed. The preliminary results indicate that measurable amounts of  $^{10}\text{Be}$  and  $^{26}\text{Al}$  are found in quartz from deeper than 300 m underground.*

---

### Objectives

The measurement of in situ-produced cosmogenic nuclides in terrestrial surface samples has opened a new field of earth sciences. We have developed techniques for studying the rates of geomorphologic processes such as erosion, glacier movement, and volcanic eruptions, using the in situ-produced cosmogenic nuclides  $^{10}\text{Be}$ ,  $^{26}\text{Al}$ , and  $^{21}\text{Ne}$  in a variety of terrestrial settings.<sup>1</sup> Production rates of these nuclides are very low in terrestrial rocks, on the order of tens of atoms per gram of rock per year. Nevertheless, the development of accelerator mass spectrometry (AMS) for radionuclides and improvements in mass spectrometry for noble gases have recently made possible the measurement of in situ-produced nuclides in terrestrial samples.

The concentration of in situ-produced cosmogenic nuclides in terrestrial samples is controlled by both the erosion/deposition rate and the exposure time. To apply the in situ method to problems of geomorphology, we must know the production rates and, in particular, the production ratio of the two nuclides. Two of the earliest studies of in situ-produced cosmogenic nuclides at the Earth's surface were focused on muon-induced  $^{26}\text{Al}$  and  $^{129}\text{I}$  in terrestrial rocks.<sup>3,4</sup> With further work, it became clear that, in general, muon-induced reactions were of minor importance relative to other production pathways. Several years ago, we determined the production rate of  $^{10}\text{Be}$  to be 6.0 atom/g  $\text{SiO}_2$  year at sea level (geomagnetic latitude  $> 50^\circ$ ), the production rate of  $^{26}\text{Al}$  to be 36.8 atom/g  $\text{SiO}_2$  year, and the  $^{26}\text{Al}/^{10}\text{Be}$  ratio to be 6.1 (Ref. 2). In that work,  $^{10}\text{Be}$  and  $^{26}\text{Al}$  induced by muons were considered to make only a small contribution to the overall production, which is dominated by cosmic-ray secondary neutrons.

Muon production remains a minor although not negligible factor in cosmogenic nuclide production near the Earth's surface. However, as the result of our recent work (unpublished), we realized that muon-induced reactions can be important in certain cases involving deep burial or high erosion rates. Therefore, to expand the range and reliability of the applications of surface-exposure dating to geologic problems, we considered it important to determine the depth dependence of muon-induced reactions in the Earth's surface. In this work, we focus on measuring the depth profiles of  $^{10}\text{Be}$  and  $^{26}\text{Al}$  in deep mines.

Two types of muon interactions were considered for this study: (1) stopped negative muon capture and (2) photonuclear effects by fast muons. Aluminum-26 in quartz is produced by both reactions:  $^{28}\text{Si}(\mu^-, \nu_\mu 2n)$  and  $^{28}\text{Si}(\gamma, np)$ . The  $^{10}\text{Be}$  and  $^{26}\text{Al}$  muon-induced reactions will make up an important part of the in situ production in terrestrial quartz. However, the production rates and depth profiles of muon-induced  $^{10}\text{Be}$  and  $^{26}\text{Al}$  in terrestrial quartz are not as yet well understood.



Knowledge of the production rates of  $^{10}\text{Be}$  and  $^{26}\text{Al}$  by muon interactions not only provides the basic data needed to calculate the surface-erosion rates but also will allow us to determine the history of the cosmic-ray muon flux using geologic samples. Our study involved a collaborative investigation to measure cosmic-ray muon-produced radionuclides in terrestrial samples and was conducted at the Space Sciences Laboratory at UC Berkeley and the Nuclear Chemistry Division and Center for Accelerator Mass Spectrometry (CAMS) at LLNL. The goal of this work is to determine the production rates of  $^{10}\text{Be}$  and  $^{26}\text{Al}$  in quartz by cosmic-ray muons underground. In FY 1994, we began a series of measurements to determine the content of long half-lived radionuclides  $^{10}\text{Be}$  and  $^{26}\text{Al}$  in quartz extracted from terrestrial rocks, using AMS at the LLNL CAMS.

We collected rock samples from three mines: Homestake gold mine in Lead, South Dakota; Kamioka zinc mine in Japan; and Kamaishi iron mine in Japan. (We thank Drs. R. Davis Jr., M. Imamura, K. Sakamoto, and W. Sakurai for sample collection.) The former two mines are also being used as neutrino observatories.<sup>5</sup> The sample depths range from 91 to 2393 m below surface. Clean quartz samples were isolated from various rock samples by a selective chemical separation procedure. Since the expected concentrations of both  $^{10}\text{Be}$  and  $^{26}\text{Al}$  are extremely low, we separated large amounts of clean quartz, ranging from a few hundred grams to 1 kg, from the 17 rock samples we studied. All quartz separations have been done, and clean quartz has been obtained from all but one sample. The  $^{10}\text{Be}$  and  $^{26}\text{Al}$  measurements are in progress. The preliminary results to date are shown in Table 1. After we measure  $^{10}\text{Be}$  and  $^{26}\text{Al}$  in other samples (in progress), we will obtain muon production of these nuclides.

Table 1. Preliminary results of  $^{10}\text{Be}$  and  $^{26}\text{Al}$  in quartz from deep mines.

Sample	Depth (m)	Weight (g)	Al (ppm)	$^{10}\text{Be}/\text{SiO}_2$ (103 atom/g)	$^{26}\text{Al}/\text{SiO}_2$ (103 atom/g)
Kamaishi-1	300	43.06	50	$12.5 \pm 10.0$	$7.2 \pm 3.9$
Kamaishi-2	300	61.62	46	$12.0 \pm 3.7$	$4.1 \pm 1.8$
Kamioka-3	790	131.80	29	$4.2 \pm 1.8$	$4.9 \pm 1.4$
Kamioka-5	555	152.24	87		$1.7 \pm 1.6$

1. Nishiizumi, K., C. P. Kohl, R. Dorn, J. Klein, D. Fink, R. Middleton, D. Lal, and J. R. Arnold (1993), "Role of In Situ Cosmogenic Nuclides  $^{10}\text{Be}$  and  $^{26}\text{Al}$  in the Study of Diverse Geomorphic Processes," *Earth Surface Processes Landforms* **18**, 407–425.
2. Nishiizumi, K., D. Lal, J. Klein, R. Middleton, and J. R. Arnold (1986), "Production of  $^{10}\text{Be}$  and  $^{26}\text{Al}$  by Cosmic Rays in Terrestrial Quartz In Situ and Implications for Erosion Rates," *Nature* **319**, 134–136.
3. Tanaka, S., K. Sakamoto, J. Takagi, and M. Tsuchimoto (1968), "Search for Aluminum-26 Induced by Cosmic-Ray Muons in Terrestrial Rock," *J. Geophys. Res.* **73**, 3303–3309.
4. Takagi, J., W. Hampel, and T. Kirsten (1974), Cosmic-Ray Muon-Induced  $^{129}\text{I}$  in Tellurium Ores," *Earth Planet. Sci. Lett.* **24**, 141–150.
5. Davis, R. J., D. S. Harmer, and K. C. Hoffman (1968), "Search for Neutrinos from the Sun," *Phys. Rev. Lett.* **20**, 1205–1209.

## References

## Studies of Soil Dynamics and Loess Paleoclimate Records Using Cosmogenic Nuclide $^{10}\text{Be}$

**Principal Investigator:** Devendra Lal (Scripps Institution of Oceanography, UC San Diego)

**LLNL Collaborators:** Marc W. Caffee, Robert C. Finkel, and John R. Southon

**Student:** Zhaoyan Gu (UC San Diego)

---

### Abstract

*The Chinese loess plateau contains a unique sequence of continuous deposition of aeolian dust back to 2.5 million years before present. This sequence has been well dated with the magnetostratigraphic method, and it has been stratigraphically correlated using oxygen isotopes, mineralogy, and other climate indicators. The dust layers were subsequently altered by in situ weathering, especially during wet and high-temperature periods, and are thus a proxy for climatic changes in the past 2.5 million years. Previous studies on concentrations of cosmogenic  $^{10}\text{Be}$  of bulk loess/paleosol samples showed a strong correlation in  $^{10}\text{Be}$  with climate. Realizing that a more detailed  $^{10}\text{Be}$  analysis, combined with data on U, Th, and certain trace elements, can yield quantitative climatic information as well as information on the in situ geochemical processes operative in chemical weathering, we are studying dust layers from five sites in the Chinese loess plateau. The data obtained have revealed information on the total  $^{10}\text{Be}$  fluxes, relative amounts of wet precipitation, and the degree of chemical changes of the soils in the past 2.5 million years. Our work also points to new directions in which future investigations of the loess deposits would be useful.*

---

### Objectives

The well-dated Chinese loess deposits offer a valuable resource for studying climatic changes back to 2.5 Ma, the global-scale atmospheric production and removal history of  $^{10}\text{Be}$ , the nature of geochemical processes occurring in the weathering of soils in well-characterized soil layers, and the incorporation of  $^{10}\text{Be}$  in the authigenic minerals. Since the dust deposition is continuous and not too slow (about 5 to 10 cm/1000 years), a detailed characterization of the chemical and isotopic changes in the dust layers would be expected to provide (1) the history of climatic changes back to 2.5 Ma and (2) the ground truth about the nature of geochemical changes in soil weathering processes. Therefore, we have completed a detailed isotopic and elemental characterization of the soil layers. Radionuclides studied are the cosmogenic  $^{10}\text{Be}$ , radiogenic U and Th, and trace elements (e.g., Be, Ti, Rb, Sr, and rare-earth elements). Our studies do seem to fulfill our hopes and goals.

---

### Progress

During FY 1993, we worked with Zhaoyan Gu, a student from the Institute of Geology, Chinese Academy of Sciences, Beijing, to complete preliminary studies of the cosmogenic  $^{10}\text{Be}$ . We examined  $^{10}\text{Be}$  in different size and chemical fractions of loess/paleosol samples and in the red-clay sediments underlying the dust layers from a few sites. We found that the loess samples generally had appreciably lower  $^{10}\text{Be}$  concentrations than the paleosol samples and that their concentrations decreased monotonically with depth in good accord with the age of the estimates based on magnetic stratigraphy.<sup>2</sup> The decay-corrected  $^{10}\text{Be}$  concentrations of loess samples are distributed within a narrow interval (about +25%), suggesting that at deposition the  $^{10}\text{Be}$  concentrations of dust were well constrained within a narrow

range and were not modified appreciably after deposition. The paleosols however show variable  $^{10}\text{Be}$  concentrations, with higher concentrations during periods of higher temperature based on  $\delta^{18}\text{O}$  SPECMAP data. Our observations are consistent with the earlier deductions made by Shen et al.<sup>1</sup> for the 0- to 0.7-Ma period, based on their  $^{10}\text{Be}$  observations in the Luochuan section.

We believe a multitracer study of the dust deposits would provide high-resolution climatic data (e.g., winds, temperature, and precipitation) and ground truth data about in situ soil weathering processes. Therefore, we have now carried out more detailed studies of soil sequences from Jixian during the time period 0 to 0.13 Ma and from Weinan and Baoji during the period 0 to 2.5 Ma. We also studied red-clay sediments below the dust deposit layers from two sites (Lintai and Baoji). A total of 63 loess/paleosol and the red-clay sediment samples were used for  $^{10}\text{Be}$  concentrations. Several samples were also analyzed for  $^{10}\text{Be}$  concentrations in different chemical phases and size fractions. The total number of  $^{10}\text{Be}$  analyses was 156.

In the 2.5-Ma dust deposit sequences at Weinan (Figure 1), the loess samples have a mean decay-corrected  $^{10}\text{Be}$  concentration of  $(2.7 \pm 0.5) \times 10^8$  atoms/g. A few loess samples have significantly higher concentrations than the mean value. These samples appear to have received  $^{10}\text{Be}$  from the overlying layers, which exhibit significantly higher precipitation fluxes. The observed variations in the paleosol samples are significantly correlated with several physical/chemical indices that are indicative of wet precipitation and weathering, e.g., Ti/Si ratios,  $^{238}\text{U}/^{232}\text{Th}$  ratios, dissolved  $^9\text{Be}$  concentrations, and magnetic susceptibility. Figure 2 shows the correlation between  $^{10}\text{Be}$  concentrations and Ti/Si ratios of the samples.

Most of the  $^{10}\text{Be}$  is found adsorbed on small particles ( $<4\ \mu\text{m}$ ), 70% in loess and 90% in paleosols, on average. The excess concentrations of  $^{10}\text{Be}$  in loess samples over the mean value show a high degree of correlation with the grain-size distribution. A similar effect is observed for paleosols, but several samples have very high  $^{10}\text{Be}$  concentrations, indicating a higher-than-average precipitation during their deposition.

The red-clay sediment samples from Lintai, which has a good magnetostratigraphically dated sequence, show a good anti-correlation between  $^{10}\text{Be}$  concentration and sedimentation rate. The  $^{10}\text{Be}$  deposition rate was much lower during the red-clay sedimentary phase, even lower than during the loess deposition, indicating appreciable reduction in the precipitation rate from 2.5 to 5.5 Ma.

The fallout of  $^{10}\text{Be}$  in the Chinese loess plateau is controlled by several climatic factors, such as wet precipitation rate, aeolian dust fluxes, winds, and of course, the global average production rate of  $^{10}\text{Be}$ . Furthermore, the incorporation of  $^{10}\text{Be}$  in the dust layers depends on the grain-size distribution in the soil and on temperature and rainfall. The two latter factors control carbonate leaching and soil weathering rate. Incorporating these parameters, guided by the ice core date and the SPECMAP  $\delta^{18}\text{O}$  record, with the assumption of a uniform  $^{10}\text{Be}$  production rate in the past, we have derived a plausible history of the time dependence of precipitation rate. In Figures 3a and 3b, we show a glimpse of the  $^{10}\text{Be}$  concentration dependence on dust flux ( $F_d$ ) and  $^{10}\text{Be}$  production rate, given by the slope of the line in Figure 3a,  $1.45 \times 10^6$  atoms/( $\text{cm}^2$  annum).

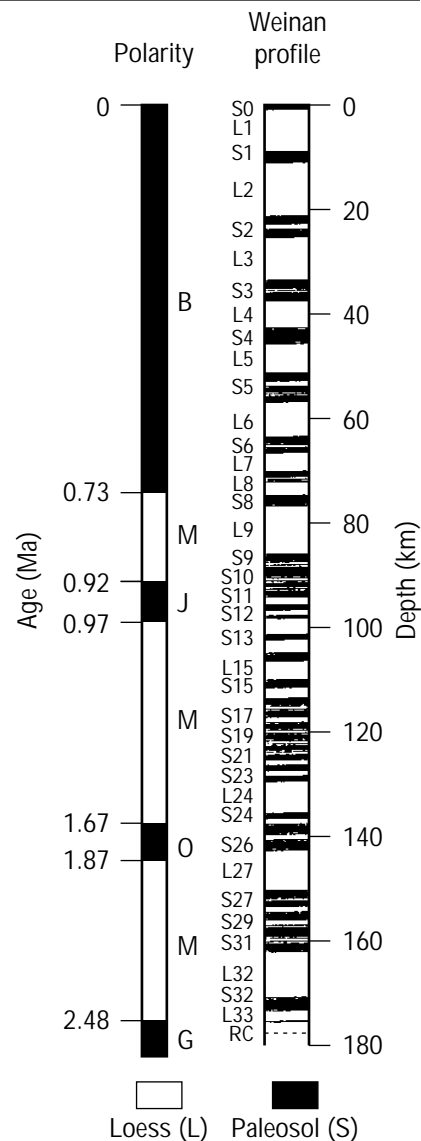


Figure 1. Magnetostratigraphy for Weinan loess and paleosol deposits.

Figure 2. Correlation of  $^{10}\text{Be}$  and Ti/Si for Weinan loess and paleosol samples.

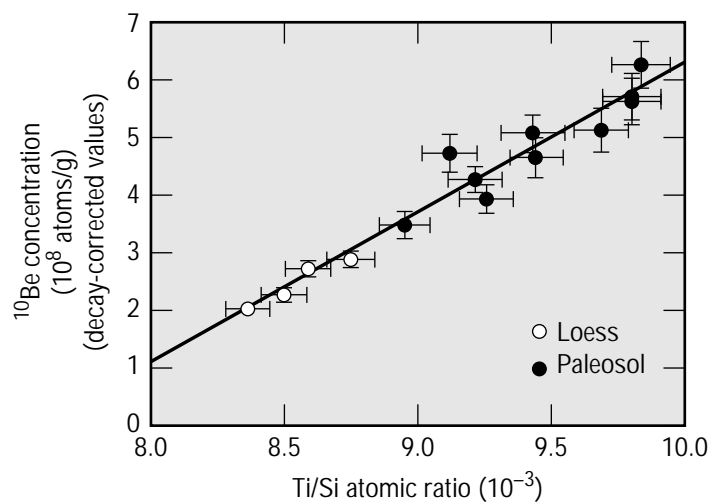
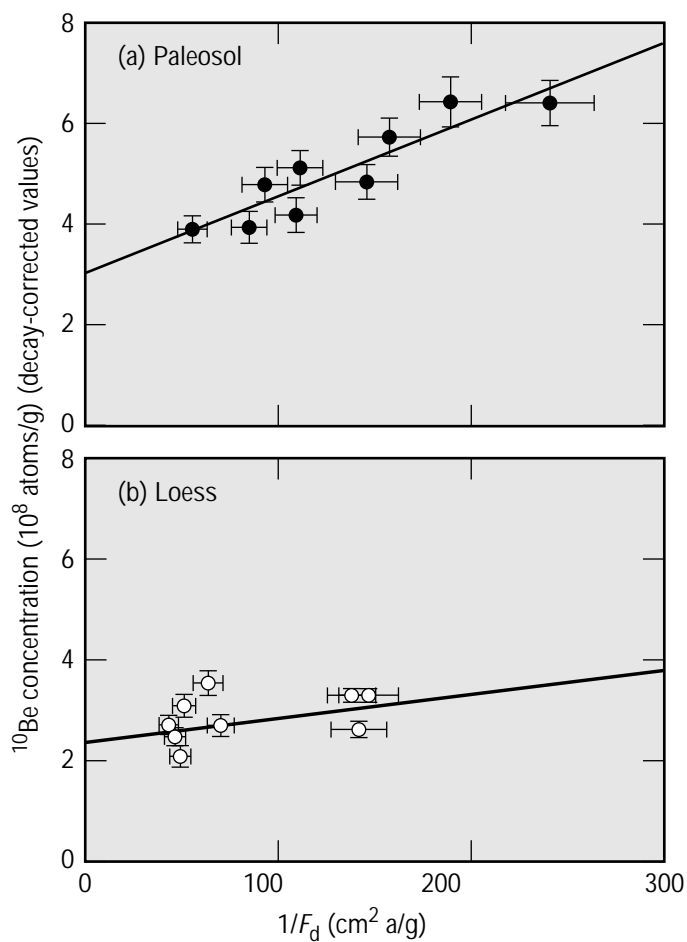


Figure 3. Dependence of  $^{10}\text{Be}$  concentration on dust flux  $F_d$  for (a) paleosol and (b) loess.



- 
1. Shen, C. D., J. Beer, T. S. Liu, H. Oeschger, G. Bonani, M. Suter, and W. Wolfli (1992), “ $^{10}\text{Be}$  in Chinese Loess,” *Earth Planet. Sci. Lett.* **109**, 169–177.
  2. Gu, Z. Y., D. Lal, C. F. You, T. S. Liu, J. Southon, M. W. Caffee, and R. C. Finkel (1993), “Evolutionary Histories of Paleosols from Chinese Loess Plateau Based on Cosmogenic  $^{10}\text{Be}$ ,” *Trans. Am. Geophys. Union* **74**(43), 210.

**References**

## Crustal Thickening in Southern Tibet over the Last 27 Ma?: The Gangdese Thrust Revisited

**Principal Investigators:** T. Mark Harrison and An Yin (UC Los Angeles)

**LLNL Collaborator:** Frederick J. Ryerson

---

### Abstract

*Structural and thermochronological investigations arising from our FY 1992 field trip to southeastern Tibet revealed the presence of a previously predicted but undocumented fault, the Gangdese thrust (GT). This thrust appears to be the earliest manifestation of crustal thickening in southern Tibet in response to the Indo-Asian collision. However, the fault was discovered during our penultimate day in the field, permitting us only to document a single outcrop. In FY 1994, we returned to the Zedong area to map this structure in detail and acquire sample suites from vertical traverses, so we can better understand the tectonothermal history of this thrust system. A 1:100,000 scale geologic map reveals that the GT is well-exposed within a window ~100 km long that was created when the dominant structural feature of the suture zone, the Renbu–Zedong thrust (RZT), bends south of the suture. A melange complex is exposed between the GT and RZT that appears to represent a continental subduction complex. Thermochronometry from two vertical traverses (0.60 and 0.92 km vertical separation) in the hanging wall immediately above the GT confirms that thrust-related cooling began at 27 Ma. Mapping suggests that the GT is exposed at significantly different structural levels along strike, which is confirmed by thermochronometry.*

---

### Objectives

The potential significance that discovery of the Gangdese thrust (GT) has to Tibetan tectonics requires that it be securely documented.<sup>1,2</sup> Our primary goals in returning to the Zedong area were to map this structure in detail and acquire sample suites from vertical traverses with which to undertake <sup>40</sup>Ar/<sup>39</sup>Ar thermochronometry. Modeling of the <sup>40</sup>Ar/<sup>39</sup>Ar results yields detailed thermal histories that can provide significant insights into the tectonothermal evolution of the thrust.

---

### Progress

Seven transects perpendicular to the east–west trend of the suture zone to the east of Zedong and one transect to the west led to a detailed 1:100,000 scale geologic map of the area. Samples collected at 100-m vertical intervals from traverses between 3.57–4.17 km and 3.60–4.52 km elevation yield mineral separates of hornblende, biotite, and K-feldspar. Analyses from the tops and bottoms of both transects have been completed. The following summary describes our current understanding of the geologic evolution of southern Tibet as a result of these investigations.

The suture zone separating Asia from the Indian subcontinent is generally marked by the Renbu–Zedong thrust (RZT), a south-dipping fault that was active between ~18 and 8 Ma. In southeastern Tibet, the fault juxtaposes Tethyan shelf rocks directly atop the Andean-type Gangdese batholith. West of Zedong, however, the RZT bends to the south, creating a 100-km-long window through which the south-directed GT is exposed. The GT is estimated to have been active between 27 to ~23 Ma with a total displacement of 50 to 80 km.

West of Lhasa, the GT juxtaposes the Late Cretaceous Xigaze Group over Tethyan sedimentary rocks. There, a lower age bound for the GT of  $18.3 \pm 0.5$  Ma

is given by crosscutting relationships. Within the Zedong window, the GT thrusts Gangdese granites and metamorphosed country rocks over Tertiary conglomerates. Directly above the GT is a mylonitic shear zone about 200 m thick, consisting of deformed granites and marbles.

The RZT thrusts Tethyan metasediments atop both the Tertiary conglomerates and a collisional melange composed of radiolarian cherts, syenite, mafic igneous rocks, gneisses, and discordant serpentinites. The interplay between erosional denudation and refrigeration of the hanging wall during thrusting produces two distinctive thermal regimes within the GT hanging wall: (1) a zone immediately above the thrust surface whose thickness is a function of the conductive time constant for the duration of thrusting, and (2) a region far above the thrust surface in which cooling is dominated by erosional denudation in response to thrust-related crustal thickening. Because thickening is diachronous, mid-crustal rocks in the southern Gangdese Shan will be uplifted and denuded prior to rocks further north.

Our  $^{40}\text{Ar}/^{39}\text{Ar}$  analyses of K-feldspars from two vertical traverses in the hanging wall of the GT reveal the onset of a rapid cooling event at 27 Ma. Sample MN-7, which is both structurally highest and closest to the thrust, transits from a temperature of  $\sim 320^\circ\text{C}$  at 27.4 Ma to  $\sim 180^\circ\text{C}$  within 1.5 million years. Then 600 m below MN-7 and at about the same distance from the thrust, ZH-3 yields a temperature history that is initially indistinguishable from MN-7 but is offset by at least  $25^\circ\text{C}$  at 26 Ma. At the same elevation, but two-thirds of a kilometer farther north, MN-1 yields a thermal history that is not significantly different from ZH-3. Immediately west of the Zedong window at Quxu and Samye, we also see evidence of rapid cooling in the Gangdese rocks beginning at 27 Ma.

We interpret this episode to reflect rapid refrigeration of the granitoids by the cold Tethyan sediments. The observed pattern of cooling in the Gangdese batholith is the opposite of what would occur if the RZT had been the dominant structural control. Within regime 2, we observe a general northward decrease in the cooling ages (from 27 Ma at the GT to  $\sim 20$  Ma 80 km north near Lhasa) that we interpret to reflect thickening-related denudation caused by propagation of the tip of the foot-wall ramp.

1. Harrison, T. M., P. Copeland, W. S. F. Kidd, and A. Yin (1992), "Raising Tibet," *Science* **255**, 1663–1670.
2. Yin, A., T. M. Harrison, F. J. Ryerson, W. Chen, W. S. F. Kidd, and P. Copeland (1994), "Tertiary Structural Evolution of the Gangdese Thrust System, Southeastern Tibet," *J. Geophys. Res.* **99**, 18,175–18,201.

## References

## Late Cenozoic Uplift History of the Tian Shan Region, Central Asia

**Principal Investigators:** An Yin and T. Mark Harrison (UC Los Angeles)

**LLNL Collaborators:** Frederick J. Ryerson, Marc W. Caffee, and Robert C. Finkel

**Student:** Peter Craig (UC Los Angeles)

---

### Abstract

*We conducted an integrated geologic and geochronological study of the Tian Shan region both in the field and in the laboratories at LLNL and UC Los Angeles. This study includes cosmic-ray dating of Quaternary terraces in the southern and northern flanks of the Tian Shan range, structural mapping to determine the magnitude of shortening, magnetostratigraphic studies to determine the initiation of thrusting, and  $^{40}\text{Ar}/^{39}\text{Ar}$  analysis to constrain the amount of erosion in the central Tian Shan. All of these factors have been considered in a quantitative model that calculates the magnitude of uplift of the present Earth's surface with respect to the sea level. The model calibrates the effect of isostasy caused by crustal thickening and erosion-induced denudation. Our preliminary results suggest that the Tian Shan range has been uplifted no more than 2.5 km with respect to the sea level and that the elevation of the Tian Shan region prior to the Cenozoic shortening is about 1.0 km. Magnetostratigraphic studies indicate that thrusting in the Tian Shan region did not start until 21 Ma, about 24 to 29 million years after the beginning of India–Asia collision.*

---

### Objectives

The surface of Earth is continuously altered under the influence of weathering, erosion, plate tectonics, and volcanic processes. Continental denudation, which depends on complex lithospheric–atmospheric interactions, is the central process of the global geologic cycling. Rates of denudation depend on a variety of factors, in particular, rock properties and their chemical composition, climate, and landform structure and elevation. A primary step in most geomorphological studies is to gain understanding of the location-specific weathering and erosional processes, the rates of which may vary over different time periods. The goal of this study is to estimate both the elevation of the Tian Shan prior to Late Cenozoic deformation and the elevation gain with respect to the sea level since the deformation. This goal was partially achieved by integrating structural and geochronological information with a quantitative model considering the isostatic effect.

---

### Progress

This study is divided into three phases: (1) field mapping, (2) laboratory analysis, and (3) data integration and interpretation. The first phase has been completed, and the second and third phases are still in progress.

Field mapping at a scale of 1:50,000 was conducted in the southern Tian Shan along the Kuche River in FY 1994. Our goal was to define the structural setting of the Quaternary terraces and magnetostratigraphic samples and to determine the magnitude of shortening in the late Cenozoic. The Quaternary terraces are well developed along the southern limb of a large anticline, which is induced by the development of a fault-bend fold system. Because the fold has been developed during the deposition of the terrace gravels, different levels of the terraces provide the opportunity to date the rate of folding once their ages are determined. Samples for



cosmogenic dating were collected, and mineral separations have been largely completed. Balanced cross sections through this region indicate that a minimum of 50% shortening has occurred in the late Cenozoic (Figure 1).

Samples were collected across the central Tian Shan for  $^{40}\text{Ar}/^{39}\text{Ar}$  analysis. Our preliminary results suggest that the maximum amount of erosion in the central Tian Shan is no more than 10 to 12 km since the beginning of the Late Cenozoic thrusting in the region, because  $^{40}\text{Ar}/^{39}\text{Ar}$  ages of K-feldspar, muscovite, and biotite have not been reset since the late Carboniferous to early Permian (Table 1). These data provide the upper bound for the late Cenozoic denudation.

Magnetostratigraphic analysis of about 150 samples from the Cenozoic strata were conducted to determine the initiation age of thrusting in the Tian Shan. Our interpreted magnetostratigraphy suggests that the sedimentation rate did not dramatically accelerate until 21 Ma and reached the maximum at about 14 Ma. In conjunction with the magnitude of shortening determined from structural mapping, an average horizontal shortening rate of  $\sim 5$  mm/year for 21 million years is estimated. This number will be compared with that determined by the cosmic-ray dating of terrace gravels to be conducted in FY 1995. By doing so, we can evaluate rates of shortening at different time intervals.

To estimate the elevation prior to shortening, we integrated the above data set and used the following equations:

$$e_1 = r_1[(\rho_m - \rho_c)/\rho_m], \quad (1)$$

$$e_2 = \{r_2 - [(T_c \times S - D)(\rho_m - \rho_c)/\rho_m]\}/(1 + S), \quad (2)$$

where:

- $e_1$  = original elevation prior to shortening.
- $r_1$  = original length of crustal root.
- $\rho_m$  = mantle density.
- $\rho_c$  = crustal density.
- $e_2$  = present elevation prior to shortening.
- $r_2$  = present length of crustal root.
- $T_c$  = continental crustal thickness when surface elevation is zero.
- $S$  = shortening strain.
- $D$  = magnitude of denudation.

As a result, we estimate that the elevation prior to shortening is about 1.0 km, and the elevation gain after shortening is 1.5 km.

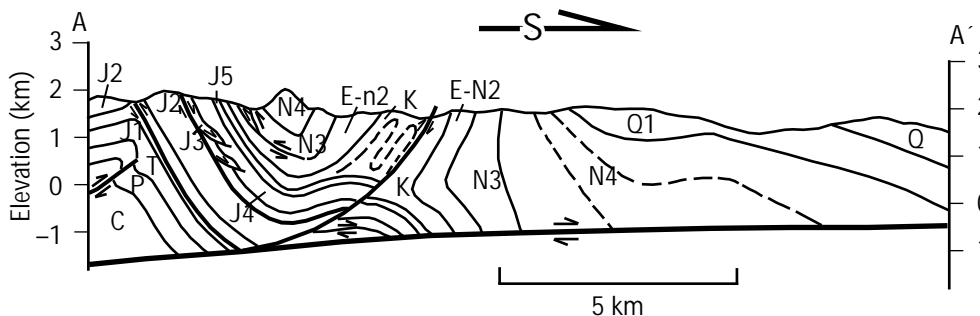


Figure 1. Geologic cross section along the Kuche River in southern Tian Shan. The samples of terrace gravels for cosmic-ray dating were collected from units Q1 and Q. These ages will determine the strain rate of folding in the later part of the late Cenozoic deformation.

*Table 1. Results of  $^{40}\text{Ar}/^{39}\text{Ar}$  analysis from central Tian Shan, which constrains the maximum amount of denudation in the Cenozoic.*

Sample No.	Mineral	Age (Ma)
N7	K-feldspar	297.3 $\pm$ 1.1
		306.4 $\pm$ 0.5
		308.3 $\pm$ 0.6
N13	Muscovite	301.8 $\pm$ 1.1
		303.0 $\pm$ 1.0
		313.7 $\pm$ 2.6
N21	Biotite	254.5 $\pm$ 4.8
		260.1 $\pm$ 3.4
N23	K-feldspar	230.8 $\pm$ 0.8
		240.4 $\pm$ 1.4
		245.9 $\pm$ 1.4
N39	K-feldspar	224.2 $\pm$ 0.8
N39	Biotite	245.1 $\pm$ 0.8
		305.3 $\pm$ 2.7
		318.1 $\pm$ 2.2
N39	Hornblende	293.2 $\pm$ 0.9
		317.3 $\pm$ 3.3
N70	K-feldspar	264.1 $\pm$ 1.5
		267.9 $\pm$ 0.8
	Biotite	295.5 $\pm$ 0.6

# An Asteroid-Meteorite Link: High-Resolution Exposure Age Chronology

**Principal Investigator:** Kurt Marti (UC San Diego)

**LLNL Collaborators:** Marc W. Caffee and Robert C. Finkel

**Other Collaborators:** Thomas Graf and Kunihiko Nishiizumi

**Student:** Yoosook Kim (UC San Diego)

## Abstract

*We discovered a substantial discrepancy in the p.m. ratio (time of fall) for a group of H5-chondrites relative to those of other ordinary chondrites. This ratio indicates distinct orbits for the immediate parent objects, a conclusion that is also supported by evidence for gas losses by solar heating. Since the H5 group belongs to the major H-parent collision ~7 million years ago, it is possible that two collisions (within 0.5 million years) occurred. This evidence raises a number of questions regarding the meteorite-asteroid link. Therefore, we determined  $^{36}\text{Cl}$ – $^{36}\text{Ar}$  exposure ages on chondritic metal to produce the quality data required to resolve this issue.*

## Objectives

Current evidence for a complex structure of the 7-Ma collisional event of the H-chondrites is based on a statistical difference in the time of fall parameters and small shifts in the distributions of exposure age peaks and retention properties of radiogenic gases of H4 and H5 chondrites. The three goals for our study of noble gases and radionuclides on bulk and metal separates of selected chondrites are to: (1) obtain new high-precision  $^{36}\text{Cl}$ – $^{36}\text{Ar}_c$  cosmic-ray exposure ages for the metal phase, so that a possible 0.5-million-year shift in exposure ages between H4 p.m. falls and H5 a.m. falls at 7 Ma can be resolved; (2) use  $^{36}\text{Cl}$  activities with new data on bulk samples, to identify meteorites with complex exposure histories and to search for different cosmic-ray flux intensities that are caused by different heliocentric distances of the two groups of chondrites; and (3) test for diffusion losses of radiogenic  $^4\text{He}$  and  $^3\text{He}_c$  in bulk and metal samples, to constrain the possibility of solar heating in H5-chondrites.

## Progress

We obtained a set of H4 and H5 chondrites (from Allegan, Limelick, Merua, Bath, Grüneberg, Ochansk) and prepared metal separates by combining magnetic and chemical separation steps. In addition, monitors and standard meteorite samples were included for calibrations. Calibrations by standards at both laboratories suggested that an overall precision of ~5% can be achieved.

Exposure ages obtained by the  $^{36}\text{Cl}$ – $^{36}\text{Ar}_c$  method depend only on production rate ratios and are therefore independent of variations in absolute production rates that are caused by different average heliocentric distances of meteoroids. In addition, the production rate ratio  $P(^{36}\text{Cl})/P(^{36}\text{Ar})$  is almost independent of energy.<sup>1</sup> Therefore, uncertainties of the exposure ages that result from shielding corrections can be minimized.

Measurements of He, Ne, and Ar as well as  $^{36}\text{Cl}$ ,  $^{10}\text{Be}$ , and  $^{26}\text{Al}$  in bulk samples of the same H-chondrites can be used to test for complex cosmic-ray exposure histories and unusual irradiation conditions (e.g., unusually large meteoroids). Exposure ages for  $^3\text{He}$ ,  $^{21}\text{Ne}$ ,  $^{38}\text{Ar}$ ,  $^{10}\text{Be}/^{21}\text{Ne}$ , and  $^{26}\text{Al}/^{21}\text{Ne}$  agree within ~10% in average-size chondrites with a one-stage exposure history.<sup>2</sup> Also,  $^{36}\text{Cl}$  produced by (n,γ) reactions provides an additional shielding indicator.

$^3\text{He}_c$  is produced directly as well as via radioactive decay of  $^3\text{H}$ . A deficit of  $^3\text{He}$  can result from a loss of either  $^3\text{H}$  or  $^3\text{He}$ . In metal,  $^3\text{H}$  is lost much faster than  $^3\text{He}$ . Because of the short half-life of  $^3\text{H}$  (~12 years), an episodic loss of only  $^3\text{H}$  will not produce a noticeable deficit of  $^3\text{He}$ . Two of the studied metals show a substantial  $^3\text{He}$  deficit, as documented by low  $^3\text{He}/^{38}\text{Ar}$  (~8) ratios. All of the measured spallation  $^{38}\text{Ar}$  concentrations except those for Allegan are in the range of 5.8 to  $6.7 \times 10^{-9} \text{ cm}^3 \text{ STP g}^{-1}$ . Bulk rock Ne exposure ages range from 6.3 to 7.7 Ma.

---

## References

1. Baros, F., and S. Regnier (1984), "Measurement of Cross Sections for  $^{22}\text{Na}$ ,  $^{20-22}\text{Ne}$ , and  $^{36,42}\text{Ar}$  in the Spallation of Mg, Al, Si, Ca, and Fe. Production Ratios of Some Cosmogenic Nuclides in Meteorites," *J. Physique* **45**, 855–861.
2. Graf, T., H. Baur, and P. Signer (1990), "A Model for the Production of Cosmogenic Nuclides in Chondrites," *Geochim. Cosmochim. Acta* **54**, 2521–2534.

### Pressure-Induced Morphology and Spatial Correlations of $\text{Ni}_3\text{X}$ Precipitates in Binary Ni-Based Alloys

**Principal Investigator:** Alan J. Ardell (UC Los Angeles)

**LLNL Collaborator:** Frederick J. Ryerson

**Postdoctoral Researcher:** Abhay Maheshwari (UC Los Angeles)

---

#### Abstract

*In this project, we aged binary Ni–Al and Ni–Ga alloys that contained 6.35 wt.% Al or 18.35% Ga, respectively, to produce dispersions of  $\gamma'$  precipitates ( $\text{Ni}_3\text{X}$ , where  $\text{X} = \text{Al}$  or  $\text{Ga}$ ). Then we re-aged the precipitates for short times at the original aging temperatures and at 9.2 GPa (92 kbar) and examined them by transmission electron microscopy to evaluate possible changes in morphology of the precipitates. The challenges of specimen preparation for the high-pressure aging experiments and for examination by transmission electron microscopy after pressurization were successfully mastered. Measurement of the ferromagnetic Curie temperatures before and after aging under pressure indicated that the solute concentrations in the matrix remained unchanged. The sizes of the coherent  $\gamma'$  precipitates also remained essentially unchanged. The applied pressure was very hydrostatic in nature, as evidenced by the absence of dislocations in the pressurized specimens.*

---

#### Objectives

There is considerable interest in the evolution of morphology and spatial distributions of  $\gamma'$  precipitates in aged Ni-based alloys. The ordered  $\gamma'$  phase has the stoichiometry  $\text{Ni}_3\text{Al}$  in Ni–Al alloys and is found in binary Ni–Si, Ni–Ga, Ni–Ge, and Ni–Ti alloys as well. The  $\gamma'$  precipitates are coherent with the saturated matrix phase, but the lattice constants of  $\gamma'$  and the matrix,  $\mathbf{a}_{\gamma'}$  and  $\mathbf{a}_m$ , respectively, differ. The resulting lattice misfit,  $\delta_0$ , produces coherency strains that profoundly influence precipitate morphology and microstructural evolution; thus,  $\delta_0 = (\mathbf{a}_{\gamma'} - \mathbf{a}_m)/\mathbf{a}_m$ .

The basis of this research is that the lattice misfit can be manipulated by imposing hydrostatic pressure. The lattice misfit at pressure  $-P$ ,  $\delta_p$ , is related to  $\delta_0$  by the equation:

$$\delta_p = (1 + \delta_0) \left[ \frac{3K_{\gamma'} - P}{3K_{\gamma'} - (1 - \Delta_K)P} \right] - 1, \quad (1)$$

where  $\Delta_K = (K_m - K_{\gamma'})/K_m$  is the hydrostatic pressure, and  $K_{\gamma'}$  and  $K_m$  are the bulk moduli of the  $\gamma'$  and matrix phases. An accurate estimate of  $\delta_p$  clearly requires knowledge of both  $K_{\gamma'}$  and  $K_m$ ; however, except for the Ni–Al solid solution, values of  $K_m$  are unknown. Nevertheless, assuming that  $\Delta_K$  for Ni–Al alloys is representative ( $\Delta_K = 0.017$ ), we can anticipate that this parameter will probably be less than 0.02 for the other alloys. Using  $\Delta_K = 0.017$  for  $\text{Ni}_3\text{Al}$  precipitates and  $\Delta_K = 0.02$  for  $\text{Ni}_3\text{Ga}$  particles, we found that imposing a hydrostatic pressure  $P$  of 10 GPa (100 kbar) reduces the lattice misfit by about 9.2% in Ni–Al alloys and by about 11% in Ni–Ga alloys. The principal objective of this investigation was to age Ni–Al and Ni–Ga alloys already containing  $\gamma'$  precipitates under hydrostatic pressure to reduce their lattice misfits, and to determine whether the magnitude of the imposed pressure was large enough to influence their morphology.

## Progress

Binary alloys of Ni–Al and Ni–Ga containing 6.35% Al and 18.35% Ga (by weight) were solution-treated at 1100°C for 1 h and quenched in refrigerated brine. The Ni–Al alloy was aged at 640°C for 69.5 h and the Ni–Ga alloy at 700°C for 2 h, to produce coherent  $\gamma'$  precipitates of an average diameter of 21.6 and 19.0 nm, respectively. Cylindrical specimens approximately 1.5 mm in diameter and 1.5 mm thick were prepared for subsequent aging under hydrostatic pressure. The Ni–Ga samples were aged at 700°C for 0.5 h at about 9.2 GPa (92 kbar), and the Ni–Al samples were aged at 640°C for 1 h at the same pressure. The samples were rapidly cooled to room temperature under pressure.

After carefully removing the pressurized samples from their ceramic casings, we cleaned their surfaces and measured the ferromagnetic Curie temperatures, to determine whether solute concentration had changed. Within experimental error, we found no changes. The small dimensions of the samples pose serious difficulties in handling and in preparing the thin-foil specimens for examination by transmission electron microscopy (TEM). For this work, we plated the small cylindrical specimens with nickel to build up the overall size. This procedure allowed us to obtain several thin slices using a thin diamond wafering blade, ultimately producing disks 3 mm in diameter (the conventional size of a TEM specimen), with the sections of the alloy embedded in the center of the disk. Then the samples were electropolished to perforation. However, since the perforated regions were not satisfactorily electron-transparent, they were subsequently ion-milled for 0.5 h. Ion milling produced some disordering of the  $\gamma'$  precipitates, degrading their contrast in the dark-field images.

Bright-field TEM images showed a relatively small density of dislocations, indicating that the applied pressure was highly hydrostatic in nature. The  $\gamma'$  precipitates were imaged in dark field using  $\{001\}$   $\gamma'$  superlattice reflections, with the thin foils tilted into  $\langle 100 \rangle$  orientation. Measurements of the particle sizes and shapes were made from high-contrast prints using a digitizer tablet. Figure 1 shows dark-field images of the precipitates in both alloys, both before and after aging under pressure. The average particle diameter in the Ni–Al alloy increased from 21.6 to 22.5 nm, whereas in the Ni–Ga alloy, the diameter remained about the same ( $\approx 9.5$  nm). Visual observation provides no indication of any change in shape.

Our preliminary results indicate considerable potential for successful experiments to observe the effect of variations in  $\delta_p$  on the morphological evolution and spatial distribution of coherent mix precipitates in binary Ni-based alloys. The applied pressure was indeed impressively hydrostatic, and the aging temperature and quench rates were controlled quite accurately. All of the major experimental difficulties that we anticipated were overcome. In hindsight, we believe a better process would be to age solution-treated, rather than previously aged, specimens under pressure and compare the shapes with those obtained from the same alloys aged at atmospheric pressure. This procedure would eliminate morphological changes brought about by either dissolution or growth of preexisting precipitates, such as would occur if the temperature in the high-pressure rig were either slightly lower or higher than the original aging temperature. Similar experiments conducted at higher pressures will produce larger changes in  $\delta_p$ , thereby facilitating data interpretation.

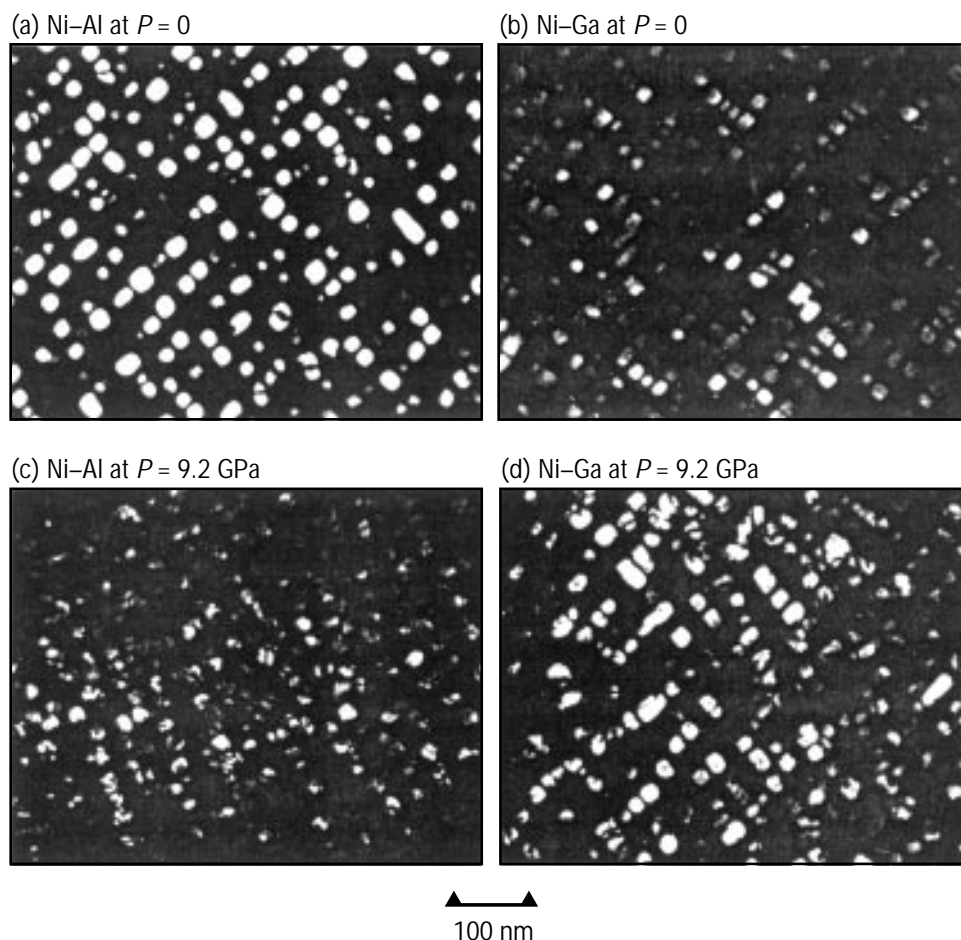


Figure 1. Dark-field TEM micrographs taken using  $\langle 100 \rangle$  superlattice reflections, showing the  $\gamma'$  precipitate dispersions in both alloys. (a) The Ni–Al alloy aged for 69.5 h at 640°C and pressure  $P = 0$ ; and (b) the Ni–Ga alloy aged for 2 h at 700°C and  $P = 0$ . (c) The Ni–Al alloy after it was re-aged for 1 h at 640°C and  $P = 9.2$  GPa (92 kbar); and (d) the Ni–Ga alloy after it was re-aged for 0.5 h at 700°C and  $P = 9.2$  GPa (92 kbar). We believe the precipitate contrast in the pressurized specimens is poorer because the radiation damage produced by ion milling reduces the long-range order in the  $\gamma'$  phase.

1. Maheshwari, A., and A. J. Ardell (1993), “Morphological Evolution of Coherent Misfitting Precipitates in Anisotropic Elastic Media,” *Phys. Rev. Lett.* **70**, 2305.

## References

## Dynamic Compaction of Alumina–Zirconia Ceramics

**Principal Investigator:** Joanna McKittrick (UC San Diego)

**LLNL Collaborator:** William J. Nellis

**Student:** John Freim (UC San Diego)

---

### Abstract

*In FY 1994, we used dynamic shock compaction to develop high-density, zirconia-toughened alumina ceramic specimens. Single-piece, crack-free specimens with densities measuring up to 80% of theoretical density for single crystals were achieved using peak shock pressures of 7 to 9 GPa. The high shock-compacted densities helped us achieve final densities measuring ~95% of the theoretical density, after sintering the compact at 1650°C for 15 min. The physical properties of the sintered compacts, including hardness, strength, and fracture toughness, were significantly better than those of conventionally processed specimens, which possessed sintered densities less than 80% of theoretical.*

---

### Objectives

The ultimate objective of our research is to fabricate hard, strong, fracture-resistant ceramic specimens. The fine-grain microstructure that accompanies the rapidly solidified alumina–zirconia ( $\text{Al}_2\text{O}_3$ – $\text{ZrO}_2$ ) eutectic makes the material a promising precursor for the manufacture of such specimens. The nanocrystalline morphology of the zirconia crystallites in this material can be exploited to incorporate the toughening mechanisms that are inherent in fine-grain zirconia ceramics. Unfortunately, the fabrication of dense specimens that retain the unique, fine-grain microstructure of this material has proven difficult. Thus, we are using dynamic shock compaction of our powder to achieve high-density specimens that can subsequently be sintered to high final densities using a short post-shock anneal.

---

### Progress

Previous research indicated that composites containing a mixture of tetragonal zirconia (t- $\text{ZrO}_2$ ) and monoclinic zirconia (m- $\text{ZrO}_2$ ) are desirable for optimizing the toughening mechanisms that operate in zirconia-toughened alumina. Our initial research produced compacts containing 90% m- $\text{ZrO}_2$  and 10% t- $\text{ZrO}_2$ . Our goal is to produce specimens containing 40% m- $\text{ZrO}_2$  and 60% t- $\text{ZrO}_2$ . A twofold approach was implemented to achieve this goal. First, we continued to optimize the rapid solidification process conditions that are used to synthesize the powder. We can synthesize material with zirconia crystallite sizes of 10 to 20 nm, dimensions at which 100% of the zirconia is stable as t- $\text{ZrO}_2$ . Second, we performed experiments to investigate the effect of yttrium oxide ( $\text{Y}_2\text{O}_3$ ) additions on the retention of t- $\text{ZrO}_2$  (which is stable only in small crystallites) as the crystallites coarsen during the post-compaction sintering cycle. Adding 1.75 mol%  $\text{Y}_2\text{O}_3$  stabilized 70% of the zirconia as t- $\text{ZrO}_2$  after a 1650°C sintering cycle.

We shock-compacted the powders in the 6.5-m-long, 20-mm-diam two-stage gas gun facility at LLNL. The powders were loaded into stainless-steel capsules and subjected to pressures from 4 to 13 GPa by impacting the capsules with projectiles traveling at approximately 1 km/s. This represents the approximate pressure range under which dense, crack-free specimens have been produced in previous research on the system. Nine shots were performed in FY 1994, and eight compacts were recovered crack free at pressures ranging from 4.3 to 9.1 GPa. The compact that was shock-compacted at the highest pressure, 12.8 GPa, was macrocracked. The tensile decompressive stresses that were generated at this pressure were too high to allow for the recovery of a crack-free compact.



The densities of the shock-compacted specimens ranged from 75 to 80% of the theoretical density of single crystals. This compares to relative densities of ~50% achieved by hydraulically cold-pressing the powder at 200 MPa. We believe the high densities of the shock-compacted specimens are a result of two mechanisms. First, the shock waves produce deagglomeration and highly efficient packing and storing of the particles. Second, the increase in bulk temperatures generated by frictional heating on the particle surfaces lowers the yield stress of the material and allows for plastic deformation to occur.

The high shock-compacted densities translated to high sintered densities as well. A specimen shock-compacted at 7.4 GPa was sintered to a density measuring 95% of the theoretical density for single crystals, compared with a relative density of ~75% for conventionally processed powder. The high density of the shock-compacted specimen was accompanied by a high microhardness, 13 GPa, and a high critical stress intensity factor, 11.4 MPa m<sup>1/2</sup>. The critical stress intensity factor was increased threefold over that of pure alumina (3.5 MPa m<sup>1/2</sup>). These results indicate that the microstructure of the material facilitates a substantial increase in toughening, as expected.

The achievement of full-density sintered specimens is the most significant obstacle remaining before we meet our ultimate goal. In ceramics, maximum strengths are typically present in fully dense material. We are investigating the effect of powder size on the shock-compacted and sintered densities. Powder size is important for determining the response to shock waves and the sinterability of a material. Preliminary results indicate that relatively large particles (20 to 40 μm) produce the highest shock-compacted densities, while smaller particles (<5 μm) produce enhanced sintering kinetics. Bimodal powder distributions are being investigated to achieve higher shock-compacted and sintered densities with the associated enhancement in material hardness and strength.

## Shock Compaction of Ferromagnetic Particles

**Principal Investigator:** M. Brian Maple (UC San Diego)

**LLNL Collaborator:** William J. Nellis

**Student:** Ricky Chau (UC San Diego)

---

### Abstract

*We have studied the magnetic properties of shock-compacted fine particles of  $\text{SmCo}_5$ . The samples were shock-compacted at LLNL using the two-stage, light-gas gun in a pressure range of 1.7 to 27 GPa (17 to 270 kbar). We used scanning electron microscopy and x-ray diffraction measurements made at UC San Diego to probe the structure of the shocked disks. Then we studied the magnetic properties using SQUID magnetometry. Between 2 and 9 GPa (20 and 90 kbar), the samples were well consolidated, and the magnetic properties remained constant. Below 2 GPa, the samples did not completely bond, and the intrinsic coercivity drops. We found that intrinsic coercivity and remnant magnetic field fall off drastically above 10 GPa.*

---

### Objective

The properties of permanent magnetic materials are a subject of great fundamental interest. The important properties are a high remnant magnetic field at zero applied field, a large magnetic reversal field, and a high magnetic energy density. These properties are controlled by the saturation magnetization, the magnetocrystalline anisotropy, and the microstructure. In particular, the microstructure in the form of grain boundaries, defects, and precipitates determines the dominant magnetization reversal mechanism. Our goal was to resolve several questions on the mechanism of magnetization reversal. By shock-consolidating fine particles of  $\text{SmCo}_5$ , we can control the microstructure using dynamic pressures. We hope to answer fundamental questions concerning magnetization reversal and develop superior magnetic properties.

---

### Progress

We investigated the magnetic and structural properties of shock-consolidated microcrystalline particles of  $\text{SmCo}_5$ . The  $\text{SmCo}_5$  particles were mechanically reduced from commercial powder. The particles have a size distribution from 1 to 10  $\mu\text{m}$  as determined from scanning electron microscopy (SEM). The size of the particles, however, is larger than the nanometer size needed for each particle to be a single domain. Therefore, we aligned the particles in a static 1-T field and compacted them with a hydraulic press. All samples were aligned except one sample shocked at 4.1 GPa (41 kbar), which was used for comparison. We loaded each pressed disk into either copper or stainless-steel capsules. Shock compaction was performed at LLNL using the 7-m, two-stage, light-gas gun at pressures from 1.7 to 27 GPa (17 to 270 kbar).

Shock compaction at pressures less than 2 GPa (20 kbar) failed to completely consolidate the particles. The edges of these samples disintegrate into loose powder. Between 2 and 10 GPa (20 and 100 kbar), the shock compaction produced a well-consolidated disk. We estimated an average density for these samples by measuring the volume and the mass. The densities were nominally 80 to 85% of the bulk value of 8.3 g/cm<sup>3</sup>. Samples shocked at pressures above 6 GPa (60 kbar) show signs of stress developing. Above 10 GPa (100 kbar), significant structural changes are visible. The samples develop a circular fracture near the rim as a result of a radial pressure release. The center of the sample exhibits a fault pattern that results in lower particle cohesion. Also, melting occurs at the edges of the sample. Between 18 and 27 GPa (180 and 270 kbar), the shock release tears the sample apart, leaving only small pieces.

We also examined the microstructure of the shocked disks using x-ray diffraction (XRD). XRD patterns showed no change in the microcrystalline structure for all samples except at 27 GPa (270 kbar). We found no evidence that  $\text{SmCo}_5$  was decomposing into the adjacent  $\text{Sm}_2\text{Co}_7$  or  $\text{Sm}_2\text{Co}_{17}$  phases. In these samples, we saw no significant change in the lattice parameters. The 27-GPa (270-kbar) sample showed evidence for significant phase decomposition into the adjacent phases.

Magnetic measurements were made with a superconducting quantum interference device magnetometer at UC San Diego. The remnant field  $B_r$  (the residual magnetization when the applied field  $H$  is zero) and the intrinsic coercivity  $H_{ci}$  (the applied field needed to reduce  $B_r$  to zero) were extracted from hysteresis loop measurements (Figure 1). The magnetic behavior of the samples versus pressure is divided into three regimes. Samples shocked at the lowest pressures (1.7 to 2.0 GPa) do not have an optimal coercive force but do have a high remnant field. The coercive force is lower at these pressures because many of the particles are loose and can rotate freely with the applied field. In a pressure range of 3 to 10 GPa (30 to 100 kbar), the magnetic properties are nearly constant. The intrinsic coercivity has its maximum in this pressure range but begins to fall off above 6 GPa (60 kbar), as structural faults begin to develop. The remnant field remains at a constant level up to 9.5 GPa (95 kbar). Above 10 GPa (100 kbar), both the remnant field and the intrinsic coercivity drop off rapidly with increasing shock pressure. The decrease in magnetic properties correlates with the structural changes (structural faults and partial melting) in this pressure region.

The pressure dependence of the magnetic properties differs from that of shock-compacted bulk samples of  $\text{SmCo}_5$ . For bulk  $\text{SmCo}_5$ , the key magnetic properties exhibit a dramatic falloff for even moderate pressures. For our samples, most of the shock energy is absorbed in bonding the individual grains together rather than inducing shock defects. This effect accounts for the nominally high values of the magnetic properties in the range of 3 to 10 GPa (30 to 100 kbar) for our samples.

Many key issues remain. We have shown that shock consolidation is a useful technique in bonding fine particles into a bulk without damaging the important magnetic properties. The unaligned sample used for comparison shows that our alignment is far from optimal. Because our particles are not single domains, we still have domain reversal in individual grains. Domain reversal prevents optimal alignment and lowers the magnetic properties. By reducing the size of the particles to single domains in future experiments, we hope to significantly improve the magnetic properties.

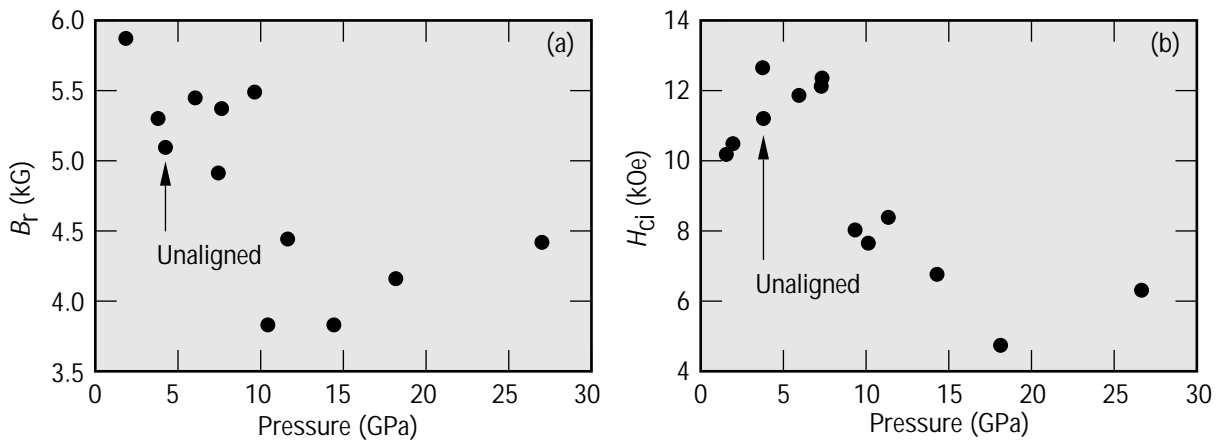


Figure 1. Dependence of (a) the remnant field and (b) the intrinsic coercivity on shock pressure. The unaligned sample is used for comparison.

## Semiconductors under High Pressure

**Principal Investigator:** Robert N. Shelton (UC Davis)

**LLNL Collaborator:** Harry B. Radousky

**Student:** Stephen H. Irons (UC Davis)

---

### Abstract

*GaAs thin films and GaAs/AlGaAs superlattices form the basis for many semiconductor devices. By applying pressure, we can vary the bandgap, band offsets, and strain energy in a single sample and thus simulate the effects of strain and chemical doping, which are usually obtained by growing a large number of expensive samples. Femtosecond spectroscopy, coupled with the application of hydrostatic pressure, can be used to selectively probe the various scattering mechanisms in GaAs materials.*

---

### Objectives

Femtosecond transmission spectroscopy can be used to understand the carrier dynamics in low-temperature-grown GaAs materials. By using a Ti-sapphire laser, operating near 825 nm, we can make measurements at the energy gap of GaAs, eliminating many of the higher-energy scattering mechanisms that complicated the usual analyses. A sapphire-anvil pressure cell can be used to apply hydrostatic pressure to low-temperature-grown GaAs films. By applying pressure, we can then vary the energy gap and study the scattering mechanism. These results can be compared with standard grown GaAs films.

---

### Progress

A sapphire-anvil pressure cell has been constructed at UC Davis for studying semiconductors. The sapphire cell is constructed from type 316 stainless steel. The small overall dimensions of the cell (2.5 cm in diameter and 2.5 cm high) and clear optical path through the center make it ideal for use in optical studies. The sapphire spheres were polished with two parallel flats (2 to 3 mm in diameter) perpendicular to the *c* axis. The cell is being tested to determine pressure uniformity inside the sample volume.

## Experimental Investigation of Shock Effects in Porous Meteoritic and Terrestrial Materials

**Principal Investigator:** John T. Wasson (UC Los Angeles)

**LLNL Collaborator:** William J. Nellis

### Abstract

*We have conducted a series of shock-loading experiments to investigate the role of variable target characteristics, especially porosity, in impact metamorphism. Experimental targets included a variety of terrestrial and asteroidal materials, plus synthetic analogs. For a series of experiments designed to constrain the role of carbon in the genesis of the ureilite meteorites, petrographic follow-up work is still at an early stage. A series of experiments involving chondrite simulants yielded little evidence of the silicate darkening (dispersion of tiny grains of magnetite and pentlandite) characteristic of the metamorphosed CK chondrites. The terrestrial materials were studied to constrain the origin of tektites. Results indicate that at a given shock pressure, systematically higher fractions of melt form if the target is loosely compacted porous loess, in comparison to compositionally and mineralogically similar, but less porous, siltstone.*

### Objectives

All of the terrestrial planets and large asteroids have been profoundly affected by impact-induced shock metamorphism, especially early in the solar system's history. Meteorites, which are collisionally dispersed fragments of asteroids, typically have been shocked to pressures of about 10 GPa and in many cases to >40 GPa.<sup>1</sup> Our experiments were designed to constrain how shock effects may vary as a function of the preshock physical state, especially the porosity, as well as the mineralogy, petrology and chemistry of the materials. The experiments have rather general application, but three specific issues were addressed: (1) The origin of tektites. Tektites are homogeneous masses of pure SiO<sub>2</sub>-rich impact glass, typically several centimeters in size, devoid of crystallites, and with very low contents of relict minerals and H<sub>2</sub>O. They are concentrated in only four roughly continent-sized "strewn-fields." (2) The shock and thermal histories of the CK group carbonaceous chondrites. (3) The potentially explosive role of carbon (graphite) during high-degree shock metamorphism of carbonaceous meteorites, especially ureilites. Ureilites are an abundant but enigmatic (e.g., carbon-rich yet igneously differentiated) type of meteorite, probably formed by partial melting of carbonaceous chondritic precursor materials.

Experimental targets included pieces of the Allende CV3 carbonaceous chondrite, synthetic analogs of chondrites and of ureilites, and for the tektites study, terrestrial materials. The synthetic analogs were prepared by mixing powders (sieved to a realistic grain-size distribution) of magnesian olivine, hypersthene, chromite, and graphite. Also, in some ureilite simulations, powdered Allende was mixed with powdered graphite. Most previous shock-loading experiments investigated either pure minerals, igneous rocks, or lunar regolith. Only a few studies (most recently Kitamura et al.<sup>2</sup>) focused on chondritic meteorites, which have peculiar mineralogy and moderately high porosity. Carbonaceous meteorites had been almost completely overlooked.

In our experiments, we used a two-stage, light-gas gun at LLNL to accelerate projectiles to speeds of 0.8 to 4 km/s and impact them into fixed targets, yielding shock pressures up to 43 GPa. Projectiles were made from Lexan, copper, or aluminum. Targets were 11-mm-diam disks, with thicknesses of 0.4 to 0.8 mm for

powdery materials or 1.0 to 1.4 mm for rocks. The samples were encapsulated in either aluminum, for a good impedance match to our typical powdery (~30% porosity) targets, or stainless steel, for experiments involving high risk of capsule failure (i.e., all experiments involving graphite-rich ureilite simulant powders, plus two others involving shock pressures  $\gg$  30 GPa). For six of the ureilite-simulant experiments, we fashioned containers with two narrow (790- $\mu$ m-diam) holes through the backup plugs, to allow escape of CO/CO<sub>2</sub> gases generated by redox reactions in response to the shock (cf., Kikuchi et al.<sup>3</sup>). In one early experiment involving solid Allende meteorite encapsulated in Al, loading to 43 GPa caused a gross rupture of the capsule, with complete disintegration of the sample. However, Al capsules survived in suitable condition for analysis in experiments when shocked as high as 40 GPa. Thin sections of the recovered samples were studied at UC Los Angeles, using mainly Zeiss Universal (petrographic) and SV8 (binocular) microscopes, and a CAMEBAX electron microprobe.

---

## Progress

A total of 20 experiments have been conducted. Petrographic investigation of the resultant thin sections is not yet complete, particularly for the ureilite-related work. Petrographic study is virtually complete for the set of experiments that addressed the origin of tektites. Compositionally, tektites are uniformly close to shales, so the source craters must be in continental crust. Our experiments used two different target materials, selected as likely candidates for the precursors of tektites: a loosely compacted (~35% porosity) Chinese loess, and a Colorado siltstone that is similar in mineralogy, composition, and grain size, but has far lower porosity. Results indicate that systematically higher proportions of impact melt form, at any given shock level, from the porous loess in comparison to the less porous siltstone. These results tend to support the hypothesis that areas with uncommonly dry and porous surface materials are far more likely than ordinary continental surfaces to spawn tektites.<sup>4</sup> During shock alteration, dry porosity favors production of homogeneous, fully vitric masses, because more of the impact energy is partitioned into shock and post-shock heating. Where the target is porous but water-rich, vaporization of the water absorbs much of the available heat and engenders high pore pressures, thus limiting the shock-compression of the target.

Unlike all other carbonaceous chondrite groups, the CK carbonaceous chondrites are thermally metamorphosed (petrologic types 4–6) and show extensive silicate darkening caused by the dispersion of tiny grains of magnetite and pentlandite in silicate interiors. The curvilinear trails formed by these opaque phases within the silicates is analogous to similar trails of metallic Fe–Ni and troilite in ordinary chondrite silicates. Rubin suggested that the silicate darkening in CK chondrites was due to shock melting and mobilization of magnetite and pentlandite.<sup>5</sup> To constrain this shock-dispersal hypothesis, we subjected mixtures of olivine and chromite (as an opaque oxide) to shock pressures of 7.9 to 29.4 GPa. Shock experiments using pieces of Allende were also germane to this problem.

Preliminary petrographic studies reveal little evidence of silicate darkening. Apart from brecciation and, in the highest-pressure experiment, formation of a small proportion of shock melt, the chromite grains seem undisturbed. Although this result does not support the shock-dispersal hypothesis, it does not necessarily conflict with it. Conceivably, CK chondrites were shocked to pressures even higher than 29.4 GPa. The magnetite-pentlandite association in CK chondrites is not precisely mimicked by the chromite (which has a higher shock impedance) of our experiments. The most likely alternative, precipitation of magnetite as a result of highly oxidizing conditions during genesis of these chondrites, is difficult to recon-

cile with the fact that highly oxidized ordinary chondrites (e.g., the LL5 Parambu, with Fa32 olivine) contain trolite and pentlandite, yet do not feature magnetite or silicate darkening. Moreover, the pentlandite dispersal is clearly not explicable by such a model.

1. Stöffler, D., K. Keil, and E. R. D. Scott (1991), "Shock Metamorphism of Ordinary Chondrites," *Geochim. Cosmochim. Acta* **55**, 3845–3867.
2. Kitamura, M., A. Tsuchiyama, S. Watanabe, Y. Syono, and K. Fukuoka (1992), "Shock Recovery Experiments on Chondritic Materials," in *High Pressure Research: Application to Earth and Planetary Sciences*, Y. Syono and M. H. Manghnani, Eds., pp. 333–340.
3. Kikuchi, M., Y. Syono, N. Kobayashi, T. Oku, E. Aoyagi, K. Hiraga, T. Atou, A. Tokiwa, and K. Fukuoka (1990), "Shock-Induced Superconductivity of  $Tl_2Ba_2CuO_6$ ," *Appl. Phys. Lett.* **57**, 813–815.
4. Wasson, J. T., and W. A. Heins (1992), "Tektites and Climate," *J. Geophys. Res. (Planets)* **98**, 3043–3052.
5. Rubin, A. E. (1992), "A Shock-Metamorphic Model for Silicate Darkening and Compositionally Variable Plagioclase in CK and Ordinary Chondrites," *Geochim. Cosmochim. Acta* **56**, 1705–1714.

## References

## The Development of Preferred Orientation in Ice Investigated by Neutron Diffraction

**Principal Investigator:** Hans-Rudolph Wenk (UC Berkeley)

**LLNL Collaborator:** William B. Durham

**Student:** Kristin Bennett (UC Berkeley)

---

### Abstract

*Our goal in this project was to study the mechanical properties, texture, and microstructure of high-pressure, low-temperature polycrystalline ice as it exists on satellites of the outer planets. High-pressure experiments were performed with a gas apparatus and a light-gas shock gun at LLNL. Samples were subsequently analyzed by neutron diffraction at the National Institute of Standards and Technology and the Los Alamos Neutron Scattering Center (LANSCE).*

---

### Objectives

The three states of matter—solids, liquids, and gases—all flow within the Earth, yet only the solid form retains a substantial memory of the strain history over geologic time scales. The strain history has a direct effect on the flow behavior and sometimes on phase changes of solid materials. Texture (preferred crystallographic orientation) is a means to document the strain history of a solid. For this reason, the strain evolution of crystalline silicates, main constituents of the Earth, is routinely studied by texture analysis in order to understand anisotropy and macroscopic deformations in the Earth. Other bodies in the solar system display anisotropic features and macroscopic deformations that are comparable to those of the Earth. A unique collection of icy satellites belonging to the outer planets display mappable terrains, tectonic activity, and plastic deformation as found on Earth. However, the satellites consist mainly of water ice or ice–rock mixtures. Therefore, understanding macroscopic deformations on these icy bodies or their geophysical evolutions requires knowledge of the strain evolution of crystalline water ice at high pressure and low temperature.

At conditions of the outer solar system, water ice behaves much like silicates during plastic deformation. Mechanical data for ice I and the high-pressure ice polymorphs are extensive. However, quantitative analysis of their texture during deformation or phase change does not exist, mainly because there has been no convenient way to measure texture at such low temperatures ( $<245$  K). Some of the experimental ice polymorphs require texture measurement at temperatures as low as 77 K to retain their phase and structure after the tests.

This work documents a new low-temperature neutron diffraction technique that was developed to measure the texture of polycrystalline materials at 77 K. High-pressure, low-temperature deformation and phase-change experiments were performed on polycrystalline ice to create texture. The fabricated textures were then measured by neutron diffraction, and the measured pole figures were used to calculate orientation distribution functions for the samples. Finally, microstructures in the samples were investigated using low-temperature scanning electron microscopy, optical microscopy, and replication techniques.



In FY 1994, we studied the mechanics, texture, and microstructure of ice I, ice I with dispersed particulates, ice I with ice II, ice II, and the phase of shocked-loaded ice. All of our samples were deuterium oxide ( $D_2O$ ) ice because the incoherent scattering of hydrogen during neutron diffraction is too high for texture analysis. We present here the results of the texture measurements because they are the first application of the new low-temperature diffraction technique.

We used a high-pressure gas apparatus to transform and deform polycrystalline ice specimens in axial compression experiments. Then the texture that developed from the transformations and deformation was determined quantitatively by neutron diffraction at 77 K, using a four-circle goniometer adapted with a cryogenic core. Microstructures were investigated by optical microscopy, or a low-temperature scanning electron microscope (LTSEM), and with replication techniques.

In the first study, the effect of hard dispersed particulates on the flow of an ice matrix at high pressures and low temperatures was investigated using polycrystalline aggregates of  $D_2O$  ice mixed with 0 to 40 vol%  $Al_2O_3$  particulates of two sizes:  $\sim 1.0$   $\mu m$  and 12  $\mu m$ . Test specimens were axially compressed using a triaxial deformation apparatus at strain rates of  $10^4$  and  $10^{-5} s^{-1}$  at confining pressures of 50 MPa and temperatures of 180 to 256 K, to achieve approximately 25 to 35% shortening. Adding rigid particulates to the ice matrix increased the yield strength of the aggregate for both the coarse- or fine-grained inclusions. Textures showed strong preferred orientations with axes parallel to the direction of compression. Texture maxima decreased with increasing volume of rigid inclusions. Major-to-minor axis ratios of ice grains in the deformed specimens decreased with increasing alumina content when coarse-grained particulates were added to the matrix. When fine-grained particulates were added to the specimen, ice grains were nearly equant after the deformation experiments and showed evidence of recovery.

In the second study, the development of preferred crystallographic orientation in the ice I  $\rightarrow$  II transformation and in the plastic flow of ice II was investigated in polycrystalline  $D_2O$  ice specimens. For two  $D_2O$  ice test specimens, approximately 50% of the ice I to ice II transformation took place using nonhydrostatic pressure. Measurements of these specimens revealed a depletion of (0112) poles and a concentration of (1120) poles parallel to compression. Three test specimens were transformed 100% to ice II using either hydrostatic or nonhydrostatic pressure. Then they were axially compressed at constant strain rates to various strains. In these specimens, pole figures showed strong preferred orientations of ice II (1120) and (1010) poles parallel to the compression. In an unusual experiment, one sample of pure ice II shortened 48% at 195 K developed a strong preferred orientation that resembled a hexagonal single-crystal texture with (0001) poles aligned in the compression direction. Models based on the viscoplastic self-consistent polycrystal plasticity theory were used to predict the preferred orientations observed in the experiments. The best agreement with the experimental data was obtained when using (1010)[0001] as the predominant slip system.

A third study used the new low-temperature neutron diffraction setup to identify phase and structure of polycrystalline  $D_2O$  ice I under shock load. Five synthetic,  $D_2O$  ice specimens with uniform grain size were shock-loaded at temperatures near 100 K using the two-stage, light-gas gun fitted with a cryogenic tank and achieving peaks of 0.6, 1.2, 1.5, 2.4, and 5.0 GPa. The phase of the metastable shock-loaded specimens was subsequently identified at 100 K in a neutron powder diffractometer as crystalline ice I. Optical microscopy of the shocked ice surfaces revealed that the grain retained its original structure and had not recrystallized.

The findings from this work have many geological and geophysical implications for the icy bodies of the outer solar system, but the effects were not studied quantitatively in this work.

## Melting of Ni and Pt at Ultrahigh Pressure: A Unique Interlaboratory Comparison

**Principal Investigator:** Raymond Jeanloz (UC Berkeley)

**LLNL Collaborator:** William J. Nellis

**Student:** Abby Kavner (UC Berkeley)

---

### Abstract

*Unique new calibration experiments are enhancing the use of the laser-heated diamond-anvil cell for quantitative experiments at ultrahigh pressure and temperatures. High-temperature thermocouples are being developed as an internal standard for temperature measurements within the laser-heated diamond cell.*

---

### Objectives

Two steps are important preconditions for establishing quantitative reliability of temperature measurement in the diamond-anvil cell: careful intralaboratory calibrations and extensive interlaboratory cross checks. These steps are being performed in tandem at the UC Berkeley and LLNL high-pressure laboratories. With these calibrations and cross checks defining the standard of quantitative temperature determination at ultrahigh pressures, future progress in this field is expected to be rapid.

---

### Progress

The measurements have so far centered on platinum because it is already established as a high-pressure standard. Also, ab initio calculations of the thermal equation of state of platinum have been performed, and platinum-based thermocouples can be used as part of the temperature measurement calibration. Once the calibrations have been established and are well understood, we will focus on determining melting temperatures at high pressures.

As a first step in calibration, we tested the accuracy of our charge-coupled device– (CCD-) based temperature measurements by measuring the room-pressure melting temperature of resistively heated metal filaments. Using spectroradiometry, we measured the temperature of the filaments just before they melted and broke, yielding a lower-bound estimate of the melting temperature for the metal filaments. For platinum, the highest temperature measured before the filament broke is 2060 K, which within the experiment precision of  $\pm 20$  K, is exactly at the actual platinum melting point of 2045 K. Measurements were also obtained for iron, zirconium, molybdenum, and tungsten filaments.

The lack of internal fixed-temperature calibrations has added to the difficulty of interpreting temperatures that are determined using spectroradiometry. To address this difficulty, we performed a set of thermocouple experiments. High-temperature thermocouples, both platinum–rhodium and tungsten–rhenium, were laser-heated in an argon atmosphere at room pressure using the Nd:YAG laser in continuous-wave mode. The temperature was measured simultaneously using both spectroradiometry and voltage measurements of the Seebeck effect. Average temperatures of the hot spot, determined by spectroradiometry, agree with the thermocouple values to within 100 to 300 K over the temperature range of 1200 to 2300 K.

The final experimental step in the calibration, still in progress, is to repeat the thermocouple experiments, this time with the thermocouples mounted under pressure in the diamond-anvil cell. This step is important for two reasons. First, it will significantly extend the pressure range of the thermocouples used for temperature

measurement at ultrahigh pressures and will allow us to evaluate the effectiveness of using them for such measurements. Second, combined with temperature gradient and thermocouple response modeling, it is a step toward addressing measurement of the large thermal gradients encountered in laser-heating at high pressures.

This experimental work will continue in FY 1995. Using special nonconducting epoxy gaskets, we have succeeded in loading the thermocouple into the diamond-anvil cell, allowing us to perform the thermocouple calibration experiments under high pressure.

### Atmospheric Characterization for Adaptive Optics

**Principal Investigator:** Stanley M. Flatté (UC Santa Cruz)

**LLNL Collaborator:** Claire E. Max

**Student:** L. William Bradford (UC Santa Cruz)

---

#### Abstract

*In FY 1994, we continued investigations into the nature of the power spectrum of optical phase fluctuations caused by refractive-index variations arising from atmospheric turbulence. This work is directed at understanding how atmospheric turbulence will affect the performance of large optical telescopes and arrays of telescopes. During FY 1994, we concentrated on analyzing the data taken by the LLNL Laser Guide Star Project team at the Lick Observatory. Most data were gathered with the 1-m-diam Nickel telescope and some with the 3-m Shane telescope. Analysis of data taken with the LLNL speckle camera has given some indication of the range of values for the temporal, spatial, and angular coherence scales to be expected at the Mount Hamilton site.*

---

#### Objectives

The objective of this investigation has been to analyze the effect of atmospheric turbulence on optical propagation at an astronomical observatory. By obtaining values for the principal parameters used to characterize those effects, we can place some restrictions on the models we use to characterize the atmosphere. Our previous work has lacked some of the information needed to characterize the atmosphere, leading us to use a variety of plausible atmospheric models, some based on real, single-instance measurements and some on general statistical models. We were able to draw some general conclusions, as documented in our previous reports and various conference proceedings.<sup>1-3</sup>

Those models can only give us broad limits on possible behavior. If we are to be able to determine whether there is any significant deviation from the standard Kolmogorov model of atmospheric turbulence,<sup>4</sup> we require more information about the structure of the atmosphere. It is not feasible to sample the atmosphere in a continuous manner over the required volumes. However, measuring coherence scales associated with the propagation of starlight through the atmosphere does give us the path-integrated values of the atmospheric structure constant  $C_n^2$  (which is a measure of the strength of refractive index fluctuations) and its products with wind velocity and altitude. These yield the Fried coherence length  $r_0$ , the coherence time  $\tau_0$ , and the isoplanatic angle  $\theta_0$ .

The Fried coherence length is the largest diameter over which phase errors introduced by the atmosphere give an image spot size less than or equal to that resulting from diffraction by an aperture of that diameter. The isoplanatic angle is essentially the angle away from some reference object at which cross correlation between two signals (or the autocorrelation for one signal) falls to  $e^{-1}$ , the zero separation angle value. The coherence time is the time interval over which the autocorrelation of a signal will fall to  $e^{-1}$  of the zero time value.

To test measurements against the Kolmogorov model, it is best to have measurements taken at two or more wavelengths, since power law models, such as the Kolmogorov model or the random walk model, will have results that scale with a

power of the wavelength. For the Kolmogorov model,  $r_0$ ,  $\theta_0$ , and  $\tau_0$  will scale as  $(\lambda_2/\lambda_1)^{1/2}$ , when measurements made at wavelength  $\lambda_2$  are compared with measurements made at  $\lambda_1$ . For the random walk model,  $r_0$ ,  $\theta_0$ , and  $\tau_0$  will scale as  $(\lambda_2/\lambda_1)^2$ . Ideally, these measurements will be made simultaneously, but this goal is not realized in the experiments performed so far. Instead, a sequence of measurements is made at one wavelength and then repeated at other wavelengths. If the atmosphere remains reasonably stationary, then scaling is possible. Of course, stationarity is a statistical concept, so even if the atmosphere is stationary, there is little to guarantee that any given set of measurements will be related by ideal scaling. Therefore, it can be difficult to ascertain if differences in measurements are caused by changes in the atmosphere or non-Kolmogorov behavior. One objective of our analysis has been to obtain some idea of how much variation is present in the data and how much data might be needed to facilitate the analysis.

The measurements made at the Lick Observatory consist of short-exposure time images taken to create stellar speckle interferograms and also of wavefront sensor measurements taken with the LLNL adaptive optics instruments. The wavefront sensor measurements can be divided into the following categories: no tip/tilt correction, open loop measurements of single and binary stars, open loop with tip/tilt correction on a natural guide star, and closed loop and tip/tilt correction on a natural guide star. Only the speckle measurements are reported here, but a future paper will discuss both sets of measurements in more detail. Some of the data have already been reported at a conference on adaptive optics.<sup>5</sup>

This information is sufficient to calculate a few parameters relevant to optical propagation through the turbulent atmosphere. These include the spatial coherence size  $r_0$ , the temporal coherence time  $\tau_0$ , and the angular coherence size  $\theta_0$ . These parameters should, in principle, be sufficient to infer a crude model of the structure of atmospheric turbulence for calculations involving integrals over the optical path through the turbulence. Such models cannot represent the fine structure known to exist in the atmosphere.

Data were taken at the Lick Observatory from February 1993 through September 1994. Of more than 30 nights with any speckle data collection at all, only about 10 have measurements that would allow some determination of all three parameters ( $r_0$ ,  $\theta_0$ , and  $\tau_0$ ). Of those, scaling of the wavelength is possible on all three parameters on only two occasions. However, wavelength scaling on at least one of the parameters is possible (in principle) on sixteen occasions. For two parameters, nine nights are possible. Analysis of the potential for information from the wavefront sensor is not complete at this time.

Even with all of these possibilities, some of the data are less useful than other data. One of the principal problems with many of the experiments is that data were taken (sometimes of necessity) at exposure times of more than 50 ms. These longer exposure times are a problem for measurements of the isoplanatic angle because they tend to wash out high-spatial-frequency information, leaving only some of the lower-spatial-frequency information. The latter is more spatially invariant; therefore, measured signals from two sources are more spatially correlated than they would be if high-spatial-frequency information is included. Initial analysis indicated larger isoplanatic angles than expected on the basis of others' experience and standard models. Initial measurements often indicated isoplanatic angles of more than 10 arcsec, far larger than the 2 to 4 arcsec typical of other sites.

Measurements at shorter exposure times were then made, which led to values more in accord with expectations, with values ranging from 3 to 5 arcsec for exposures of a few milliseconds. In some cases, an attempt has been made to correct the

## Progress

long exposure data. This was done by plotting values of cross correlation versus exposure time for some of the datasets. Unfortunately, no single set of measurements was attempted over the entire range from 1 to 100 ms, and the data from several experiments have some scatter. Nevertheless, it looked as if a measurement made at 100 ms, which yielded a cross correlation of 0.85, might correspond to 0.50 at 1 ms (all very roughly). For the datasets used, which had binary components separated by 3 to 4.4 arcsec, this seemed to give  $\theta_0$  values more in line with expectations.

The same correction was applied to a dataset where the separation of the binaries is almost twice as large and only exposure times of 100 ms had been made. The results still give  $\theta_0$  values much larger than expected. It appears that what we have actually observed is that at 100 ms, the cross correlations are relatively independent of binary separation (at least for separations between 4 and 8 arcsec). This may be a hint of some sort of outer scale, but the interpretation is uncertain.

The longer exposure times are also not useful for estimates of the coherence time since measurements at other sites, and these data, show that the coherence time is often less than 10 ms. Still, several datasets were taken with appropriately short exposure times. The results indicate that at wavelengths of 550 nm, the coherence time is about 5 to 10 ms. The datasets do indicate that the coherence time is longer as the wavelength increases, but quantitative comparisons with the data analyzed so far seem inconclusive.

Calculations of the Fried coherence length were made by calculating the average value of the square of the modulation transfer function for a star image. This was then used to fit a function of the parameter  $r_0$ , yielding a best fit value for  $r_0$ .<sup>6</sup> The particular function to be fitted assumes a Kolmogorov model. Fits to the data using a non-Kolmogorov model are planned.

Because the values for  $r_0$  are obtained by fitting to a function, we must be careful in reporting the values obtained. If the fit is not particularly good, the value reported may be misleading. For example, we have some values reported at longer wavelengths that seem to indicate quite good seeing, but for which the fit is not particularly good. This may indicate that performance gains at longer wavelengths are better than expected from Kolmogorov, as suggested by Bester et al.<sup>7</sup> Fitting with non-Kolmogorov models will provide some guidance.

In Figure 1, we show some data taken at the Nickel telescope on September 29, 1993. Triangles represent the best-fit values of  $r_0$  computed from the fitting function. The circles represent the values of  $r_0$  obtained if the wavelength scaling rule is applied to scale to a wavelength of 500 nm. Note that about 20 min into the data, the scaled values increase. Is this increase caused by an improvement in the seeing, or is it somehow related to a non-Kolmogorov effect? Certainly, the former is possible and very likely. As mentioned, the atmosphere may not appear to be stationary. Evidence for this is shown in Figure 2, in which data from March 11, 1993, are plotted. In Figure 2, all measurements were at a single wavelength, so variability in values represents variability in the atmospheric (and possibly dome) conditions. Early in the night, the data do not fluctuate as much as later in the evening. This fact indicates that nonstationary behavior is possible. One problem with the analysis is that there are relatively few extended sets of measurements.

With additional data and analysis, particularly analysis of the wavefront sensor data, we hope to get better insight into the question of model variations versus non-stationary atmospheric effects.

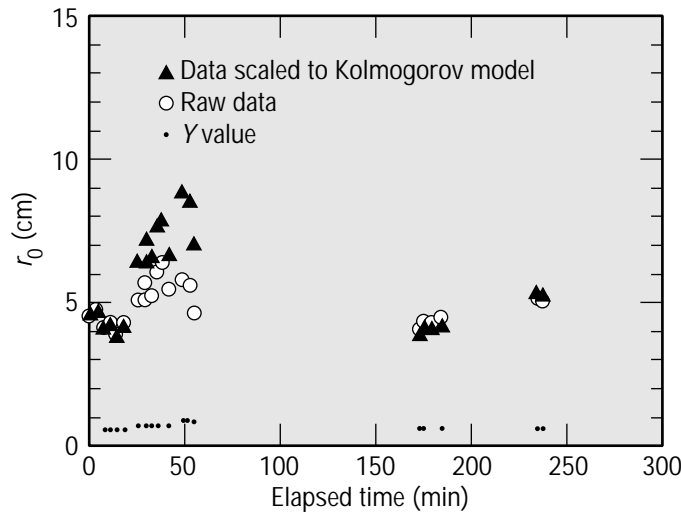


Figure 1. Values of  $r_0$  measured for the night of September 29, 1993. Solid triangles represent the values calculated for a fit of MTF data to a function of  $r_0$ . Those values are not collected for zenith angle and wavelength. Open circles represent the same data when the data are scaled to a single wavelength and vertical incidence. Note that  $r_0$  increases early in the night, because of either better seeing or a non-Kolmogorov effect.

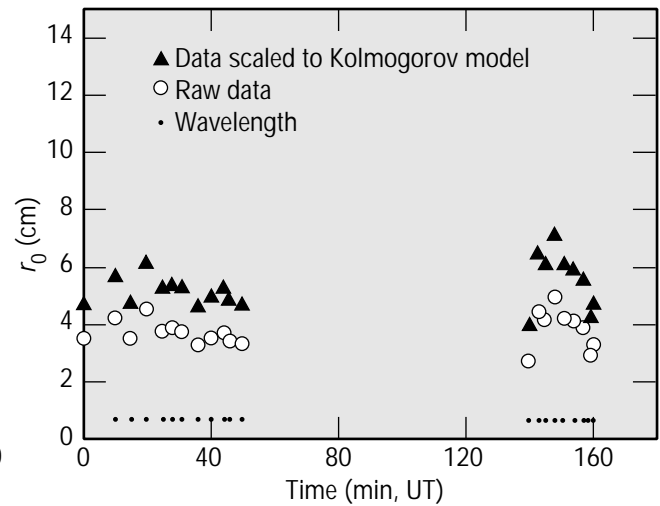


Figure 2. Values of  $r_0$  measured for the night of March 11, 1993. Notation is same as in Figure 1. All data are at a single wavelength; therefore, variability reflects changes in atmospheric conditions, indicating that the atmosphere is not likely to be stationary over long periods of time.

1. Bradford, L. W., S. M. Flatté, and C. E. Max (1994), "Modelling Atmospheric Turbulence Effects on Ground-Based Telescope Systems," in *Adaptive Optics for Astronomy*, D. Alloin and J.-M. Mariotti, Eds. (Dordrecht, The Netherlands: Kluwer).
2. Bradford, L. W., S. M. Flatté, and C. E. Max (1994), "Modeling Atmospheric Turbulence Effects on a Ground-Based Interferometer," in *Amplitude and Intensity Spatial Interferometry II*, J. B. Breckinridge, Ed., *Proc. SPIE* **2200**.
3. Flatté, S. M., L. W. Bradford, and C. E. Max (1994), "Modeling Atmospheric Turbulence Effects on Ground-Based Telescope Systems," in *Atmospheric Propagation and Remote Sensing III*, W. A. Flood and W. B. Miller, Eds., *Proc. SPIE* **2222**.
4. Tatarskii, V. I. (1971), *The Effects of the Turbulent Atmosphere on Wave Propagation* (U.S. Department of Commerce, Washington, DC).
5. Olivier, S. S., et al. (1994), "Performance of Adaptive Optics at Lick Observatory," in *Adaptive Optics in Astronomy*, M. A. Ealey and F. Merkle, Eds., *Proc. SPIE* **2201**.
6. Schneiderman, A. M., and D. P. Karo (1978), "Measurements of  $r_0$  with Speckle Interferometry," *J. Opt. Soc. Am.* **68**, 348–351.
7. Bester, M., W. C. Danchi, C. G. Degiacomi, L. J. Greenhill, and C. H. Townes (1992), "Atmospheric Fluctuations—Empirical Structure Functions and Projected Performance of Future Instruments," *Astrophys. J.* **392**, 357–374.

## References

## The r-Process in Supernovae and Parameterized Nucleosynthesis

**Principal Investigator:** Stanford E. Woosley (UC Santa Cruz)

**LLNL Collaborators:** Grant J. Mathews and James R. Wilson

**Student:** Robert D. Hoffman (UC Santa Cruz)

---

### Abstract

*In this project, we focused on the r-process, especially a series of calculations designed to give quantitative support to our earlier contention that these neutron-rich nuclei are produced in Type II and Ib supernovae as a result of a neutrino-driven wind during the first 10 to 20 s after the explosion. We also continued our studies of intermediate mass nucleosynthesis in massive stars, with emphasis on long-lived gamma-ray radio activities, and we explored the production of rare neutron-rich species in Chandrasekhar mass supernovae of Type Ia.*

---

### Objectives

We originally proposed to study several topics in stellar nucleosynthesis: (1) heavy-element production in the hot bubble, a region of high-entropy (up to 500) that comes to exist between the surface of a young (1 to 20 s) neutron star and the receding shock following core bounce, in those supernovae that leave neutron stars; (2) a parameterized (model-independent) survey of hydrostatic and explosive nucleosynthesis that would span the entire temperature spectrum of explosive and hydrostatic processing in massive stars; (3) the publication of a small, fast nuclear reaction network that accurately estimates the nuclear energy generation rate during advanced stages of stellar evolution; and (4) the production and distribution of a tabular compilation of our nuclear reaction rate tables for strong, electromagnetic, weak, and neutrino-induced reactions on nuclei from hydrogen to ruthenium (atomic number between 1 and 44). Progress was made in all four areas, but we spent the most time and learned the most in studying the r-process.<sup>1</sup>

---

### Progress

We calculated the nucleosynthesis arising from the neutron- and  $\alpha$ -rich freeze-out of material initially in nuclear statistical equilibrium that occurs within neutrino-driven winds during the first 18 s of a model supernova. In particular, we examined the last  $0.03 M_{\odot}$  ejected using conditions taken directly from the latest  $20 M_{\odot}$  delayed explosion model of Wilson and Mayle.<sup>2,3</sup> We found that the nucleosynthesis arising from the last  $10^{-4} M_{\odot}$  of ejecta was indeed in very good agreement with the solar r-process, both in terms of its composition and the total mass required by Galactic chemical evolution. This result was achieved without adjustment of the physical parameters (entropy, neutron excess, expansion time scale) affecting the nucleosynthesis in the model. Competing efforts by other research groups<sup>4-6</sup> also confirmed that the r-process evolved within the context of the neutrino-driven wind scenario described by our earlier papers.<sup>7,8</sup> However, these parametric studies were not based on a realistic supernova explosion model and thus lacked adequate detail to prove the case.

Despite our success, the present model suffers from a large overproduction of neutron-rich material, mostly nuclei with a closed  $N = 50$  neutron shell, during the first second of the explosion. If ejected, these would overwhelm the successful r-process isotopes made a few seconds later. This defect may originate from uncertainties in the supernova model, for example, because of the inherently



multidimensional character of the event we are studying or because of relatively small errors in the electron fraction  $Y_e$  characterizing ejecta at this time. We suggested in our paper that this defect might be avoided by appealing to convection in the early part of the calculation, where the overproduced  $N = 50$  isotones might not be ejected, but rather returned to the neutron star. At later times, the character of the hot bubble changes to a neutrino-driven wind, and the subsequent conditions necessary for the evolution of the r-process isotopes are retained.

Our most recent efforts to avoid the  $N = 50$  overproduction problem center more on uncertainties in  $Y_e$  and suggest the exciting possibility of producing the previously unaccounted for light p-process nuclei  $^{70}\text{Ge}$ ,  $^{74}\text{Se}$ ,  $^{78}\text{Kr}$ ,  $^{84}\text{Sr}$ ,  $^{92}\text{Mo}$ , and  $^{96}\text{Ru}$  in the same neutrino-driven wind that eventually gives rise to the r-process. The synthesis of the latter two is especially welcome in light of their deficiency in the best current models for the p-process.<sup>9</sup> The inclusion of electron-neutrino and anti-neutrino capture reactions on free nucleons and heavy nuclei can alter the neutron excess of the material in the wind and reduce at early times its very neutron-rich character, which led to the principal failure of the current model. The flux and spectra of the electron neutrinos, combined with the systematics of the nuclei in the region from zinc to ruthenium, allow the nuclear flows to proceed along a path that is more proton-rich and can provide for both a diminishment of the large overproduction factors of neutron-rich  $N = 50$  isotones and favor the production of the rare p-nuclei mentioned above. We are continuing to study this problem with George Fuller (UC San Diego) and Brad Meyer (Clemson).

A definitive answer that fully explains the production of the solar abundances of the r- and light p-nuclides will likely come from future models that incorporate all of these factors, the individual aspects of which we are currently studying. Nevertheless, we are encouraged to find such a rich and diverse site in nature that can provide for the production of some of nature's rarest material.

We also prepared a table of reaction rates that includes the nuclear data used in the r-process studies,<sup>1,7,8</sup> the ongoing massive star nucleosynthesis surveys at LLNL,<sup>10–12</sup> and the parameterized nucleosynthesis survey<sup>13</sup> being carried out at UC Santa Cruz. Additionally, we have made available the reaction rate database and the programs needed to calculate the nuclear reaction rates on intermediate mass isotopes contained in Woosley et al.<sup>14</sup> These are available on request and will soon be available on the World Wide Web.

With the advent of multidimensional models, there is considerable demand for a fast, accurate code that provides the nuclear-energy generation rate. We have developed and tested a small, nine-isotope reaction network that provides an accurate estimate for the nuclear-energy generation rate during advanced stellar burning conditions ranging from helium to oxygen burning. Versions of this code are being used by several researchers to study multidimensional massive star collapse in Type II and Ia supernova models and in the propagation of detonation and deflagration fronts in degenerate material. A specialized version that more accurately tracks the evolution of the neutron excess is already in use in Wilson's core collapse code and in the multidimensional supernova models of Herant and Benz.

## References

1. Woosley, S. E., J. R. Wilson, G. J. Mathews, R. D. Hoffman, and B. S. Meyer (1994), *Astrophys. J.* **433**, 229.
2. Wilson, J. R. (1992), in preparation for *Astrophys. J.*
3. Wilson, J. R., and R. W. Mayle (1993), *Phys. Reports* **227**, 97.
4. Witt, J., H. Th. Janka, and K. Takahashi (1993), *Astron. Astrophys.* **286**, 841.
5. Takahashi, K., J. Witt, and H. Th. Janka (1993), *Astron. Astrophys.* **286**, 857.
6. Howard, W. M., S. Goriely, M. Rayet, and M. Arnould (1993), *Astrophys. J.* **417**, 713.
7. Woosley, S. E., and R. D. Hoffman (1992), *Astrophys. J.* **395**, 202.
8. Meyer, B., G. Mathews, W. M. Howard, S. E. Woosley, and R. Hoffman (1992), *Astrophys. J.* **399**, 656.
9. Rayet, M., M. Arnould, M. Hashimoto, N. Prantzos, and K. Nomoto (1994), submitted to *Astron. Astrophys.*
10. Weaver, T. A., and S. E. Woosley (1995), in preparation for *Astrophys. J. Suppl.*
11. Timmes, F. X., S. E. Woosley, and T. A. Weaver (1994), Lawrence Livermore National Laboratory, Livermore, CA, UCRL-JC-118277.
12. Woosley, S. E., and T. A. Weaver (1995), in preparation for *Astrophys. J. Suppl.*
13. Hoffman, R. D., S. E. Woosley, T. A. Weaver, R. G. Eastman, F. X. Timmes, and D. H. Hartmann (1994), UCO Preprint 44.

# Dark Matter Neutrinos, Weak Interaction Physics, and Supernova Dynamics and Nucleosynthesis

**Principal Investigator:** George M. Fuller (UC San Diego)

**LLNL Collaborators:** Grant J. Mathews, James R. Wilson, and Ron Mayle

**Student:** Gail C. McLaughlin (UC San Diego)

## Abstract

*We have investigated several weak interaction physics issues that bear on nucleosynthesis from neutrino-heated supernova ejecta. In particular, we have continued our study of the relationship between matter-enhanced neutrino flavor transformation ( $\nu_{\tau(\mu)} \leftrightarrow \nu_e$  or  $\bar{\nu}_{\tau(\mu)} \leftrightarrow \bar{\nu}_e$ ) and supernova heavy-element nucleosynthesis. We have also computed neutrino and anti-neutrino capture rates on heavy nuclei. In turn, these rate calculations have suggested to us that p-process nucleosynthesis may have its origin in neutrino-heated supernova ejecta at times less than 1 s after core bounce.*

## Objectives

The objectives of this project included a further investigation of matter-enhanced neutrino flavor transformation and concomitant nucleosynthesis effects in the post-core-bounce supernova environment.<sup>1</sup> This is important because the  $\nu_\mu$  and/or  $\nu_\tau$  vacuum masses that give neutrino-mass level crossings in the region of the supernova where heavy-element nucleosynthesis originates are coincidentally the same as those of interest for neutrino hot dark matter (1 to 100 eV). Another objective is to calculate neutrino and anti-neutrino capture rates on heavy nuclei.

Neutrino flavor transformation probabilities in the supernova environment can be affected by the manner in which neutrino–neutrino forward scattering is treated. Furthermore, density fluctuations in the environment above the neutrino sphere could conceivably cause neutrino flavor decoherence. In this process, for example, a pure beam of, say,  $\nu_\tau$  propagates through fluctuations and becomes equal parts  $\nu_e$  and  $\nu_\tau$ .

## Progress

In FY 1994, we made considerable progress on several issues of weak interactions in the supernova problem. Studies of neutrino captures on heavy nuclei are nearly completed,<sup>2</sup> and we are still wrestling with the problem of neutrino flavor evolution in the post-core-bounce supernova environment.

Calculations on neutrino–neutrino forward scattering contributions and matter-enhanced neutrino flavor conversion in supernovae are well under way.<sup>3</sup> This is a difficult problem to treat properly, in part because of the nonlinear nature of the weak potential seen by a neutrino propagating above the neutrino sphere. This potential is partly contributed by neutrino–neutrino forward scattering, so it depends on the flavor states of the background neutrinos. In turn, what flavor state the neutrino resides in depends on the weak potential (and the prior history of the weak potential) encountered by the neutrino. In FY 1994, we discovered a numerical scheme to treat this problem.

Neutrino and anti-neutrino capture rates on heavy nuclei were calculated for conditions relevant for the region above the neutrino sphere in supernovae.<sup>2</sup> We found that these rates are dominated by the Fermi and Gamow–Teller resonance transitions. These rates have led us to suggest a possible production channel for

some of the light p-process nuclei, particularly  $^{92}\text{Mo}$ . We are undertaking a systematic study of this site in the supernova as a likely environment for the production of the light p-isotopes.<sup>4</sup> Part of our research will involve computing the neutrino capture rates on heavy nuclei.

We also investigated the ramifications of matter-enhanced neutrino flavor transformation on the detection of neutrinos from a galactic supernova.<sup>5</sup>

---

## References

1. Qian, Y.-Z, G. M. Fuller, G. J. Mathews, R. Mayle, J. R. Wilson, and S. E. Woosley (1993), "Connection between Flavor Mixing of Cosmologically Significant Neutrinos and Heavy Element Nucleosynthesis in Supernovae," *Phys. Rev. Lett.* **71**, 1965.
2. Fuller, G. M., and B. S. Meyer (1994), "Neutrino Capture and Supernova Nucleosynthesis," submitted to *Astrophys. J.*
3. Qian, Y.-Z, and G. M. Fuller (1994), "Signature of Supernova Neutrino Flavor Mixing in Water Cerenkov Detectors," *Phys. Rev. D* **49**, 1762.
4. Hoffman, R., S. E. Woosley, G. M. Fuller, and B. S. Meyer, in preparation (1994).
5. Qian, Y.-Z, and G. M. Fuller (1994), "Neutrino-Neutrino Scattering and Matter Enhanced Flavor Transformation in Supernovae," submitted to *Phys. Rev. D*.

# Numerical Studies of Fragmentation in Star-Forming Regions

**Principal Investigator:** Christopher F. McKee (UC Berkeley)

**LLNL Collaborators:** Richard I. Klein, John Bell, Louis H. Howell, and Jeffrey Greenough

**Student:** John H. Holliman II (UC Berkeley)

## Abstract

*The fragmentation of star-forming molecular clouds is poorly understood, in part, because of the highly nonlinear nature of the process and its sensitivity to the initial conditions. Previous simulations of this process have suffered conceptually because collapse is started from a contrived initial state that is usually far out of equilibrium, is always highly unstable, and does not include all of the pressure components that contribute to dynamical support in clouds. We have developed an analytic formalism that determines the structure and assesses the stability of clouds when support from thermal motions, Alfvénic turbulence, and static magnetic fields is included. Prior work has also had the disadvantage of using conventional numerical schemes with prohibitive computational requirements. Therefore, as a prelude to studying fragmentation, we incorporated gravity into a powerful adaptive mesh refinement hydrodynamics algorithm recently developed at LLNL. Our unique code is highly discriminating in allocating time resources, thus allowing fragmentation to be modeled with unprecedented resolution. During FY 1994, we improved the analytic stability formalism, completed the code development tasks, and began testing our algorithm on a supercomputer.*

## Objectives

Star formation plays a crucial role in galactic evolution and is critical in determining the structure of the interstellar medium; nevertheless, answers to basic questions concerning this process remain elusive: What dictates the rate of star formation? What determines the relative proportions of low-mass and high-mass stars? A key step in the star-formation process is fragmentation, whereby massive molecular clouds or clumps within the clouds break up into substantially less massive cores that may in turn condense into stars. The first objective of our work is to develop the numerical technology and conceptual advances that will allow us to consider this problem realistically. Code development includes testing on a standard suite of problems. Once the working status of the code is established, the primary goals of the simulation are to: (1) assess the nature of fragmentation in environments where massive stars form and (2) investigate the sensitivity of the results to the rotational rate, the relative support from Alfvén waves and static magnetic fields, and the density perturbation spectrum. Our analysis may determine whether the initial spectrum of perturbations, or the fragmentation process itself, dictates the mass distribution of the fragments. The effort could thus effect a fundamental advance in our understanding of star formation.

## Progress

Our numerical work was motivated in part by conceptual weaknesses in earlier fragmentation studies that include neither meaningful initial conditions for collapse nor realistic treatments of the nonthermal dynamical support in star-forming clouds. At the time of the original proposal, Holliman and McKee had developed a formalism that determined the equilibrium structure and stability of gas spheres supported

by thermal motions and Alfvén waves. In the interim, we augmented this scheme to approximate the effect of static magnetic fields on the initial condition for collapse. The substantial influence of static magnetic fields is a general feature in star-forming regions, but their effect on structure and stability when Alfvén waves are also present had not previously been determined. The detailed magnetic-field geometry is relatively difficult to calculate, and its evolution can only be followed with a magnetohydrodynamic code. However, because we model magnetized systems as gas spheres with polytropic pressure components, our analysis is straightforward. The agreement with the detailed calculations for isothermal clouds that have been performed by others is excellent. Additionally, the equation of state that is needed in the adaptive mesh refinement (AMR) algorithm to represent support from thermal motions, Alfvén waves, and static magnetic fields is readily obtained from our formalism.

We proposed this project having previously used an AMR hydrodynamics code without gravity on several astrophysically significant problems.<sup>1–3</sup> The task of coupling the Godunov integrator in the hydrodynamics algorithm to an adaptive, multigrid solver for self-gravity was divided into four steps. Preliminary work involved moving the component texts to our development platforms—Sun workstations and a Cray supercomputer—and adapting this source code to the peculiarities of the compilers. We confirmed that the Godunov integrator and elliptical solver for gravity were working properly on an individual basis. Next, we joined these codes so that, at each time step, the multigrid solver computes the gravitational potential of the density distribution and then adds the corresponding body force to each cell before the next step. We were the first group to couple these numerical schemes. The third step was to update the Godunov integrator to include the self-induced gravitational forces. A convergence study indicated that, following this additional coupling, the code provided the anticipated second-order accuracy. In the final developmental step, we incorporated the coupled routines into the hierarchical AMR algorithm.

We requested and received both a development grant and a production grant for this work on the Cray Y-MP C90 at the Pittsburgh Supercomputing Center. The fully funded production grant is being used to complete the standard test suite and to conduct a pilot study that will determine which parameters would be most profitably varied in our subsequent high-resolution runs.

---

## References

1. Klein, R. I., J. Bell, R. Pember, and T. Kelleher (1993), in *Fourth Int. Conf. on Compressible Turbulence*, P. F. Linden, Ed. (Cambridge: Cambridge University Press).
2. Klein, R. I., C. F. McKee, and P. Colella (1994), “On the Hydrodynamic Interaction of Shock Waves with Interstellar Clouds: I. Nonradiative Shocks in Small Clouds,” *Astrophys. J.* **420**, 213.
3. Woods, D. T., R. I. Klein, J. I. Castor, C. F. McKee, and J. B. Bell (1994), submitted to *Astrophys. J.*

## Dust-Driven Winds from Pulsating, Late-Type Stars

**Principal Investigator:** Mark Morris (UC Los Angeles)

**LLNL Collaborator:** John I. Castor

**Student:** Nickolaos Mastrodemos (UC Los Angeles)

### Abstract

*We have produced dynamical models of winds originating from pulsating late-type giants. Our primary focus is the interaction between gas and dust under the effect of pulsation and the detailed density structure of the wind. The preliminary findings of this work are that, although there exists a potential instability in the two-fluid flow, it cannot grow significantly in the time available for most realistic conditions. Thus, the wind appears to be stable and uniform on large scales.*

### Objectives

The formation of dust grains in the atmospheres of pulsating red giants occurs under highly irregular conditions. With a linearized treatment of the dust–gas flow equations, we have shown that the drift of dust grains through the gas can amplify initial inhomogeneities for certain wavelengths on time scales shorter than the wind flow time, thus leading to instabilities. Of particular interest is the possibility of resonances between the growing modes and the periodic luminosity variation of the star. If resonances exist, they may favor growth of certain wavelengths, thereby further enhancing the density contrast. To investigate the wind structure in the nonlinear regime, we constructed a numerical simulation of a dust-driven wind.

### Progress

The basis of our numerical study is a one-dimensional hydrodynamic code originated and used by Owocki and Castor to study winds from OB stars. This code uses a staggered-mesh and explicit time stepping that is operator split into Lagrangian and advection steps. Advection is performed with Van Leer’s second-order monotonization algorithm.

To adapt the code to the physics of red giant winds, we needed a number of modifications and additions. For example, to study the effects of dust-streaming, we included dust as a separate fluid. Also, the numerical inner boundary is kept fixed because we are not concerned with the actual pulsation of the star but with its luminosity variations. The levitating effect of the pulsation is accomplished by thermal expansion and by a fictitious mechanical force.

Dust grains are assumed spherical and form when the temperature drops below 1500 to 1200 K, depending on the dust species. Dust is not an ordinary fluid because its kinetic “temperature” is effectively zero. A single dust species is uniquely specified by the grain radius and density of its material. To better investigate the effects of different grain sizes and to reduce computational effort, we have so far confined our analysis to grains of a single size.

The two fluids—gas and dust—are momentum-coupled, and this coupling drives the wind. The coupling term is nonlinear, depending on the volume densities of the two fluids and on the gas kinetic temperature, and it is quadratic in the drift velocity. These dependences render the momentum equation very stiff in the inner 10 to 20 stellar radii. For typical velocities and mass-loss rates, the characteristic coupling time and length are as small as  $10^{-5}$  years and  $10^{-6}$  stellar radii, respectively, which is impossible to resolve. We have therefore opted for an implicit description of the momentum equation. The optimal spatial resolution was determined after some experimentation and observation of the resulting wave structure. A density

wave is typically contained within 20 to 30 zones. To extend our calculations to a radial distance of  $10^{16}$  cm, we need a spatial mesh with 9000 to 12,000 points.

Of particular importance for the time integration is the initial state. We learned that an initial state far from the steady-state solution will usually result in enormous shocks and transients propagating outward. To eliminate this problem, we determine the initial state from the solution of the steady-state problem under the simplifying assumption of complete momentum coupling. This solution also saves considerably in computer processing time.

The energy balance of the wind must be properly accounted for to determine the extent to which thermal pressure can smooth out initial fluctuations. The most important heating and cooling mechanisms are heating that results from the viscous interaction between gas and dust, and cooling that results from adiabatic expansion and molecular excitation. These energy terms were included one at a time to better assess their relative importance.

At each stage, we explored parameter space by considering grain radii from  $10^{-8}$  to  $10^{-5}$  cm, mass-loss rates from  $10^{-7}$  to  $10^{-4}$  solar masses per year, gas terminal velocities of 10 to 20 km/s, and periods of luminosity variation between 100 and 1000 days. For all cases considered, the dust formation radius was between 1 and  $2 \times 10^{14}$  cm, consistent with observations. The dust opacity per unit mass was adjusted so that terminal gas velocities are within the observed values.

In our first exploratory phase, we considered an adiabatic wind. The temperature gradient appears very steep, with temperature dropping below the 2.73 K background at  $5 \times 10^{15}$  cm. The instability is apparent at every length scale, with the most rapid growth at shorter wavelengths. This finding is in agreement with our linearized analysis.

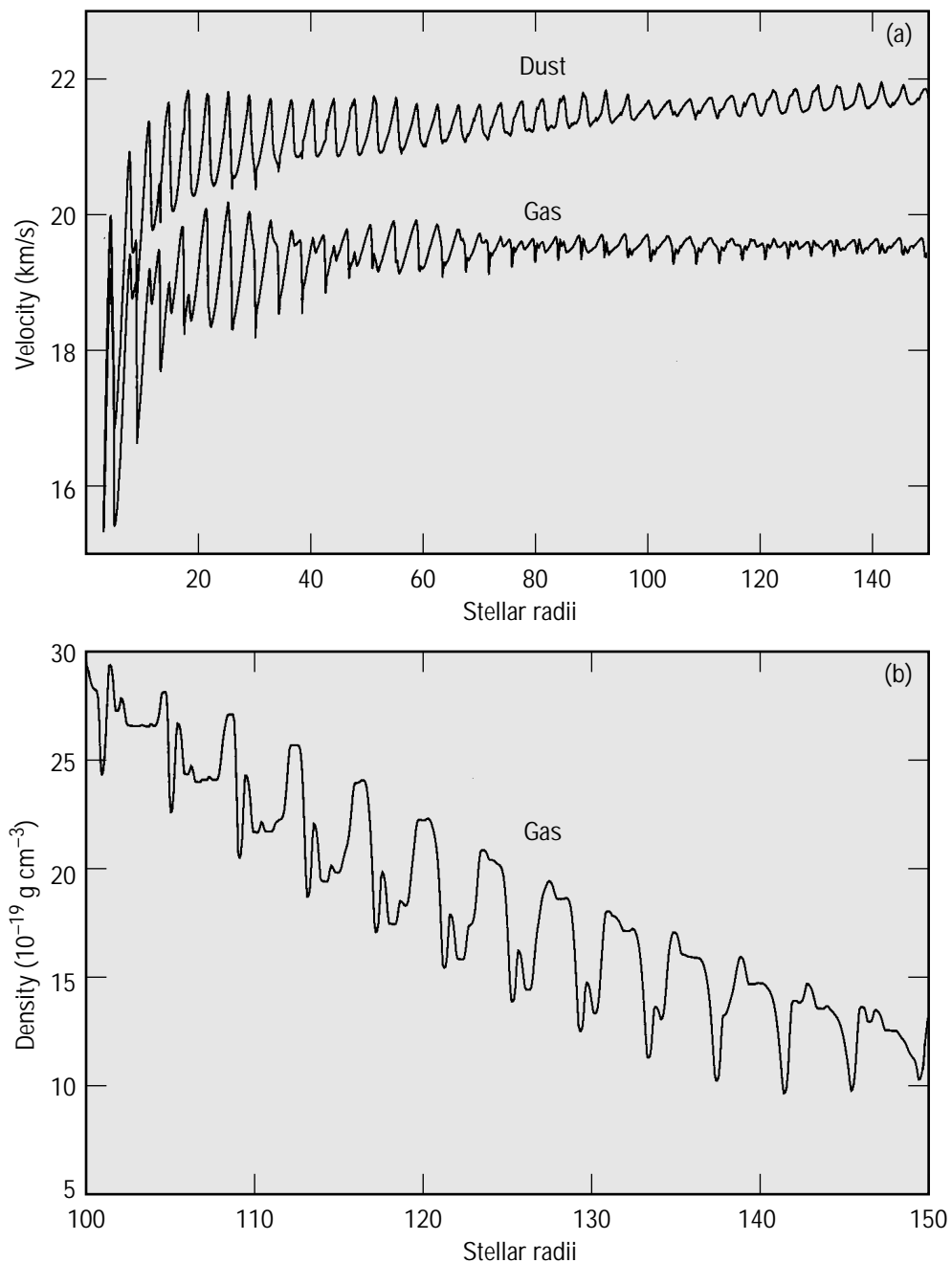
Adiabatic cooling is an unrealistic model, however, so we next added the viscous heating term, obtaining a more reasonable temperature structure, with temperature ranging from 80 to 150 K at  $10^{16}$  cm. Growth of short wavelengths completely disappears under these circumstances. Longer wavelengths, although present at large radial distances, do not appear to grow any faster than they are advected, so the instability is suppressed.

Figure 1 shows waves provoked by the periodic luminosity variations of the star. The wave amplitude appears to increase slightly with an increase in the period of luminosity variation. It is also proportional to the mass-loss rate and to the ratio of the gas to drift velocity. The latter is in agreement with results from an absolute stability analysis. For mass-loss rates of  $10^{-5} M_{\odot}/\text{year}$  and terminal velocities of  $\sim 20$  km/s, the drift velocity is  $\sim 2$  km/s. This velocity implies a rather strong coupling between the two fluids that does not allow the fluctuations to diminish. At mass-loss rates of  $10^{-6}$  and terminal velocities of  $\sim 15$  km/s, the drift velocity is higher,  $\sim 4$  km/s, and the amplitude of the waves diminishes with distance.

A prominent feature is the formation of wavepackets in the profiles of all physical variables, containing as many as 20 of the individual waves. These wavepackets resemble standing waves; their maximum and minimum amplitudes are at fixed locations. This is a surprising and somewhat unexpected feature. We speculate that it is owed to the interaction of two growing modes, one lagging behind the gas and one moving essentially with the dust. A typical envelope wavelength is 1 to  $2 \times 10^{15}$  cm.

To complete the correct description of energy balance, we included the most important cooling terms, rotational and vibrational transitions of  $\text{H}_2\text{O}$  and  $\text{H}_2$ , respectively. The temperature at  $10^{16}$  cm is now 30 to 40 K. Whether the instability will be rekindled by the inclusion of cooling is under investigation. As of this writing, the production runs are under way, and we expect to conclude this investigation during FY 1995.





*Figure 1. Variations of physical quantities with radius in the presence of a star having a periodic, two-year luminosity variation of 50% about 6000 solar luminosities: (a) outflow velocity of gas and dust and (b) gas density.*



## Section IV. IGPP–LLNL Seminars and Workshops

### *Center for Geosciences*

#### **Seminars**

December 9, 1993

“Measurements of Anisotropic Elastic Moduli and Comparison with Equivalent Media Theories”

Julie Hood, University of Miami

December 16, 1993

“PIXE and Related Techniques Applied to the Geosciences”

Graham Bench, GERP’s Center for Accelerator Mass Spectrometry

January 20, 1994

“Probing Phase Transformations in NaCl and Tridymite via Infrared Spectrometry at Pressure and Temperature”

Anne Hofmeister, UC Davis

February 17, 1994

“Phase Equilibria Studies of Amphibolite–Eclogite Transition”

Jun Liu, Stanford University

March 1, 1994

“Crustal Thickening and Lithospheric Thinning in the Indo-Asian Continental Collision”

Greg Houseman, Monash University, Australia

March 3, 1994

“Subducted Oceanic Sediments—Experimental Constraints on Highly Peraluminous Melts and Cl-Rich Fluids”

Geoff Nichols, California Institute of Technology

March 28, 1994

“Origin of the Giant Stratospheric SO<sub>2</sub> Cloud from the Climactic Eruption of Mount Pinatubo”

Terry Gerlach

March 30, 1994

“Rates of Silicate–Water Interactions in Natural Processes”

Eric Oelkers, University of Paul Sabatier, Toulouse, France

April 29, 1994

“Systematic Stress Variations in the Southern San Joaquin Valley and along the White Wolf Fault: Implications for the Rupture Mechanics of the 1952 Ms 7.8 Kern County Earthquake and Contemporary Seismicity”

David Castillo, Stanford University

May 5, 1994

“Ore Mineralization in the German Deep Drilling Project and Its Significance to Some Geophysical Parameters”

Agnes Kontny, University of Geissen, Germany

May 12, 1994

“History, Experience, and Possibilities of Interpretation of Magnetotelluric Measurements in the Eastern Part of Germany”

G. Porstendorfer, Bergakademie Freiberg, Institute of Geophysics, Freiberg, Germany

May 16, 1994

“Analysis of the Geochemical Aspects of the Underground Disposal of CO<sub>2</sub>”

Isabelle Czernichowski, Bureau de Recherches Geologiques of Minieres

June 2, 1994

“Perspectives on Mantle Melting from Thermodynamic Models of Minerals and Silicate Melts”

Marc Hirschmann, California Institute of Technology

June 1994

“Water Transport and Release in Subduction Zones: An Experimental Investigation of Hydrous Phases in Synthetic and Natural (Crustal) Systems”

Clermont Ferrand, Department de la Terre, CNRS, France

## *Center for High-Pressure Sciences*

---

### **Seminars**

February 3, 1994

“Theoretical Modeling of Island Growth during the Early Stages of Epitaxy”

Steven Bales, Sandia National Laboratory, California

February 11, 1994

“First-Principles Calculations for (100) Semiconductor Surfaces”

A. Garcia, Xerox PARC

February 14, 1994

“Dielectric Properties and Pressure-Induced Phase Transition of Stishovite”

Changyol Lee, Cornell University

February 17, 1994

“Magnetism and Normal-State Properties of the  $t$ - $J$  Model”

Y. R. Wang, Xerox Webster

March 3, 1994

Microanalysis of the Structure of Epitaxially Grown Superconducting Thin Films”

Rich Howell, LLNL

March 4, 1994

“Some Theoretical Considerations Involving Diamond Recovery in Dynamic Experiments”

Robert G. Arkhipov, Ree

March 10, 1994

“Optical Studies of Novel Strain-Layered Quantum Well Heterostructures”

W. Zhou

March 31, 1994

“Biomimetics Biomaterials: What’s in It for H-Division?”

D. Young, LLNL

April 7, 1994

“Electron-Lattice Interaction at Semiconductor Surfaces”

Oleg Pankratov

April 12, 1994

“Low- and High-Temperature Phases of Clean and Pb-Covered Ge(111) Surfaces”

Annabella Selloni, University of Geneva

April 14, 1994

“Charge-Transfer Phenomena in Polyphenylenevinylene/Molecularly Doped-Polymer Bilayer Devices”

Homer Antoniadis, Xerox

April 28, 1994

“Investigations of New Photonic Materials: Silicon Nanocrystals and Fullerenes”

Howard Lee, LLNL

June 2, 1994

“Ultrafast All-Optical Computations Using Conjugated Polymers”

Andrew W. Hays, UC Santa Barbara

June 9, 1993

“Powders under Shock Loading and Controlled High-Rate Shear Deformation”

Vitalii Nesterenko, UC San Diego and Novosibirsk State University

June 14, 1994

“Conjugated Polymers for Use in Schottky Devices”

Khashayar Pakbaz, UC Santa Barbara

June 16, 1994

“Properties of Nitrogen-Doped ZnSe”

Tony Chen, UC Berkeley and Lawrence Berkeley National Laboratory

June 30, 1994

“Organic Semiconductor Light-Emitting Diodes”

Ming Yan, AT&T Bell Labs

July 14, 1994

“Ultrahigh Pressure Research with the Femtosecond Laser”

Richard More, LLNL

July 21, 1994

“Cathodic Arc Deposition of Amorphous Diamond Thin Films”

Steve Falabella, LLNL

July 22, 1994

“Raman Scattering in Natural and C<sub>13</sub>-Enriched Diamond at High Pressure”

Sergei M. Stishov, Institute of High-Pressure Physics, Troitsk, Russia

August 4, 1994

“Electric Field Modulation Spectroscopy of Light-Emitting Molecules and Polymers”

Tom Hagler, Los Alamos National Laboratory

August 9, 1994

“A Unified Picture Crystal Structures of Metals”

Soderlind, University of Uppsala

August 11, 1994

“Ab Initio Study of Liquid Boron”

Gilles Zerah, Centre d’Etudes de Limeil, France

August 12, 1994

“Nonlinear Optical Probes of Solids under Pressure”

Magnus Lipp, University of Missouri

August 25, 1994

“Planar Fault Energies in Substitutionally Disordered TiAl Alloys”

Chris Woodward

September 15, 1994

“A Constitutive Model Based on Microstructure”

Steward Keeton, LLNL

September 22, 1994

“Dielectric Properties of Hydrogen under High Pressure”

William J. Evans

## *Astrophysics Research Center*

---

### **Seminars**

October 8, 1993

“Pulsars and Supernova Remnants”

Shrinivas Ramchandra Kulkarni, California Institute of Technology

October 15, 1993

“Infall and Outflows in Early Stellar Evolution”

Lee Hartman, CfA, Harvard

October 18, 1993

“The Crust of the Neutron Star”

Jochen Wambach, University of Illinois

October 19, 1993

“Planetary Nebula Formation: Filling in the Missing Link”

Margaret Meixner, UC Berkeley

October 22, 1993

“The True Shape of Elliptical Galaxies”

Tom Statler, University of North Carolina

October 29, 1993

“Peculiar Motions in the Universe”

Greg Bothun, University of Oregon

November 5, 1993

“The Distance to M81 from the Hubble Space Telescope”

Jeremy R. Mould, California Institute of Technology

November 12, 1993

“Probable Detection of Microlensing by Halo Objects: The MACHO Project’s  
First Year”

Kem Cook, LLNL

November 18, 1993

“Distant Radio Galaxies”

Huib Rottgering, Leiden Observatory, The Netherlands

November 19, 1993

“Planetary Nebulae and Their Role in the Progress toward the Hubble Constant”

George Jacoby, NOAO, Kitt Peak Observatory

December 3, 1993

“Making Mountains out of Mole Hills: Gas Dynamical Simulation of Galaxy and  
Large-Scale Structure Formation”

Paul Shapiro, University of Texas



December 10, 1993

“The Structure of Spheroidal Nuclei as Seen with the Space Telescope”

Sandy Faber, UC Santa Cruz

January 7, 1994

“On Constraining the Small-Scale Structure of the Early Universe by Primordial Nucleosynthesis”

Karsten Jedamzik, LLNL–IGPP

January 21, 1994

“COBE Observations and the Early Universe”

George Smoot, Space Sciences Laboratory, UC Berkeley

January 28, 1994

“Pixion Quantification of Picture Information Content with Application to Image Reconstruction”

Richard Puetter, UC Diego

February 4, 1994

“Galaxy Evolution in Moderate Redshift Clusters”

Adam Stanford, IPAC, Jet Propulsion Laboratory

February 18, 1994

“The VLA FIRST Survey: A Progress Report”

Bob Becker, UC Davis–IGPP

February 25, 1994

“Relativistic Shocks and the Excitation of the Crab II Nebula”

Jonathan Arons, UC Berkeley

March 4, 1994

“Cosmic Microwave Background Anisotropies after COBE”

Douglas Scott, UC Berkeley

March 8, 1994

“Galaxy Dynamics and the Mass of the Universe”

Vera Rubin, Carnegie Institution of Washington

March 11, 1994

“Pluto’s Atmosphere: Where It Comes from and Where It’s Going”

Roger V. Yelle, University of Arizona

March 18, 1994

“Evidence that Gamma-Ray Bursts Repeat and Are Galactic in Origin”

Don Lamb, University of Chicago

March 21, 1994

“Testing Inflation”

Michael Turner, University of Chicago, FNAL

April 1, 1994

“Inferring Cloud Fragmentation via Near-Infrared Studies of a Young Star Cluster”

Mary Barsony, UC Riverside

April 8, 1994

“Gravitational Lensing, Time Delays, and Hubble’s Constant”

Jacqueline Hewitt, Massachusetts Institute of Technology

April 15, 1994

“Nucleosynthesis in Massive Stars”

Tom Weaver, LLNL

April 18, 1994

“The Shape of Dark Matter Halos: Another Conspiracy?”

Penny Sackett, Institute for Advanced Study, Princeton University

April 18, 1994

“White Dwarfs and Brown Dwarfs Theory: Galactic Implications”

Gilles Chabrier, Ecole Normale Supérieure de Lyon, Cedex, France

April 22, 1994

“Galileo Enroute to Jupiter”

Torrence Johnson, Jet Propulsion Laboratory

April 29, 1994

“Infrared to X-Ray Spectral Energy Distributions of High-Redshift Quasars”

Jill Bechtold, University of Arizona

May 2, 1994

“Infall to the Galactic Center”

Paul Ho, Smithsonian Astrophysical Observatory

May 4, 1994

“Spectral Characteristics of Local Galaxies”

Anne Kinney, Space Telescope Science Institute

May 6, 1994

“Galactic Accretion Disks: Lifting the Veil on Halos”

Tom Steiman-Cameron, NASA/Ames

May 10, 1994

“Science with the Infrared Array Spectrometer CGS4 on the United Kingdom  
Infrared Telescope—From the Solar System to the Edge of the Universe”

Gillian Wright, United Kingdom Infrared Telescope

May 13, 1994

“Batch Discovery of Six High-Redshift Supernovae: Developing a New Tool for  
Cosmology”

Saul Perlmutter, Lawrence Berkeley National Laboratory

May 17, 1994

“UCLA Infrared Camera and an Infrared Search for Brown Dwarfs in the Hyades”

Bruce Macintosh, UC Los Angeles

May 20, 1994

“Measuring the Extragalactic Distance Scale with Type II Supernovae”

Ron Eastman, LLNL

May 27, 1994

“Mining the MACHO Database: Microlensing and Variable Stars”

Kem Cook, IGPP–LLNL

August 12, 1994

“Multi-Wavelength Signatures of Galactic Black Holes”

Edison Liang, Rice University and LLNL

September 9, 1994

“The Propagation of MHD Waves in Plasma with Random Inhomogeneities”

Margarita P. Ryutova, Institute of Nuclear Physics, Novosibirsk, Russia

September 16, 1994

“Results from the ASCA X-Ray Observatory”

Nick White, NASA/GSFC

September 22, 1994

“Three-Dimensional Local Instability in Accretion Disks”

Tzi-Hong Chiueh, National Central University, Taiwan

September 23, 1994

“Cosmic Gamma-Ray Bursts and Soft Gamma-Ray Repeaters”

Kevin Hurley, UC Berkeley, Space Sciences Laboratory

September 29, 1994

“Gamma-Ray Bursts from Fast Neutron Stars in the Galactic Halo”

Stirling Colgate, Los Alamos National Laboratory

September 30, 1994

“Galaxy Formation and Globular Clusters”

Steve Zepf, UC Berkeley

## **Workshop**

March 17–19, 1994

“Galactic Chemical Dynamics”

Host: Grant Mathews, LLNL



## Section V. Bibliography

1994

- Arons, J., and M. Tavani (1994), "Relativistic Particle Acceleration in Plerions," *Astrophys. J. Suppl.* **90**, 797.
- Aufderheide, M., I. Fushiki, G. Fuller, and T. Weaver (1994), "A New URCA Process," *Astrophys. J.* **424**, 257.
- Aufderheide, M., I. Fushiki, S. Woosley, and D. Hartmann (1994), "Search for Important Weak Interaction Nuclei in Presupernova Evolution," *Astrophys. J. Suppl.* **91**, 389.
- Beck, S., et al. (1994), "Across the Andes and along the Altiplano: A Passive Seismic Experiment," *IRIS Newsletter*, Vol. XIII, No. 3, pp. 1–3.
- Becker, R., R. White, D. Helfand, and S. Zoonematkermani (1994), "A 5-GHz VLA Survey of the Galactic Plane," *Astrophys. J. Suppl.* **91**, 347.
- Beckers, J., S. Y. Schwartz, and T. Lay (1994), "The Velocity Structure of the Crust and Upper Mantle under China from Broad-Band P and PP Waveform Analysis," *Geophys. J. Int.* **119**(2), 574.
- Benson, D. J., and W. J. Nellis (1994), "Dynamic Compaction of Copper Powder—Computation and Experiment," *Appl. Phys. Lett.* **65**(4), 418–420.
- Brenan, J. M., H. F. Shaw, D. L. Phinney, and F. J. Ryerson (1994), "Rutile-Fluid Partitioning of Nb, Ta, Hf, Zr, U, and Th: Implications for High-Field-Strength Element Depletions in Island-Arc Basalts," *Earth Planet. Sci. Lett.* **128**, 327–339.
- Charlot, S. and J. Silk (1994), "Evolution of Galaxies in Clusters," *Astrophys. J.* **432**, 453.
- Cordier, P., A. A. Gratz, J. C. Doukhan, and W. J. Nellis (1994), "Microstructures of  $\text{Al}_2\text{O}_3$  Subjected to High Shock Pressures," *Phys. Chem. Minerals* **21**(3), 133–139.
- Dey, A., and W. van Breugel (1994), "Blue Optical Continuum Emission Associated with a Radio Knot in 3C34G," *Astrophys. J.* (submitted).
- Erskine, D., W. J. Nellis, and S. T. Weir (1994), "Shock Wave Profile Study of Tuff from the Nevada Test Site," *J. Geophys. Res. Solid Earth* **99**(8), 15529–15537.
- Erskine, D., W. Nellis, and S. Weir (1994), "Shock Wave Profile Study of Tuff from the Nevada Test Site," *J. Geophys. Res.* **99**, 15529.
- Farber, D., Q. Williams, and R. Ryerson (1994), "Diffusion in  $\text{Mg}_2\text{SiO}_4$  Polymorphs and Chemical Heterogeneity in the Mantle Transition Zone," *Nature*, **371**, 693.

- Freim, J., J. McKittrick, W. J. Nellis, and J. D. Katz (1994), "Improved Zirconia-Toughened Alumina (ZTA) Microstructures Obtained through Rapid Solidification and Shock Compaction," *J. Mater. Res.* (submitted).
- Fuller, G. M., and B. S. Meyer (1994), "Neutrino Capture and Supernova Nucleosynthesis" (submitted).
- Fuller, G. M., K. Jedamzik, G. J. Mathews, and A. Olinto (1994), "On Constraining Electroweak-Baryogenesis with Inhomogeneous Primordial Nucleosynthesis," *Phys. Lett. B* **333**, 135.
- Gallant, Y., and J. Arons (1994), "Structure of Relativistic Shocks in Pulsar Winds: A Model of the WISPs in the Crab Nebula," *Astrophys. J.* **435**, 230.
- Ghez, A. M., J. P. Emerson, J. R. Graham, M. Meixner, and C. J. Skinner (1994), "10-Micron Imaging of Uz Tauri: Evidence for Circumstellar Disk Clearing due to a Close Companion Star," *Astrophys. J.* **434**, 707.
- Gregg, M. (1994), "Spectrophotometry of Early Type Systems. I. A Metallicity Sequence of Globular Clusters," *Astron. J.* **108**, 2164.
- Hawley, S., and G. Fisher (1994), "Solar Flare Model Atmospheres," *Astrophys. J.* **426**, 387.
- Helfand, D. J., R. H. Becker, G. Hawkins, and R. L. White (1994), "The Nature of the Compact X-Ray Source in the Supernova Remnant G27.4+0.0," *Astrophys. J.* **434**, 627.
- Hoffman, R., S. E. Woosley, T. Weaver, R. Eastman, F. Timmes, and D. Hartmann, (1994), "Gamma-Ray Producing Radioactivities from Supernova Explosion," in *Gamma-Ray Sky*, Signore, Salati, and Vedrenne, Eds. (Kluwer Academic Publishers).
- Hough, S. (1994), "Southern Surface Rupture Associated with the M7.3 1992 Landers, California, Earthquake," *Bull. Seis. Soc. Am.* **84**, 817.
- Jedamzik, K., and G. M. Fuller (1994), "Baryon Number Transport in a Cosmic QCD-Phase Transition," (submitted).
- Jedamzik, K., and G. M. Fuller, (1994), "The Evolution of Nonlinear Subhorizon-Scale Entropy Fluctuations in the Early Universe," *Astrophys. J.* **423**, 33.
- Jedamzik, K., G. M. Fuller, and G. J. Mathews (1994), "Inhomogeneous Primordial Nucleosynthesis: Coupled Nuclear Reactions and Hydrodynamic Dissipation Processes," *Astrophys. J.* **423**, 50.
- Jedamzik, K., G. M. Fuller, G. J. Mathews, and T. Kajino (1994), "Enhanced Heavy-Element Formation in Baryon-Inhomogeneous Big Bang Models," *Astrophys. J.* **422**, 423.
- Jiao, W., T. C. Wallace, S. L. Beck, P. G. Silver, G. Zandt (1994), "Evidence for Static Displacements from the June 9, 1994, Deep Bolivian Earthquake," *Geophys. Res. Lett.* (submitted).

- Justtanont, K., C. J. Skinner, and A. G. G. M. Tielens, (1994), "Molecular Rotational Line Profiles from Oxygen-Rich Red Giant Winds," *Astrophys. J.* **435**, 852.
- Kagan, Y. Y., and D. D. Jackson, (1994), "Long-Term Probabilistic Forecasting of Earthquake," *J. Geophys. Res.* **99**, 13685.
- Kersting A. B., and R. J. Arculus (1994), "Klyuchevskoy Volcano, Kamchatka, Russia—The Role of High-Flux Recharged, Tapped, and Fractionated Magma Chamber(s) in the Genesis of High- $\text{Al}_2\text{O}_3$  from High-MgO Basalt," *J. Petrol.* **35**, 1–41.
- Klein, R., C. F. McKee, and P. Colella, (1994), "On the Hydrodynamic Interaction of Shock Waves with Interstellar Clouds: I. Nonradiative Shocks in Small Clouds," *Astrophys. J.* **420**, 213.
- Kramer, M. J., R. W. McCallum, W. J. Nellis, and U. Balachandran (1994), "Effects of Shock-Induced Defect Density on Flux Pinning in Melt-Textured  $\text{YBa}_2\text{Cu}_3\text{O}_{7-\delta}$ ," *J. Electron. Mater.* **23**, 1111–1115.
- Kramer, M. J., R. W. McCallum, W. J. Nellis, and U. Balachandran (1994), "Effects of Shock-Induced Defects and Subsequent Heat Treatment on Flux Pinning in Melt-Textured  $\text{YBa}_2\text{Cu}_3\text{O}_{7-\delta}$ ," *Physica C* **228**(3–4), 265–278.
- Lehnert, M., and T. Heckman (1994), "Emission-Line Ratios of the Integrated Spectra of Galaxies: Evidence for a Diffuse Ionized Medium in Other Galaxies?," *Astrophys. J. Lett.* **426**, L27.
- Lundstrom, C. C., H. F. Shaw, D. L. Phinney, F. J. Ryerson, J. B. Gill, and Q. Williams (1994), "New U–Th–Ba Partition Coefficients between Chromian Diopside and Haplobasaltic Melts," *Earth Planet. Sci. Lett* **128**, 407–423.
- Max, C. E., D. T. Gavel, S. S. Olivier, J. M. Brase, H. W. Friedman, K. Avicola, J. T. Salmon, A. D. Gleckler, T. S. Mast, J. E. Nelson, P. L. Wizinowich, and G. A. Chanan, (1994), "Issues in the Design and Optimization of Adaptive Optics and Laser Guide Stars for the Keck Telescopes," *SPIE* **2201**, 189.
- Myers, S. C., T. C. Wallace, S. L. Beck, P. G. Silver, G. Zandt, J. Vandecar, and E. Minaya (1994), "Implications of Spatial and Temporal Development of the Aftershock Sequence for the  $M_w$  8.3 June 9, 1994, Deep Bolivian Earthquake," *Geophys. Res. Lett.* (submitted).
- Qian, Y.-Z., and G. M. Fuller (1994), "Neutrino–Neutrino Scattering and Matter-Enhanced Neutrino Flavor Transformation in Supernovae" (submitted).
- Qian, Y.-Z., and G. M. Fuller (1994), "Signature of Supernova Neutrino Flavor Mixing in Water Cerenkov Detectors," *Phys. Rev. D* **49**, 1762.
- Schuessler, B. K., S. L. Beck, G. Zandt, and T. C. Wallace (1994), "Crustal Thickness Variations in the Central Andes of South America Determined from Regional Waveform Modeling of Earthquakes," *Geophys. J. Int.* (submitted).

- Skinner, C. J. (1994), "Red Giants with Unusual Dust Shells—II. The Dusty R Star HD 100764," *Monthly Notices*, **271**(2), 300.
- Skinner, C., M. Meixner, G. Hawkins, E. Keto, J. G. Jernigan, and J. Arens (1994), "Mid-Infrared Images of the Post-Asymptotic Giant Branch Star HD 161796," *Astrophys. J. Lett.* **423**, L-135.
- Skulski, T., W. Minarik, and E. B. Watson (1994), "High-Pressure Experimental Trace-Element Partitioning between Clinopyroxene and Basaltic Melts," *Chem. Geology* **117**, 127–149.
- Steck, L., and W. Prothero (1994), "Crustal Structure beneath Long Valley Caldera from Modeling of Teleseismic P Wave Polarizations," *J. Geophys. Res.* **99**, 6881.
- Sylvester, R., M. Barlow, and C. Skinner (1994), "UIR-Band Emission from M Supergiants," *Mon. Not. R. Astron. Soc.* **266**, 640.
- Tinker, M. A., T. C. Wallace, S. L. Beck, P. G. Silver, and G. Zandt (1994), "Aftershock Source Mechanisms from the June 9, 1994, Deep Bolivian Earthquake, *Geophys. Res. Lett.* (submitted).
- Tunaboylu, B., J. McKittrick, W. J. Nellis and S. R. Nutt (1994), "Dynamic Compaction of  $\text{Al}_2\text{O}_3$ – $\text{ZrO}_2$  Compositions," *J. Am. Ceram. Soc.* **77**(6), 1605–1612.
- Verdonck, D., and G. Zandt (1994), "Three-Dimensional Crustal Structure of the Mendocino Triple Junction Region from Local Earthquake Travel Time," *J. Geophys. Res.* **99**, 23843.
- Wenk, H.-R. (1994), "Texture Development during Deformation: New Results in Complex Systems," *Solid State Phenom.* **35–36**, 45.
- Woosley, S. E., J. R. Wilson, G. J. Mathews, R. D. Hoffman, and B. S. Meyer (1994), "The r-Process and Neutrino-Heated Supernova Ejecta," *Astrophys. J.* **433**, 229.
- Yin, A., T. M. Harrison, F. J. Ryerson, C. Wenji, W. S. F. Kidd, and P. Copeland (1994), "Tertiary Structural Evolution of the Gangdese Thrust System: Southeastern Tibet," *J. Geophys. Res.* **99**, 18175–18201.
- Zandt, G., A. A. Valasco, and S. L. Beck (1994), "Composition and Thickness of the Southern Altiplano Crust, Bolivia," *Geology* **22**(11), 1003–1006.
- Zandt, G., and C. J. Ammon (in press), "Continental Crust Composition Constrained by Measurements of Crustal Poisson's Ratio," *Nature*.



---

1993

---

- Akers, W. T., M. Grove, M. Harrison, and F. J. Ryerson (1993), "The Instability of Rhabdophane and Its Unimportance in Monazite Petrogenesis," *Chem. Geology* **110**, 147–168.
- Alcock, C., C. Akerlof, R. Allsman, T. Axelrod, D. Bennett, S. Chan, K. Cook, K. Freeman, K. Griest, S. Marshall, H.-S. Park, S. Perlmutter, B. Peterson, M. Pratt, P. Quinn, A. Rodger, C. Stubbs, and W. Sutherland (1993), "Possible Gravitational Microlensing of a Star in the Large Magellanic Cloud," *Nature* **365**, 621.
- Ammon, C. J., and G. Zandt (1993), "Receiver Structure beneath the Southern Mojave Block, California," *Bull. Seis. Soc. Am.* **83**, 737–755.
- Bennett, K., H.-R. Wenk, A. Gratz, M. Bourke, and J. A. Goldstone (1992), "Neutron Diffraction of Shock-Loaded Low-Temperature D<sub>2</sub>O Ice," *EOS Trans. Am. Geophys. Union* **73**, 326.
- Bennett, K., H.-R. Wenk, C. S. Choi, and S. F. Trevino (1993), "Texture Development in Deformed Polycrystalline Ice II: A Study by Neutron Diffraction, in *Textures of Geological Materials*, H.-J. Bunge and K. Weber, Eds., *Ger. Soc. Mat. Sci.* (submitted).
- Bennett, K., H.-R. Wenk, W. B. Durham, S. K. Kirby, and L. A. Stern (1993), "Preferred Crystallographic Orientation in Polycrystalline Ice with Hard Particulates" (submitted).
- Bennett, K., H.-R. Wenk, W. B. Durham, S. H. Kirby, and L. A. Stern (1993), "Rheology and Preferred Orientation Development in Ice I with Dispersed Particulates and Ice II at Low-Temperature: Application to Plastic Anisotropy in the Icy Satellites," *EOS Trans. Am. Geophys. Union* (submitted).
- Benson, D. J. (1993), "An Analysis by Direct Numerical Simulation of the Effects of Particle Morphology on the Shock Compaction of Copper Powder," *Modeling and Simulations in Mat. Sci. Eng.* (submitted).
- Benson, D. J., and W. J. Nellis (1993), "Dynamic Compaction of Copper Powder: Computation and Experiment," *Appl. Phys. Lett.* **65**, 418.
- Benson, J. D., (1993), "The Calculation of the Shock Velocity–Particle Velocity Relationship for a Copper Powder by Direct Numerical Simulation," *Wave Motion* (submitted).
- Chandramouli, M., G. Thomas, and W. J. Nellis (1993), "Shock Compaction of Fe–Nd–B," *J. Appl. Phys.* **73**(10), 6494–6496.
- Chastel, Y. B., P. R. Dawson, H.-R. Wenk, and K. Bennett (1993), "Anisotropic Convection with Implications for the Upper Mantle," *J. Geophys. Res. B* **98**, 17757.

- DeLoach, T., M. Clough, and W. J. Nellis (1993), "Shock Amorphization of Cristobalite," *Science* **259**, 663.
- Duong, H., M. Beeman, and J. Wolfenstien (1993), "Creep and Dislocation Substructure of KCl-KBr Solid Solution Alloys," *Acta Metal. Materialia* (submitted).
- Freim, J., J. McKittrick, and W. J. Nellis (1993), "Shock Compaction of Al/Zi Ceramics" presented at Am. Phys. Soc. Meeting (Colorado Springs, CO).
- Freim, J., J. McKittrick, and W. J. Nellis (1994), "Structure Ceramics Produced through Post-Sintering of Dynamically Compacted Powder," presented at Fifth Int. Symp. Ceramic Materials and Component for Engines (Shanghai, China).
- Fuller, G. (1993), "The Curious Connection among Neutrino Masses, Mixings, and Heavy-Element Nucleosynthesis in Supernovae," presented at Massachusetts Institute of Technology (Cambridge, MA).
- Fuller, G. (1993), "The Curious Connection between Neutrino Dark Matter and r-Process Heavy-Element Nucleosynthesis in Supernovae" presented at University of Washington.
- Fuller, G. (1994), "Constraining Weak Interaction Physics and Neutrino Properties with Astrophysical Considerations," presented at the Snowmass Workshop.
- Gratz, A. J., et al. (1992), "Shock Metamorphism of Quartz with Initial Temperatures  $-170^{\circ}\text{C}$  to  $1000^{\circ}\text{C}$ ," *Phys. Chem. Minerals* **19**, 267–288.
- Gratz, A. J., L. D. DeLoach, T. M. Clough, and W. J. Nellis (1993), "Shock Amorphization Of Cristobalite," *Science* **259**, 663–666.
- Gratz, A. J., W. J. Nellis, and N. A. Hinsey (1993), "Observations of High-Velocity, Weakly Shocked Ejecta from Experimental Impacts," *Nature* **363**, 522–524.
- Gurrola, H., G. E. Baker, and J. B. Minster (1993), "Simultaneous Time Domain Deconvolution with Application to Receiver Functions," *Geophys. J. Int.* (submitted)
- Hoffman, R. (1994), "Gamma-Ray Radioactivities from Supernova Explosion," presented at the Gamma-Ray Sky with CGRO and Sigma Conf. (Les Houches, France).
- Hoffman, R. (1994), "The r-Process and Neutrino-Heated Supernova Ejecta," presented at Conf. Nuclei in the Cosmos (Gran Sasso, Italy).
- Hubert, A., and S. Schwartz (1993), "State of Stress at the Cape Mendocino Triple Junction from Inversion of Focal Mechanisms of the 1992 Petrolia, CA, Earthquake Sequence," *Trans. Am. Geophys. Union* **74**, 200.
- Jedamzik, K., G. M. Fuller, G. J. Mathews, and T. Kajino (1993), "Enhanced Heavy Element Formation in Baryon-Inhomogeneous Big Bang Model," *Astrophys. J.* **422**, 423.

- 
- Kagan, Y. Y. (1993), "Distribution of Incremental Static Stress Caused by Earthquakes," *Nonlinear Processes Geophys.* (submitted).
- Kagan, Y. Y. (1993), "Observational Evidence for Earthquakes as a Nonlinear Dynamic Process" *Physica D.* (submitted).
- Leloup, P. H., T. M. Harrison, F. J. Ryerson, C. Wenji, Li Qi, P. Tapponier, and R. Lacassin (1993), "Structural, Petrological and Thermal Evolution of a Tertiary Ductile Strike-Slip Shear Zone, Diancang Shan Yunnan," *J. Geophys. Res.* **98**, 6715–6744.
- Maheshwari, A., and A. Ardell (1993), "Morphological Evolution of Coherent Misfitting Precipitates in Anisotropic Elastic Media," *Phys. Rev. Lett.* **70**, 2305.
- Mangino, S. G., G. Zandt, and C. J. Ammon (1993), "The Receiver Structure beneath Mina, Nevada," *Bull. Seis. Soc. Am.* **83**.
- Mathews, G. J., R. Boyd, and G. M. Fuller (1993), "Chemical Evolution of Irregular Galaxies and the Primordial of  $^4\text{He}$  Abundance," *Astrophys. J.* (in press).
- Nellis, W. J., and A. J. Gratz (1993), "Recovery of Materials Impacted at High Velocity," *Int. J. Impact Eng.* **14**(1–4), 531–539.
- Nishiizumi, K., C. P. Kohl, R. Dorn, J. Klein, D. Fink, R. Middleton, D. Lal, and J. R. Arnold, (1993), "Role of In Situ Cosmogenic Nuclides  $^{10}\text{Be}$  and  $^{26}\text{Al}$  in the Study of Diverse Geomorphic Processes," *Earth Surface Processes Landform* **18**, 407.
- Qian, Y.-Z., G. M. Fuller, G. J. Mathews, R. W. Mayle, J. R. Wilson, and S. E. Woosley (1993), "Connection between Flavor Mixing of Cosmologically Significant Neutrinos and Heavy-Element Nucleosynthesis in Supernovae," *Phys. Rev. Lett.* **71**, 1965.
- Schwartz, S. Y. (1993), "Source Parameters of Local Earthquakes from Inversion of P- and S-Wave Amplitudes," *Trans. Am. Geophys. Union* **74**, 399.
- Seidl, M. A., W. E. Dietrich, and J. W. Kirchner, (1993), "Longitudinal Profile Development into Bedrock: An Analysis of Hawaiian Channels," *J. Geology* **102**, 457–474.
- Verdonck, D., and G. Zandt (1993), "Three-Dimensional Crustal Structure of the Mendocino Triple Junction Region from Local Earthquake Travel Times," *J. Geophys. Res. Solid Earth* **99**(12), 23843–23858.
- Warren P. H., A. E. Rubin, J. T. Wasson, A. J. Gratz, W. J. Nellis, and N. H. Hinsey (1993), "Experimental Shock of Loess and a Compositionally Analogous Siltstone: Implications for the Origin of Tektites," *EOS Trans. Am. Geophys. Union* **74**, 390.
- Zandt, G., and C. R. Carrigan (1993), Small-Scale Convective Instability and Upper Mantle Viscosity under California," *Science* **261**, 460–463.



## Section VI. Fiscal Year 1995 IGPP–LLNL University Collaborative Research Program

Project No.	UC campus	Student investigators	LLNL collaborators	Project title
AP 95-02	Davis	R. Becker	W. van Breugel	The VLA's survey of the sky at 1400 MHz
AP 95-05	Berkeley	G. Basri	K. Cook	Variability of evolved stars in the LMC
AP 95-06	Berkeley	C. McKee	J. Bell, R. Klein	Numerical studies of fragmentation in star formation regions
AP 95-07	Berkeley	K. Hurley	K. Ziock	Development work on a gamma-ray burst and particle detector for the Mars surveyor and Pluto fast flyby missions
AP 95-09	San Diego	G. Fuller	T. Weaver	The evolution of supermassive objects
AP 95-13	Santa Barbara	R. Antonucci	W. van Breugel	Unified models and the alignment effect in radio galaxies and quasars
GS 95-16	Berkeley	R. Jeanloz	W. Nellis	Shock amorphization of olivine
GS 95-18	San Diego	S. Constable	A. Duba	Seebeck coefficient and quantitative electrical conductivity models for olivine rock
GS 95-20	Los Angeles	M. Nicol	C.-S. Yoo	Equations of state of planetary materials by x-ray diffraction studies at high pressures and temperatures achieved by laser heating
GS 95-22	Berkeley	D. DePaolo	I. Hutcheon	Ion microprobe analyses of samples from the Hawaiian scientific drilling project
GS 95-25	Santa Cruz	E. Knittle	R. Reichlin	Optical absorption and reflectance measurements of iron sulfides at high pressure: Application to the nature of bonding in the Earth's outer core
GS 95-26	Los Angeles	M. Reid	R. Finkel, M. Caffee	Quaternary differential rates of uplift in the northwestern Himalaya using cosmogenic nuclide dating of strath terraces
GS 95-27	Los Angeles	W. Kaula	C. Williams	Numerical simulations of convergent crustal plateau formation

Project No.	UC campus	Student investigators	LLNL collaborators	Project title
GS 95-28	Los Angeles	M. Harrison	R. Ryerson	Crustal thickening in southern Tibet: The Kailas connection
GS 95-29	Los Angeles	K. McKeegan	R. Ryerson	The effect of pressure on oxygen diffusion in olivine and its high-pressure polymorphs
GS 95-30	San Diego	J. McKittrick	W. Nellis	Enhanced sinterability of shock-compacted, zirconia-toughened alumina composites
GS 95-31	San Diego	D. Lal	M. Caffee, R. Finkel, J. Southon	Development of a nuclear method based on cosmogenic in situ nuclides $^{14}\text{C}$ and $^{10}\text{Be}$ for determining soil erosion rates
GS 95-32	San Diego	B. Maple	W. Nellis	Shock compaction of nanoparticles of rare-earth permanent magnets
GS 95-33	Los Angeles	F. Kyte	R. Finkel	$^{26}\text{Al}$ and $^{10}\text{Be}$ in sediments of the equatorial Pacific
GS 95-36	Santa Cruz	Q. Williams	R. Ryerson, H. Shaw	Element partitioning between silicate melts and crystals: Constraints on magmatic segregation and transport processes from the uranium decay series
GS 95-38	Berkeley	W. Dietrich	R. Finkel	Empirical determination of a soil production law using topographic data, measurements of soil depth, and cosmogenic nuclides
GS 95-40	Santa Cruz	S. Schwartz,	K. Mayeda, W. Walter, H. Patton, G. Zandt	Waveguide effects on regional wave propagation in the western United States: Application to seismic discrimination
GS 95-41	Santa Cruz	Y.-S. Zhang	H. Patton	Three-dimensional modeling of upper mantle structure beneath the western United States
GS 95-42	San Diego	P. Shearer	G. Zandt	Imaging the 80-km discontinuity with shear-coupled P waves
GS 95-43	San Diego	J. P. Morgan	G. Zandt, C. Carrigan	Modeling small-scale atmosphere convection under California

Project No.	UC campus	Student investigators	LLNL collaborators	Project title
GS 95-45	Davis	C. Leshner	A. Kersting, A. Volpe	High-field-strength and rare-earth element concentrations in island arc and continental rifting volcanic rocks by inductively coupled plasma mass spectrometry: Geochemical constraints on mantle melting processes
GS 94-47	Santa Cruz	J. Zhang	W. Walter	The shear-wave velocity structure beneath central California from surface waves







